# Extrinsic and Intrinsic Dynamics in Visuomotor Tracking

Damar Susilaradeya

Submitted for

Doctor of Philosophy in Neuroscience

Supervisors:

Prof Andrew Jackson

Dr Kai Alter

Dr Ferran Galán

Newcastle University

Institute of Neuroscience

February 2018

*Untuk guru-guruku yang tak lelah mengajar, membimbing, dan mendampingiku dengan sabar dan menanamkan rasa percaya diri sehingga aku bisa sampai di tahap ini.*

# Abstract

Humans typically produce 2–3 submovements per second when tracking slow targets. This intermittency is altered by the addition of delays in sensory feedback suggesting that it is governed by extrinsic properties of the control loop. However, the motor cortex also exhibits an intrinsic rhythmicity at 2–3 Hz, which might influence the temporal structure of movements. This thesis examines how the interplay between extrinsic and intrinsic dynamics shapes the kinematics of tracking behaviour.

I found that the dependence of submovement frequencies on extrinsic delays could be reproduced by a simple feedback controller model. This model predicted that submovements reflect frequencies at which visuomotor noise is exacerbated, and this was confirmed by perturbation experiments. However, these experiments also revealed a 2-3 Hz band-pass filtering of feedback responses irrespective of extrinsic delay. Further experimental evidence suggested this filter did not reflect properties of either visuomotor noise, the feedforward pathway, or visual processing. However, the filter exhibited features consistent with a state estimator required for optimal feedback control (OFC) in the presence of visual and motor noise.

Finally, I sought evidence that this filter was implemented by motor cortical circuits. Multichannel local field potentials (LFPs) in the motor cortex of macaque monkeys were strongly correlated with submovements, at frequencies which depended on extrinsic delay. However, the dynamics of LFP cycles during submovements were independent of delay, and matched instead the properties of the state estimator in the OFC model.

In summary, by combining human behavioural studies, computational modelling and monkey electrophysiology, I show how movement intermittency can be explained by the interplay of both extrinsic and intrinsic dynamics within an OFC framework. Moreover, I suggest that motor cortical rhythmicity reflects recurrent circuitry that combines sensory feedback with an internal dynamical model to form optimal estimates of required motor corrections.

# Acknowledgements

I am grateful to many people who have supported me throughout the PhD.

First, I would like to acknowledge Thomas M. Hall and Wei Xu who collected the monkey data (from Monkeys S and U, respectively) presented in Chapter 5. Adam Stubbs contributed to the development of the human task. My main supervisor, Professor Andrew Jackson, contributed to all of the work in this thesis.

I would particularly like to thank Andy for being an amazing supervisor throughout the PhD. I consider myself very lucky to be under the guidance of such a capable scientist. I have learned a lot from Andy's methods of scientific discovery and dissemination. Thank you for guiding me through every step of the PhD journey!

Next, I would like to thank my other PhD supervisors, Dr. Kai Alter and Dr. Ferran Galán. Thank you both for being there for me, and supporting me throughout my PhD. Thanks Kai, for being so supportive and understanding, and for always providing me with good advice and encouragement. Thank you Ferran, for reminding me to learn to walk before I can run! You are a great teacher – hardworking and thorough. Thank you for being so helpful and teaching me so many things!

I would also like to extend my gratitude to my panel members, Dr Mark Baker and Prof. Jenny Read, who have given me advice and support throughout the PhD.

I would like to thank the Indonesian Endowment Fund for Education (Lembaga Pengelola Dana Pendidikan Republik Indonesia) for supporting my PhD studies. This work would also not have been possible without the financial support of the Wellcome Trust, and the Medical Research Council.

I would like to thank people in JacksonLab, the Motor Control Group, and the Institute of Neuroscience, who have provided support to me in many different ways: Claire Schofield, Tom Hall, Felipe de Carvalho, Wei Xu, Edmund Hodkin, Matthieu Ambroise, Boubker Zaaimi, Stuart Baker, Demetris Soteropoulos, Karen Fisher, Lauren Dean, Norman Charlton, Terri Jackson, Jennifer Tulip, Stephan Jaiser, Isabel Glover, Peter Trebilcock, Ann Fitchett, Beckie Hedley, Barry Hirst, Sid Henriksen, Zoltan Derzsi, Lisa Jones, and Anderson Brito da Silva.

I would like to thank the Faculty of Medicine Universitas Indonesia for the support to undertake a PhD. My sincere thanks goes to Prof. Dr. Pratiwi Pudjilestari Sudarmono, Ph.D., SpMK(K), Dr. Nani Cahyani Sudarsono, SpKO, Dr. Evita Halim, Sp.KK(K), and Dr. Isabella Kurnia Liem, PhD.

Special thanks goes to 汤汤 for providing me with extra support during the writing of the thesis. You are a very special person.

I would like to express my deepest gratitude to my family: Opa, Papa, Mama, Dian, Mami Jo, Pi Bon, the Sidharta's and the Hutauruk's.

For those who have *'merantau'*, you will appreciate the *'gezelligheid'* from a family other than your own. Thank you so much to the Collins and the Ifzaren families for giving me a home during Christmas and New Year. Thank you to my dear flat mates: Miriam, Sarah, Juni, Shen, and Victoria. Thanks to Paul and Peter for colouring my life. Thanks to Steve, Tamara, Neela, Alexis, Stefane, Oliver, Richard, Kathleen, Yingdi, Dinar, Metta, Anna, Dina, Vania, Syema, and Riashad for being such amazing friends. Last, I would like to thank Georgia for being on my mind. Hah!

*"Standing on the shoulders of giants, shoulder to shoulder with the dwarfs."*

# Conference Presentations

**Damar Susilaradeya**, Ferran Galán, Kai Alter and Andrew Jackson. Movement intermittency: visuomotor feedback loop or intrinsic rhythmicity? Poster session presented at: British Neuroscience Association 2015: Festival of Neuroscience; 2015 April 12-14; Edinburgh, UK.

**Damar Susilaradeya**, Ferran Galán, Kai Alter and Andrew Jackson. Movement intermittency: visuomotor feedback loop or intrinsic rhythmicity? Poster session presented at: Society for Neuroscience 45th Annual Meeting; 2015 October 17-21; Chicago, USA.

**Damar Susilaradeya**, Ferran Galán, Kai Alter and Andrew Jackson. Submovements: visuomotor feedback loop or intrinsic rhythmicity? Poster session presented at: 10th Federation of European Neuroscience Societies Forum of Neuroscience; 2016 July 2-6; Copenhagen, Denmark.

**Damar Susilaradeya**, Ferran Galán, Kai Alter and Andrew Jackson. Extrinsic and intrinsic dynamics in visuomotor tracking. Poster session presented at: Society for Neuroscience 46th Annual Meeting; 2016 November 12-16; San Diego, USA.

**Damar Susilaradeya**, Thomas Hall, Ferran Galán, Kai Alter and Andrew Jackson. Intrinsic and extrinsic contributions to submovement kinematics. Poster session presented at: Neural Control of Movement 27th Annual Meeting; 2017 May 2-5; Dublin, Ireland.

# Table of Contents

**Abstract......v**

**Acknowledgements......vii**

**Conference Presentations......x**

**Table of Contents......xi**

**List of Figures......xvii**

**List of Tables......xix**

**Abbreviations......xx**

**Chapter 1. Introduction......1**

1.1 Computational basis for motor control......1
1.2 Literature review of intermittency research from an historical perspective......4
1.3 Optimal Feedback Control and movement intermittency......6
1.4 Neural basis for movement intermittency......7
1.5 The current state of knowledge on movement intermittency......7
1.6 Thesis overview......10

**Chapter 2. Methods......11**

2.1 Human experiments......11
  2.1.1 Tracking experiment......11

  2.1.2 Tapping experiment......13

  2.1.3 Data analysis of tracking experiment......14

  2.1.4 Data analysis of tapping experiment......15

2.2 Monkey experiments ........................................................................... 15
2.2.1 Centre-out task ........................................................................... 15
2.2.2 Surgical procedure and LFPs recording .......................................... 16
2.2.3 Data analysis ........................................................................... 17

**Chapter 3. Origin of submovements during visuomotor tracking...................... 18**
3.1 Chapter overview ........................................................................... 18
3.2 Effect of visual feedback delay on submovement frequencies ........................ 18
3.2.1 Aim ........................................................................... 18
3.2.2 Methods ........................................................................... 18
3.2.3 Analysis of performance and power spectra ............................................ 19
3.2.4 Linear fitting of submovement harmonics ................................................ 21
3.2.5 Summary ........................................................................... 21
3.3 A feedback controller to model submovement frequencies ............................ 22
3.3.1 Aim ........................................................................... 22
3.3.2 Methods ........................................................................... 22
3.3.3 Feedback controller exhibited comb filtering properties ........................... 23
3.3.4 Simulation of the effect of delay on submovement frequencies ................ 25
3.3.5 Summary ........................................................................... 26
3.4 Human amplitude response to sinusoidal spatial perturbations during tracking ........................................................................... 27
3.4.1 Aim ........................................................................... 27
3.4.2 Methods ........................................................................... 27
3.4.3 Analysis of performance and example .................................................... 29
3.4.4 Analysis of cursor power spectra and gain response............................... 31
3.4.5 Summary ........................................................................... 35

3.5 Discussion ........................................................................................35
3.5.1 Novel bimanual tracking task ....................................................................35
3.5.2 Dependency of delay on submovement frequencies.................................36
3.5.3 Linear feedback controller reproduced submovements.............................36
3.5.4 Human’s amplitude response resembled a comb filter..............................37
3.6 Chapter summary ....................................................................................38
**Chapter 4. Origin of intrinsic dynamics during visuomotor tracking .................39**
4.1 Chapter overview......................................................................................39
4.2 Finger-force frequency response to perturbations ...................................42
4.2.1 Aim..........................................................................................................42
4.2.2 Methods ...................................................................................................42
4.2.3 Analysis of finger-force power spectra and gain response........................43
4.2.4 Analysis of finger-force time delay response.............................................46
4.2.5 Summary...................................................................................................46
4.3 Feedforward tapping.................................................................................47
4.3.1 Aim..........................................................................................................47
4.3.2 Methods ...................................................................................................47
4.3.3 Analysis of example, power spectra and gain response............................48
4.3.4 Summary...................................................................................................50
4.4 Incorporating intrinsic dynamics in feedback controller model ..........................50
4.4.1 Aim..........................................................................................................50
4.4.2 Methods ...................................................................................................51
4.4.3 Cursor and finger-force frequency response.............................................57
4.4.4 Simulation of the effect of delay on submovement frequencies ................58

4.4.5 Simulation of the effect of perturbations on cursor frequency response and finger-force amplitude response ........ 60

4.4.6 Summary ........ 62

4.5 Discussion ........ 63
4.5.1 Intrinsic dynamics did not reflect properties of visuomotor noise ........ 63

4.5.2 Feedforward process did not impose intrinsic dynamics ........ 63

4.5.3 Intrinsic dynamics were modelled to originate in the feedback process: specifically the state estimator ........ 64

4.5.4 Attenuation of feedback gains in isometric visuomotor tracking ........ 65

4.6 Chapter summary ........ 66

**Chapter 5. Extrinsic and intrinsic dynamics in local field potentials recorded from non-human primates ........ 67**

5.1 Chapter overview ........ 67
5.2 Aim ........ 68
5.3 Methods ........ 68
5.4 Analysis of power spectra and coherence of speed and LFP ........ 70
5.5 Analysis of submovement related activity ........ 76
5.6 Analysis of submovement-triggered LFP-PC trajectories and imaginary cross-spectral density of LFPs ........ 79
5.7 Prediction of LFP activity during sleep ........ 80
5.8 Discussions ........ 82
5.8.1 Delay-dependent features in behaviour and LFPs ........ 82

5.8.2 Delay-independent features in behaviour and LFPs ........ 84

5.8.3 LFP activity during sleep ........ 87

5.9 Chapter summary ........ 88

**Chapter 6. General discussion ........ 89**

6.1 Main findings of this thesis ........ 89
6.2 Submovement reflect exacerbation of visuomotor noise ........ 90
6.2.1 The role of visual feedback in the generation of submovements ........ 90

6.2.2 Submovements reflect filtered noise instead of movement segmentation .91

6.2.3 Submovements reflect error correction of noise .......................................92

6.3 Submovement kinematics reflected both extrinsic and intrinsic dynamics .......93
6.3.1 Where does intrinsic dynamics arise from? ..............................................93

6.3.2 Evidence for intrinsic dynamics in rhythmical behaviours..........................94

6.4 Rotational state-space trajectories of M1 LFP reflect a recurrent neural network involved in state estimation .........................................................................94
6.5 Future directions ..........................................................................................96
6.5.1 A framework to generalize findings ...........................................................96

6.5.2 Removing submovements ..........................................................................96

6.5.3 Evidence for a smith predictor ...................................................................96

6.6 Conclusions ...................................................................................................97

**Appendix A. Target speed tracking experiment ..................................................98**

**Appendix B. Equations ........................................................................................100**

Tracking experiment ............................................................................................100
Spatial perturbations ............................................................................................100

Calculation of score .............................................................................................100

Calculation of angular velocity .............................................................................100

Calculation of frequency response to perturbations ...........................................102

Calculation of root-mean-squared error ..............................................................103

Tapping experiment .............................................................................................103
Calculation of amplitude response ......................................................................103

Monkey experiment .............................................................................................104
Calculation of cursor velocity ...............................................................................104

Calculation of magnitude squared coherence in monkey experiment ..............104

Calculation of imaginary cross-spectral density ............................................... 104

**References ........................................................................................................ 106**

# List of Figures

Figure 1.1.1 Feedback and feedforward control of voluntary movement. ....................2

Figure 1.1.2 Internal models. ..........................................................................2

Figure 1.1.3 Development of feedback control. ..........................................................4

Figure 1.2.1 Example of intermittencies seen during visuomotor tracking. ..................5

Figure 2.1.1 Human visuomotor tracking task. ........................................................12

Figure 2.1.2 Human tapping task. .........................................................................14

Figure 2.2.1 Monkey centre-out task. .....................................................................16

Figure 3.2.1 Task design, performance, and examples of delay experiment. ............19

Figure 3.2.2 Effect of visual feedback delay on submovement frequencies. .............20

Figure 3.3.1 Schematic of visuomotor tracking model and its comb filter amplitude response ..........................................................................................23

Figure 3.3.2 Simulation of the visuomotor tracking model and the effect of delay on submovement frequencies. ............................................................................26

Figure 3.4.1 Task design of spatial perturbation and delay experiment. ...................28

Figure 3.4.2 Performance of participants and model in spatial perturbation and delay experiment. ..........................................................................................30

Figure 3.4.3 Examples of tracking data, from an example subject (left) and generated by the comb filter model (right), in the perturbation and delay experiment. ...............31

Figure 3.4.4 Individual power spectra of cursor velocity in response to perturbations. .........................................................................................................33

Figure 3.4.5 Averaged cursor response to perturbations and predictions by model. .34

Figure 4.1.1 Comparison of submovement spectra from experimental and simulated data. ..........................................................................................................40

Figure 4.1.2 Schematic of plausible sources of intrinsic dynamics. ...........................41

Figure 4.2.1 Diagram of measured finger-force response to spatial perturbations. ...43

Figure 4.2.2 Individual power spectra of finger-force velocity in response to perturbations. ..................................................................................................44

Figure 4.2.3 Averaged finger-force response to perturbations, compared to predictions by model. ..........................................................................................45

Figure 4.3.1 Task conditions and examples data from the tapping experiment. .........48

Figure 4.3.2 Individual power spectra, averaged power spectra and gain of tapping. ........ 49

Figure 4.4.1 Schematic and frequency response of a tracking model incorporating intrinsic dynamics. ........ 52

Figure 4.4.2 Simulation of the *+intrinsic dynamics* model and the effect of delay on submovement frequencies. ........ 58

Figure 4.4.3 Comparison between comb filter and +intrinsic dynamics model in predicting submovement frequencies and internal time delay. ........ 60

Figure 4.4.4 Examples and performance of the *+intrinsic dynamics* model in simulation of the perturbation delay experiment. ........ 61

Figure 4.4.5 Simulation of the effect of perturbations in the *+intrinsic dynamics* model. ........ 62

Figure 5.1.1 Neuronal implementation of the state estimator. ........ 67

Figure 5.4.1 Task design and examples of LFP experiment. ........ 71

Figure 5.4.2 Frequency analysis of speed and LFPs in monkey S. ........ 72

Figure 5.4.3 Frequency analysis of speed and LFPs in monkey U. ........ 73

Figure 5.4.4 Frequency analysis of speed and LFPs in the *+intrinsic dynamics* model. ........ 75

Figure 5.5.1 Submovement related activity in monkey S. ........ 76

Figure 5.5.2 Submovement related activity in monkey U. ........ 77

Figure 5.5.3 Submovement related activity in the data generated by the *+intrinsic dynamics* model. ........ 79

Figure 5.6.1 Delay-independent low-frequency rotational structure in LFP. ........ 80

Figure 5.7.1 The model predicted a rotational structure during sleep. ........ 81

Figure 5.7.2 Simulation of K-complexes during sleep in the *+intrinsic dynamics* model. ........ 82

Figure 5.8.1 Schematic of submovement-triggered averages and frequency analysis results in the model. ........ 84

Figure appendix A 2 Smoothed power spectra of cursor velocity at different target speeds in the no delay condition ........ 98

Figure appendix A 3 Smoothed power spectra of cursor velocity at different target speeds in the 200 ms delay condition. ........ 99

# List of Tables

Table 1.5.1 Extrinsic and intrinsic evidence of intermittency. ......................................9

Table 3.2.1 Linear fitting of submovement harmonics. ............................................21

Table 6.1.1 Summary of extrinsic and intrinsic features found in behaviour and neural activity. .....................................................................................................................89

# Abbreviations

| | |
|---|---|
| $\dot{e}_t$ | error velocity |
| $\hat{e}_t$ | optimally estimated error position |
| $K_i$ | integral gain |
| $K_p$ | proportional gain |
| $P_{pos}$ | mean activity of neural population representing position |
| $P_{vel}$ | mean activity of neural population representing velocity |
| $T_{art}$ | artificial delay |
| $T_m$ | model delay |
| $T_v$ | visual delay |
| $f_{pert}$ | perturbation frequency |
| $r_t$ | feedforward command |
| $t_{subm}$ | submovement period |
| $y'_t$ | visual feedback prediction |
| 1D | 1 dimension |
| 2D | 2 dimension |
| ANOVA | analysis of variance |
| CPG | central pattern generator |
| CSD | cross-spectral density |
| FIR | finite impulse response |
| LFP | local field potential |
| M1 | primary motor cortex |

| | |
|---|---|
| NHP | non-human primate |
| OFC | optimal feedback control |
| PET | positron emission tomography |
| PPC | posterior parietal cortex |
| PRP | psychological refractory period |
| RMSE | root-mean-squared error |
| UCM | uncontrolled manifold |
| $FM$ | forward model |
| $J$ | cost function |
| $T$ | total time delay |
| $\boldsymbol{D}$ | matrix applying $\boldsymbol{a}$ |
| $\boldsymbol{F}$ | state transition matrix |
| $\boldsymbol{G}$ | control input matrix |
| $\boldsymbol{H}$ | transformation matrix |
| $\boldsymbol{M}$ | innovation gain |
| $\boldsymbol{Q}$ | process noise covariance matrix |
| $\boldsymbol{R}$ | measurement noise covariance matrix |
| $a_t$ | acceleration |
| $e_t$ | true error position |
| $t$ | time |
| $u_t$ | motor command |
| $v_t$ | visual noise |

| | |
|---|---|
| $w_t$ | motor noise |
| $y_t$ | visual feedback |
| $z_t$ | observed error |
| $\varepsilon_t$ | error state |
| $\boldsymbol{\varepsilon}$ | state vector |

# Chapter 1. Introduction

It is remarkable how effortlessly we move, and adapt to a diverse range of contexts – from picking up objects, talking and singing, dancing, lifting weights, writing and drawing, performing surgery, to swimming and skiing. All of these different types of movement require humans to optimise their behaviour to specific constraints (e.g. performing surgery requires accurate and precise movement, whereas skiing requires balancing and planning ahead when moving at high speed). The study of motor control is concerned with understanding how the nervous system interacts with the world and coordinates muscles to generate purposeful movement.

In this thesis I studied visuomotor tracking behaviour. An everyday life example of tracking behaviour is driving, during which appropriate movements of the steering wheel are required to maintain the position of the car on the road. Visuomotor tracking tasks require continuous monitoring of feedback and updating of motor commands. However, despite their continuous nature, discontinuities in movement have frequently been observed in tracking behaviours and this is referred to as movement intermittency. The aim of my study was to understand how these intermittencies arise.

In this chapter, I review aspects of the computational motor control with relevance to movement intermittency. Next, I review the history of our understanding of movement intermittency and the explanations that have been proposed. I will distinguish these explanations into two categories, reflecting intrinsic versus extrinsic perspectives. Finally, I will present an overview of the thesis.

## 1.1 Computational basis for motor control

Until the mid-1970s, the motor system was generally thought to behave as a servo-controller (Scott, 2008). In this view, feedback of sensory consequences is compared with the desired sensory consequences to drive corrections of movement (Figure 1.1.1 (A)). Any errors in the feedback loop will be reduced at every iteration of the cycle until they are nullified.

In the mid-1980s research started to uncover aspects of movement that seemed incompatible with such a purely feedback scheme (Scott, 2008). During multi-joint movements (e.g. arm movements), the trajectory of the end effector (e.g.

the hand) is relatively straight and exhibits stereotyped bell-shaped velocity profiles (Morasso, 1981). This suggested that movements were first planned in a kinematic coordinate frame before being transformed into motor commands (Figure 1.1.1 (B)). According to this view, movement is produced in a ballistic fashion and the sensory consequences of that movement are only observed after its execution. To perform this feedforward control, the brain would require an ‘inverse model’ to transform the desired goal state (e.g. in visual or proprioceptive coordinates) into an appropriate motor command (Figure 1.1.2(A)). Note that due to redundancy in the motor system, there may be multiple motor commands that can achieve any given desired goal. Therefore it was proposed that an optimal feedforward controller would generate motor commands that achieved the desired goal whilst also minimizing some ‘cost function’ (e.g. minimum jerk) (Flash and Sejnowski, 2001).

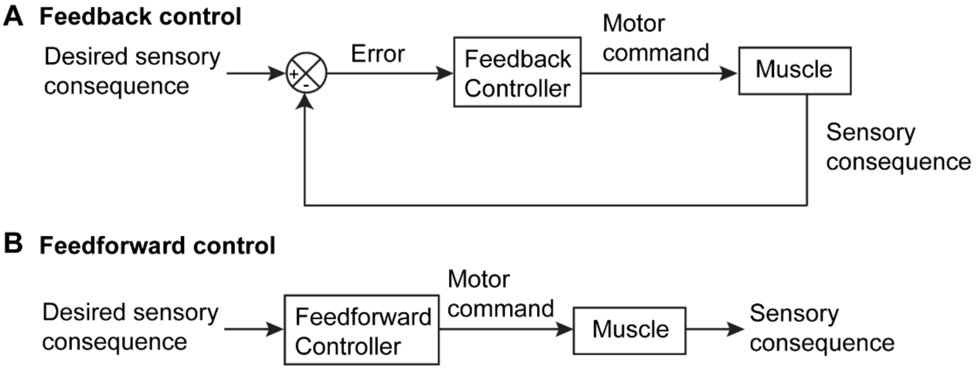

**Figure 1.1.1 Feedback and feedforward control of voluntary movement.**

**(A)** In feedback control, the motor command is driven by comparing the sensory consequence with the desired sensory consequence. **(B)** In feedforward control movement is executed without monitoring of the sensory consequence.

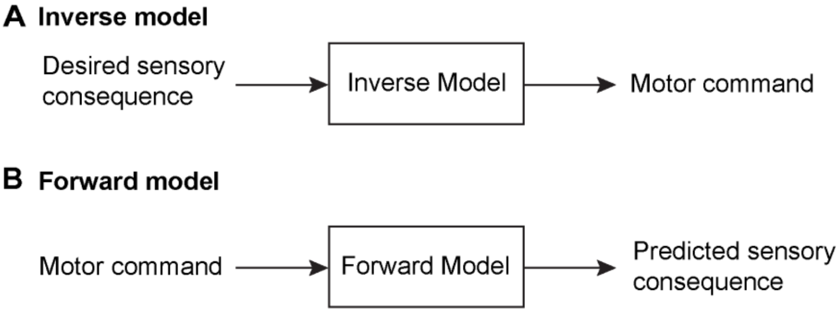

**Figure 1.1.2 Internal models.**

**(A)** An inverse model transform the desired sensory consequence into a motor command. **(B)** A forward model predict the sensory consequences given the motor command.

As well as an ‘inverse model’, it was also suggested that the brain might use a ‘forward model’ (Figure 1.1.2(B)) to predict the sensory consequences of actions based on a copy of the motor command (efference copy). Such predicted sensory consequences could be used to distinguish self-generated sensation from external stimuli, as well as to better estimate the true state of the limbs following movement (Wolpert and Miall, 1996) (Figure 1.1.3 (A)).

A further advantage of using a forward model is in dealing with feedback delays. Such delays can cause instabilities in servo-control which can only be avoided by using a small gain, with consequently slow correction of errors (Miall *et al.*, 1993a). This problem is overcome by implementing a Smith predictor which utilises a forward model in the feedback loop (Miall *et al.*, 1993b). The forward model provides a delayed prediction of the sensory consequences which can then be compared with sensory data (Figure 1.1.3 (B)) allowing the feedback controller to operate with high gains without instabilities (assuming the forward model is accurate).

Recently, the ‘optimal feedback control’ (OFC) framework has combined many of these ideas into an influential theory of motor control (Todorov and Jordan, 2002; Scott, 2004; Diedrichsen *et al.*, 2010). In the presence of sensorimotor noise, optimal movements are generated by optimal feedback policies acting on optimal estimates of the current sensory state. Optimal state estimation combines the predictions of a forward model with noisy, delayed sensory feedback (Figure 1.1.3 (C)). Optimal feedback policies act on task-relevant dimensions of the sensory state, and therefore intervene only to correct task-relevant errors (the ‘minimum intervention principle’). Support for this theory comes from evidence that fast feedback corrections during movement act only along task-relevant dimensions (Diedrichsen *et al.*, 2004; Nazarpour *et al.*, 2012).

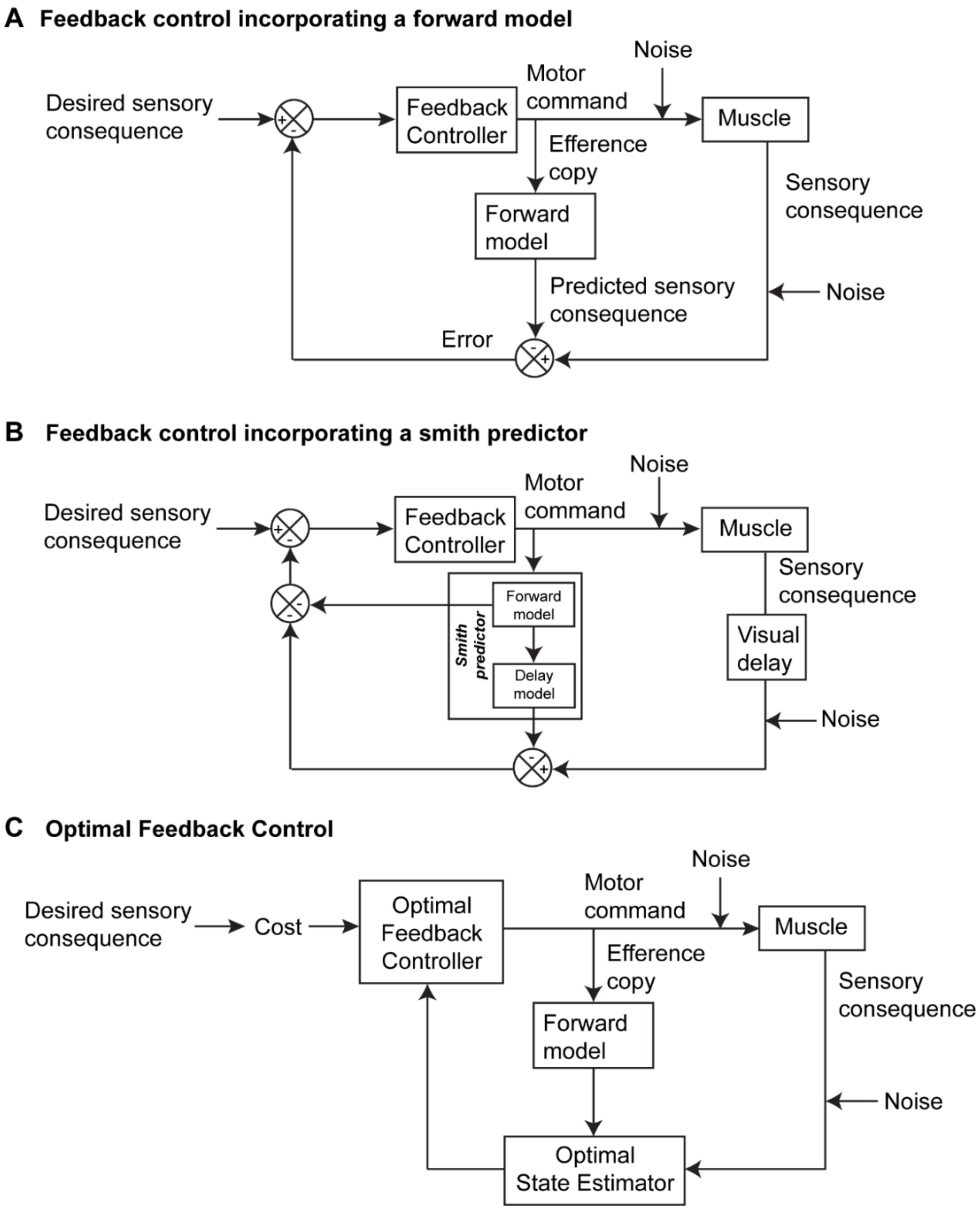
A Feedback control incorporating a forward model

B Feedback control incorporating a smith predictor

C Optimal Feedback Control

**Figure 1.1.3 Development of feedback control.**

**(A)** Incorporating a forward model to the feedback controller. **(B)** Incorporating a Smith Predictor to the feedback controller. **(C)** Optimal Feedback Control framework.

## 1.2 Literature review of intermittency research from an historical perspective

In 1899, Woodworth performed an ‘aiming’ experiment in humans, and described slowing of movement as subjects’ movement approached the target (Woodworth, 1899). Woodworth thus distinguished two stages of movement: (1) an initial ballistic movement, consisting of a large movement to get closer to the target; and (2) finer adjustments, consisting of multiple, smaller movements to home into the target. These smaller movements were thought to be a set of increasingly accurate corrections, made using sensory feedback.

In other seminal studies, Craik and Vince demonstrated intermittencies in tracking movements (Craik, 1947; Vince, 1948), which occurred periodically at a frequency of 2 Hz, irrespective of target speed. This rhythmicity was suggested to arise because of a ‘psychological refractory period’ (PRP). The PRP is a period after execution of a movement, during which a new movement cannot be executed. According to this view, submovements were thought to be controlled periodically in a ballistic fashion. This implied that, once a submovement has been executed, it cannot be altered.

Movement intermittencies have since been described in many studies, mainly during visuomotor tracking (Vince, 1948; Partridge, 1965; Pew, 1974; Miall *et al.*, 1986; Miall *et al.*, 1993; Miall, 1996; McAuley *et al.*, 1999; Hall *et al.*, 2014; Sakaguchi *et al.*, 2015). Intermittencies can be observed in the trajectory of movement and more clearly seen in the differentiated trajectory trace (that is, speed trace) which shows clear, rhythmical fluctuations in speed (e.g. Figure 1.2.1).

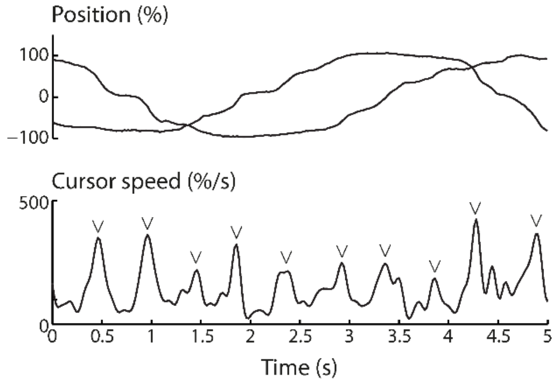

**Figure 1.2.1 Example of intermittencies seen during visuomotor tracking.**
Example of cursor position and differentiated position (speed) in a subject performing a 2D isometric tracking task, revealing intermittencies. Arrows indicate submovements (peaks of fluctuations in speed). Source: Data collected by author (Susilaradeya *et al.*, 2015).

Such rhythmicity has been consistently reported to occur at a frequency of 1−4 Hz (Pew, 1974; Miall, 1996; Pasalar *et al.*, 2005; Hall *et al.*, 2014). In tracking tasks, intermittencies have only been observed when moving slowly, when following target speeds below 2 Hz (Pew *et al.*, 1967). In such tasks, intermittencies are defined as frequencies occurring at other frequencies than target frequencies.

Today, there are three main conceptual ways in which movement intermittency is interpreted. Firstly, many studies continue to interpret intermittency as a sign of intermittent 'feedforward' control of error detected in a feedback loop (Neilson *et al.*, 1988; Gawthrop *et al.*, 2011). In this view, movement is segmented into submovements and executed in a ballistic fashion. The triggers for executing these feedforward submovements are either, (1) a refractory period, (2) an error threshold, or (3) reduced reliability in the internal model (Gawthrop *et al.*, 2011; Sakaguchi *et al.*, 2015).

Secondly, the rhythmicity of intermittencies has been suggested to be caused by intermittent sampling of sensory feedback and movement execution (Bekey, 1962).

Thirdly, intermittencies may be interpreted as part of a dynamical systems framework (Russell and Sternad, 2001). Instead of viewing intermittencies as corrections to error detected in a feedback loop, intermittencies could be viewed as a by-product of instability in a dynamical system. Fluctuations in the kinematics of movement could occur as a result of the human-task system entering an unstable regime, much like how coupled oscillators can temporarily switch between unstable and stable regimes (Haken *et al.*, 1985).

### 1.3 Optimal Feedback Control and movement intermittency

Despite the success of Optimal Feedback Control models, there has been few attempts to explicitly address the phenomenon of movement intermittency within this framework. Visuomotor tracking has often been modelled without directly addressing intermittency (Jagacinski and Flach, 2003, but see Sakaguchi *et al.*, 2015). Conversely, submovements have often been described in an optimal feedback control framework in non-tracking tasks such as reaching (Todorov and Jordan, 2002). In these tasks, the time of movement is often determined in advance, or determined based on a cost function which minimises time (to target) (Qian *et al.*, 2013). On the other hand, modelling of visuomotor tracking has focused on describing the human transfer function but not describing the rhythmicity of intermittency (Kleinman, 1974). Other models have explained intermittency by explicit segmentation of movement, but have neglected the frequency structure of intermittency (Gawthrop *et al.*, 2011). In this thesis, I will argue that intermittency arises as an emergent property of optimal continuous visuomotor tracking, rather than as an explicit segmentation of movement.

### 1.4 Neural basis for movement intermittency

Traditionally, cortical activity during movement has been thought to represent specific parameters of the plant or movement (Scott, 2008). This is known as the ‘representational view’. The problem is that many different parameters of movement are found represented, even within primary motor cortex (M1), making it difficult to answer the question of which parameter is ‘controlled’ by the motor cortex.

More recently, there is increasing interest in an alternative, ‘dynamical system view’ of motor cortical function (Shenoy *et al.*, 2013). In this view, we would expect to see a mix of signals representing different parameters of movement. This view focuses on finding out how the dynamics of neural activity produce movement, rather than asking what parameter is encoded in neural activity. For example, activity in high-dimensional neural firing rate space in M1 has been shown to exhibit rhythmical activity, even when movement (e.g. reaching) is not overtly rhythmical. Such activity appears to be lawful, and lower-dimensional projections of this activity can be modelled as linear (rotational) dynamical systems (Churchland *et al.*, 2012). This finding suggests that the role of motor cortex could be as a pattern generator, similar to the central pattern generators (CPGs) that have been documented in the spinal cord (Kiehn, 2006).

### 1.5 The current state of knowledge on movement intermittency

Theories explaining how intermittencies arise in movement can broadly be classified into two categories: intrinsic theories and extrinsic theories (Table 1.5.1). Intrinsic theories describe how properties inherent to the central nervous system can produce a particular phenomenon. Extrinsic theories describe how the interaction between the central nervous system and the external world can produce that phenomenon. These theories can thus be tested by manipulating external properties and assessing whether features in intermittency are unchanged or changed by the extrinsic manipulation.

Evidence supporting the ‘extrinsic theory of intermittency generation has mainly been focused on the role of visual feedback in the generation of submovements. The strongest evidence for the dependence of submovements on visual feedback is the shift in submovement frequencies seen when delays are added to the visual feedback loop (Pew, 1974; Miall *et al.*, 1986; Miall, 1996). Moreover, submovements have been shown to be dependent on other extrinsic factors such as target speed[1] (Miall, 1996; Celik *et al.*, 2009) and force fields (Pasalar *et al.*, 2005).

There is also a large body of literature supporting the ‘intrinsic theory’. M1 may act as a central-pattern generator, and this could be reflected in submovements. Moreover, submovements have been shown to occur in the absence of visual feedback (Doeringer and Hogan, 1998). An intrinsic refractory period or error ‘dead-zone’ could be responsible for submovements, but these were found to be dependent on extrinsic parameters (Wolpert *et al.*, 1992, van de Kamp *et al.*, 2013). In addition, submovements have also been thought to reflect visuomotor noise (Pew *et al.*, 1967; Celik *et al.*, 2009). Of particular relevance to this thesis is the recent finding of intrinsic rhythmicity in M1 locked to submovements (Hall *et al.*, 2014).

In summary, there is good evidence supporting both extrinsic and intrinsic views of the origins of intermittency. Therefore, in this thesis I aim to re-examine extrinsic and intrinsic contributions to submovements, using the framework of optimal feedback control (OFC) theory.

---

[1] For the interested reader, I tested the effect of target speed on submovement frequencies in the **Error! Reference source not found.**.

**Table 1.5.1 Extrinsic and intrinsic evidence of intermittency.**

| | **Evidence** | **References** |
|---|---|---|
| **Extrinsic** | Submovements depend on the presence of visual feedback. | (Miall *et al.*, 1993) |
| | Submovement frequencies are determined by the visual feedback loop delay. | (Pew, 1974; Miall *et al.*, 1986; Miall, 1996) |
| | Submovement frequencies depend on target speed. | (Miall, 1996; Celik *et al.*, 2009) |
| | Submovements depend on accuracy of tracking. | (Miall *et al.*, 1988; Miall *et al.*, 1993; Reed *et al.*, 2003) |
| | Submovement frequencies depend on external force fields. | (Pasalar *et al.*, 2005) |
| | Refractory period to a double step stimuli were order dependent. | (van de Kamp *et al.*, 2013) |
| | Error dead zone during compensatory tracking was task dependent. | (Wolpert *et al.*, 1992) |
| | Submovements depend on internal model reliability. | (Sakaguchi *et al.*, 2015) |
| **Intrinsic** | Submovements reflect intrinsic rhythmicity in M1. | (Hall *et al.*, 2014) |
| | Submovements are independent on the presence of visual feedback. | (Doeringer and Hogan, 1998) |
| | Submovement frequencies does not depend on target speed. | (Miall *et al.*, 1988; Doeringer and Hogan, 1998; Pasalar *et al.*, 2005) |
| | Submovement frequencies are independent of external inertia manipulation. | (Loram *et al.*, 2006) |
| | Submovements are independent of sensory modality. | (Lakie and Loram, 2006; Hughes *et al.*, 2014; Creighton and Hughes, 2017) |
| | Submovements reflect visuomotor noise. | (Pew *et al.*, 1967; Celik *et al.*, 2009) |
| | Submovements reflect an intrinsic psychological refractory period. | (Craik, 1947; Vince, 1948) |

## 1.6 Thesis overview

The remainder of this thesis is organized as follows:

In chapter 2, I describe the tracking tasks I use to characterize submovements both in humans and monkeys.

In chapter 3, I investigate whether submovements are dependent on extrinsic properties. I further model a feedback controller to explain submovement frequencies.

In chapter 4, I investigate the origin of intrinsic dynamics found in behaviour independent of extrinsic properties. I model intrinsic dynamics as part of a state estimator in an optimal feedback control (OFC) framework.

In chapter 5, I characterize submovements in the movements of Macaque monkey behaviour, and describe local field potentials during submovement generation. I model local field potentials using the feedback controller model with intrinsic dynamics.

Finally in chapter 6, I summarize the findings of this thesis, discuss implications of my findings, and list possible directions for future research.

# Chapter 2. Methods

In this chapter, I will describe the methods of the experiments presented in this thesis. These experiments were designed to address the question whether submovements arise due to extrinsic or intrinsic factors.

First, I will describe the visuomotor tracking task used to characterize submovements in humans. In the first tracking experiment, I delayed visual feedback of the cursor to investigate whether submovements were depended on extrinsic factors. In the second tracking experiment, I added tangential cursor displacements at different frequencies to the cursor to test the extrinsic hypothesis. I will further describe a related tapping task used to investigate feedforward movements in human subjects. I will then describe my analysis methods for these data.

Next, I will describe the centre-out task used to characterize submovements in monkeys. Monkeys' movement has previously been shown to comprise of submovements using the same task in another study in the laboratory (Hall *et al.*, 2014). Recording of behaviour in monkeys allowed simultaneous electrophysiological recording of the motor cortex (M1). This was important to investigate how intrinsic factors of the brain contributes to the generation of submovements. The rhesus macaque is a necessary and appropriate model to study forelimb movement, because only Old World primates (such as macaques) have comparable dexterity and corticospinal tract anatomy to humans (Courtine *et al.*, 2007). Visual feedback was delayed to investigate whether local field potentials (LFPs) were locked to extrinsic factors. Finally, I will describe my analysis methods for these data.

## 2.1 Human experiments

### *2.1.1 Tracking experiment*

I developed an isometric 2D bimanual pursuit tracking task, in which subjects tracked a target on a computer monitor (Figure 2.1.1 (A)). The target underwent uniform circular motion at a frequency of 0.2 revolutions per second. The direction of circular motion on a particular trial was pseudorandomised. The 2D circular trajectory was formed by two sine waves in perpendicular directions with a 90° phase difference (Figure 2.1.1 (B)).

Subjects controlled the cursor in a bimanual manner by exerting isometric force on force sensors (FSG15N1A; Honeywell) with their index fingers. Each finger controlled cursor movement in one dimension (left diagonal or right diagonal). Thus each hand tracked a sinusoid that was phase-shifted relative to the sinusoid tracked by the other hand. The movement of the cursor was proportional to the amount of force exerted. Each dimension of cursor position was expressed as a percentage with 100% and −100% corresponding to the peak and the trough of the sinusoid, respectively. A force of 1.63N was needed to move the cursor position to 100%. The target and cursor were square, with dimensions 59% by 59%. Analog finger force signals were sampled and digitized at 50 samples/s (USB-6343; National Instruments), and translated into cursor position on a monitor screen using custom-written code (Delphi 7, Borland).

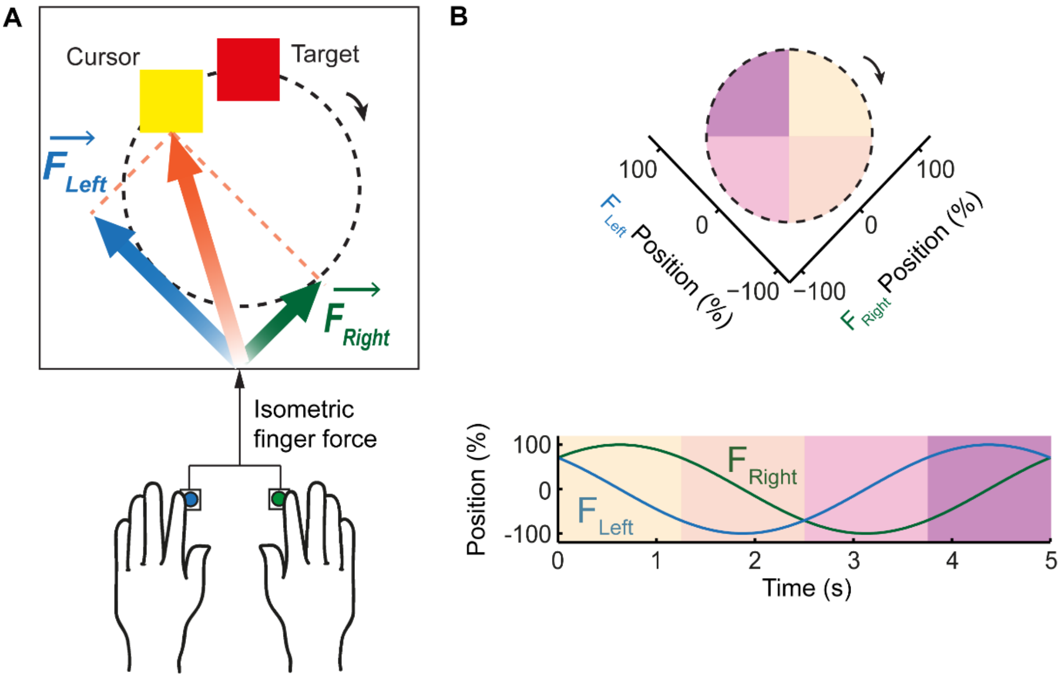

**Figure 2.1.1 Human visuomotor tracking task.**

**(A)** Subjects tracked a target moving circularly at 0.2 Hz on a monitor screen. Cursor position was proportional to $\overrightarrow{F_{Left}}$ (left diagonal dimension) and $\overrightarrow{F_{Right}}$ (right diagonal dimension) isometric finger force. **(B)** The 2D cursor position was thus formed by two sine waves in each dimension, with 90° phase difference**.** The peak and through of the sinusoid corresponds to 100% and −100%, respectively. Coloured shadings indicates concurrent time in both 1D and 2D representations**.**

In the first tracking experiment, the ‘Delay experiment’, I delayed visual feedback of the cursor, to investigate whether submovements were dependent on extrinsic factors. Visual feedback of the cursor was delayed by [0, 100, 200, 300, and 400] ms, in separate conditions. These delay values were chosen based on pilot experiments performed by the author and previous delay experiments performed by other authors (Pew, 1974; Miall, 1996). Preliminary experiments that I performed suggested rapid adaptation (a few seconds) to delays. Therefore delays were switched on a trial-by-trial basis.

In the second tracking experiment, the ‘Spatial perturbation and delay experiment’, I spatially perturbed the cursor at [0, 1, 2, 3, 4, and 5] Hz and delayed it by [0, 200] ms. This experiment was performed to test a hypothesis derived from an original model that supported the extrinsic hypothesis.

Spatial perturbations were added to the cursor position in the tangential to the velocity vector of the target. Note that perturbations were of equal peak angular velocity (equal to the angular velocity of the target) for all 5 perturbation frequencies, implying that the spatial amplitude of perturbation was highest for the 1 Hz perturbation and reduced with increasing perturbation frequency.

Eight healthy human subjects (3 females; age 23–33 years; 1 left-handed) were well-trained at performing the tracking task. Experiments were approved by the local ethics committee at Newcastle University and performed after informed consent, which was given in accordance with the Declaration of Helsinki.

In the ‘Delay experiment’, subjects performed a total of 70 trials, comprising 14 trials per delay condition. In the ‘Spatial perturbation and delay’ experiment, subjects performed a total of 144 trials, comprising 12 trials per condition. At the end of each 20-second trial, subjects were given a score based on how accurately they tracked the target. Subjects were instructed to maximize this score, and would receive a score of 1000 if they tracked the target perfectly. The score (range 0–1000) was made to exponentially decline with increase in position error, to encourage subjects to perform as accurately as possible.

### 2.1.2 Tapping experiment

To investigate the contribution of the feedforward pathway to a feature in subject behaviour that was unexplained by an extrinsic model, an isometric 1D unimanual tapping task was designed (Figure 2.1.2). Subjects tapped with their right index finger to an auditory cue (a beep) presented with an inter-beep frequency of [1, 2, 3, 4, and 5] Hz. Subjects received visual feedback of the cursor controlled but the target position was hidden. Instead, subjects were given an amplitude boundary (set to be

0–100%) between of the hidden target position. Subjects were instructed to control the cursor to the full extent of the amplitude boundary. The force required to move the cursor, and the cursor/target size, were as described in the tracking experiment. Subjects performed a total of 15 trials, comprising three 20 s trials per condition.

Eight healthy human subjects (3 females; age 23–33 years) participated in this experiment (all right-handed). Six of these subjects also participated in the prior tracking experiment.

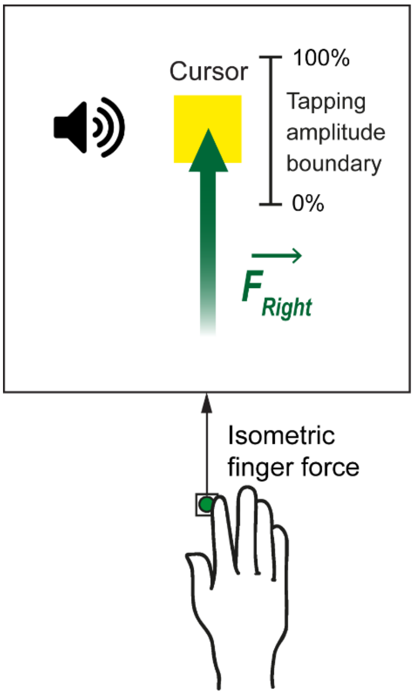

**Figure 2.1.2 Human tapping task.**

Subjects tracked a sonically-cued target, beeping at a frequency of 1–5 Hz. Subjects received visual feedback of cursor position, and had to tap between amplitude boundaries (0–100%). Vertical cursor position was proportional to $\overrightarrow{F_{Right}}$ isometric finger force.

### *2.1.3 Data analysis of tracking experiment*

The main analysis performed in the tracking experiment was calculation of the power spectral density and frequency response of cursor velocity, finger force velocity, and perturbation velocity. These calculations were performed on the middle part of the 20 s long trial (i.e. 1024 samples~10 s).

Power spectral density was calculated using the function *pwelch* in MATLAB with non-overlapping windows of 512 samples. Regression analysis was performed to assess the relationship between submovement frequencies and artificial delays.

To identify submovement peaks in the power spectra of cursor velocity, I smoothed the power spectra with a seven-point moving-average filter, using the function *smooth* in MATLAB.

The amplitude response of the cursor velocity to perturbation velocity was calculated from the complex magnitude of $DFT_{Cursor}(f_{Pert})$ using the function *abs* in MATLAB.

The frequency response of the finger force velocity to perturbation velocity was calculated from complex magnitude and phase of $DFT_{FingerForceVel}(f_{Pert})$ using the function *abs* and *angle* in MATLAB for the gain and the phase response, respectively.

An analysis of variance (ANOVA) approach was used to compare the frequency response across conditions. In addition, tracking performance was reported as root-mean-squared error (RMSE).

Data analysis and statistics were performed in MATLAB (MathWorks), Excel (Microsoft), and SPSS (IBM). Color maps were adjusted for colorblind readers using the online Color Brewer software (Brewer, 2018).

### *2.1.4 Data analysis of tapping experiment*

The main analysis performed in the tapping experiment was calculation of the power spectral density of cursor position. Power spectral density was calculated using the function *pwelch* in MATLAB with non-overlapping windows of 256 samples.

The amplitude response of the cursor position to perturbation position was calculated from the complex magnitude of $DFT_{CursorPos}(f)$ using the function *abs* in MATLAB. ANOVA was performed to compare the amplitude response across conditions.

## 2.2 Monkey experiments

### *2.2.1 Centre-out task*

In order to investigate M1 LFPs during tracking, monkeys were trained to perform an isometric 2D centre-out task on a computer monitor (Figure 2.2.1). Monkeys controlled the cursor by generating isometric flexion-extension (vertical) and radial-ulnar (horizontal) torque with their wrist restrained in a pronated posture. Targets were presented in 8 peripheral positions in a pseudorandom order. Targets were positioned at 70% of the distance to the screen edge (100% corresponding to torque of 0.67 Nm). The diameter of the target and cursor ranged between 14-36%. To probe extrinsic and intrinsic dynamics in M1 LFPs, visual feedback of the cursor was delayed by [0, 200, 400 and 600] ms delivered in separate condition blocks. Two purpose-bred female rhesus macaques (monkey S: 6 years old, 6.6 kg; monkey U: 6 years old, 8.8 kg) participated in the experiment. Analog output of the wrist torque transducer (Nano25; ATI Industrial Automation) was sampled at 488 samples/s (USB-6229; National Instruments), and translated into cursor position on a monitor screen using custom-written code (Delphi 7, Borland). Animal experiments were performed under appropriate UK Home Office licenses in accordance with the Animals (Scientific Procedures) Act 1986.

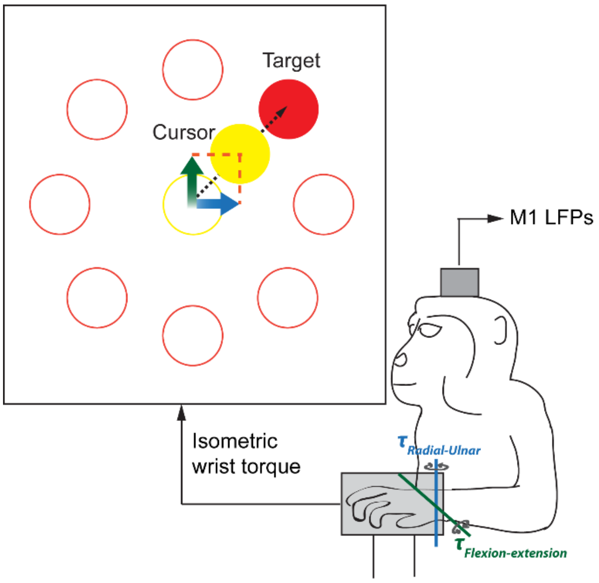

**Figure 2.2.1 Monkey centre-out task.**

Monkeys controlled the position of a cursor to acquire a target presented in a centre-out sequence on a monitor screen. Cursor position was proportional to $\tau_{Radial-ulnar}$ (horizontal) and $\tau_{Flexion-extension}$ (vertical) isometric wrist torque. Multichannel LFPs were recorded from the motor cortex (M1).

### 2.2.2 Surgical procedure and LFPs recording

A custom array of 12 moveable 50 µm diameter tungsten microwires (impedance ~200 kΩ at 1 kHz) was implanted into M1. Surgery was performed under sevoflurane anaesthesia with postoperative analgesics and antibiotics. Head-free recordings were made using unity-gain headstages followed by wide-band amplification and sampling at 24.4 kilosamples/s (System 3; Tucker-Davis Technologies). LFPs were digitally low-pass filtered at 200 Hz and recorded at 488 samples/second. M1 LFPs (and contralateral wrist torque) were recorded from left M1 in monkey S and in left (45 recording days) and right (44 recording days) M1 in monkey U.

### *2.2.3 Data analysis*

I differentiated the magnitude of the absolute 2D torque (expressed as a percentage of the distance to the edge of the screen) to obtain radial cursor velocity (expressed as %/s).

When performing frequency analysis, I removed the task-locked component by subtracting the average velocity across trials, to better visualise submovements. LFP channels were subjected to visual inspection to reject noisy LFP channels. I removed the task-locked LFP components by subtracting the average LFPs across trials. Power spectral density of cursor velocity and LFP was calculated using the function *pwelch* in MATLAB with overlapping windows of 16,384 samples.

Submovement frequencies were identified as peaks in the smoothed power spectra of the velocity. Smoothing was performed by convolving each spectrum with a 16 point Hanning window using the function *hanning* in MATLAB. Coherence spectra were calculated between radial cursor velocity and LFP. Submovement-related activity of LFP was also assessed in the time domain. Finally, imaginary cross-spectral density analysis was performed to assess the phase relationship between pairs of LFP channels.

Analysis of kinematics and neural data was performed on data recorded over 8 different days comprising of 56 task blocks in Monkey S (no delay: 24 blocks; 200 ms delay: 13; 400 ms delay: 13; 600 ms delay: 6), and 89 recording days comprising of 356 task blocks in Monkey U (no delay: 89; 200 ms delay: 89; 400 ms delay: 89; 600 ms delay: 89). Each task block comprised 50 (monkey S) or 70 trials (monkey U), performed contiguously with a single delay throughout. Between some recording days in Monkey U, the microwires were moved to different cortical depths. Therefore, I divided the 356 task blocks in Monkey U into 15 sets comprising those task blocks (between 12 – 80 per set) during which the microwires were not moved.

# Chapter 3. Origin of submovements during visuomotor tracking

## 3.1 Chapter overview

This chapter will examine whether submovements arise from properties intrinsic to the motor systems of the brain or extrinsic properties of the environment. For example, the frequency of submovements could be imposed by an intrinsic rhythmicity in motor circuits (Hall *et al.*, 2014). Alternatively, the rate of submovements could depend on extrinsic factors such as the delay inherent in visual feedback of movements (Pew, 1974; Miall, 1996).

In this chapter, I re-examined whether submovements depended on extrinsic properties in tracking tasks by artificially increasing visual feedback delays. I found that submovement frequencies depended systematically on visual feedback delay. Furthermore, simulations of a delayed feedback controller reproduced submovement frequencies and their dependency on visual feedback delay. My model made further predictions about the human amplitude response which I then tested by delivering perturbations in the form of tangential cursor displacements at different frequencies. The result of these experiments suggest that submovements occur as a result of noise exacerbation.

## 3.2 Effect of visual feedback delay on submovement frequencies

### *3.2.1 Aim*

The aim of this section was to develop a novel visuomotor tracking task to accurately assess submovement structure, in order to test the effect of artificially increasing visual feedback delays. In such a task, if submovements are not affected by feedback delay, this supports the intrinsic hypothesis. Conversely, if submovements *are* affected by delay, then this supports the extrinsic hypothesis.

### *3.2.2 Methods*

Eight participants performed an isometric 2D visuomotor tracking task (section 2.1.1). Visual feedback of the cursor was delayed by [0, 100, 200, 300 and 400] ms in separate conditions (Figure 3.2.1 (A)), which were delivered in pseudorandom order.

Submovement frequencies were identified as peaks in the smoothed power spectra of the angular velocity (frequency resolution=0.098 Hz). A seven-point moving-average filter was used to smooth the power spectra. Submovement peaks were converted to submovement periods by calculating the inverse of the frequency peak. A linear regression line was fitted to each submovement harmonic group.

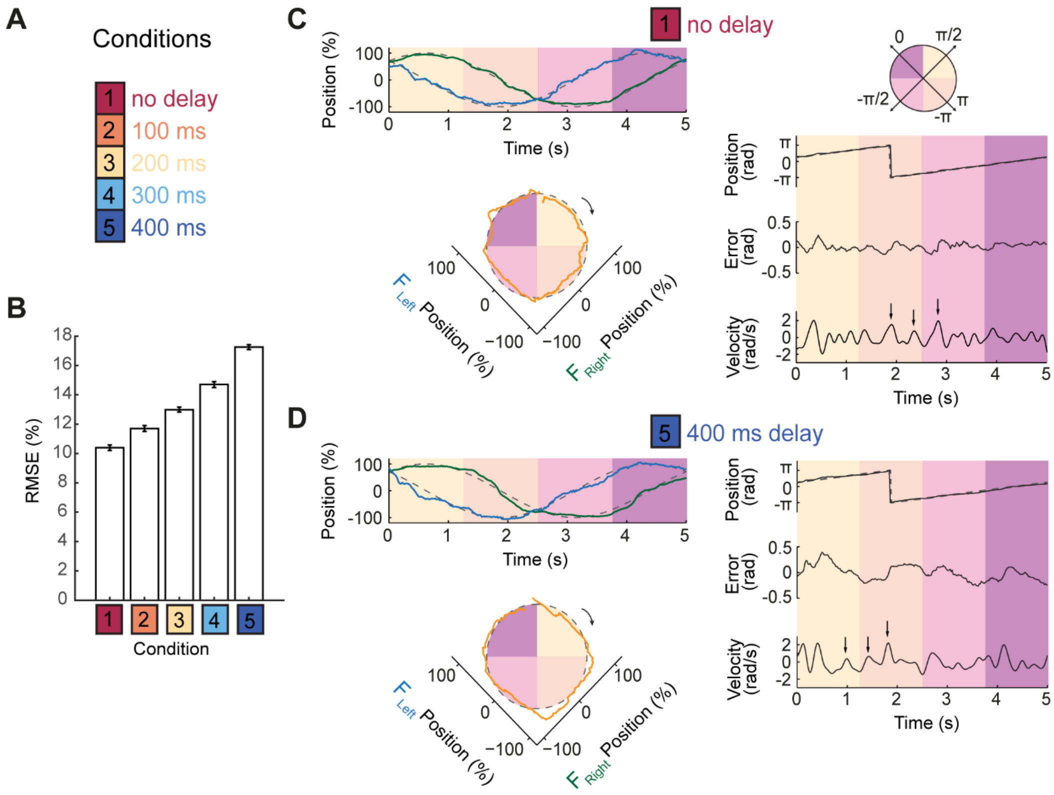

**Figure 3.2.1 Task design, performance, and examples of delay experiment.**

**(A)** Eights subjects performed a finger-force tracking task in which artificial delays ($T_{art}$) were added to the visual feedback of the cursor in separate conditions. **(B)** Average performance across subjects (n=8), shown as root-mean-squared error (RMSE) with plus/minus standard error. **(C)** Example traces of position and velocity in the no delay condition. Finger-force position over time (*top left*) and 2D cursor position (*bottom left*) for one target revolution. Dashed line indicates target position. Coloured shading indicates concurrent times in 1D and 2D traces. The angular position of the cursor (*top right*) was calculated and from this was subtracted the angular position of target (*middle right*). Angular error was differentiated to obtain velocity (*bottom right*) which was then used for further analysis. Velocity was low-pass filtered and three examples of submovements are indicated by arrows. **(D)** The same as (C), but for the 400 ms delay condition.

### *3.2.3 Analysis of performance and power spectra*

All subjects were able to perform the task to a similar degree of performance after training (Figure 3.2.1 (B)). Performance (measured using RMSE) was worse with longer delays in visual feedback.

Examples of un-delayed and delayed position and velocity traces can be seen in Figure 3.2.1 (C, D). Submovements can be seen as fluctuations in cursor velocity. To assess at what frequency these submovements occurred, I calculated the power spectral density of velocity. I identified clear peaks in the power spectra of cursor velocity in individual spectra, and in the average over subjects (Figure 3.2.2 (A-B)).

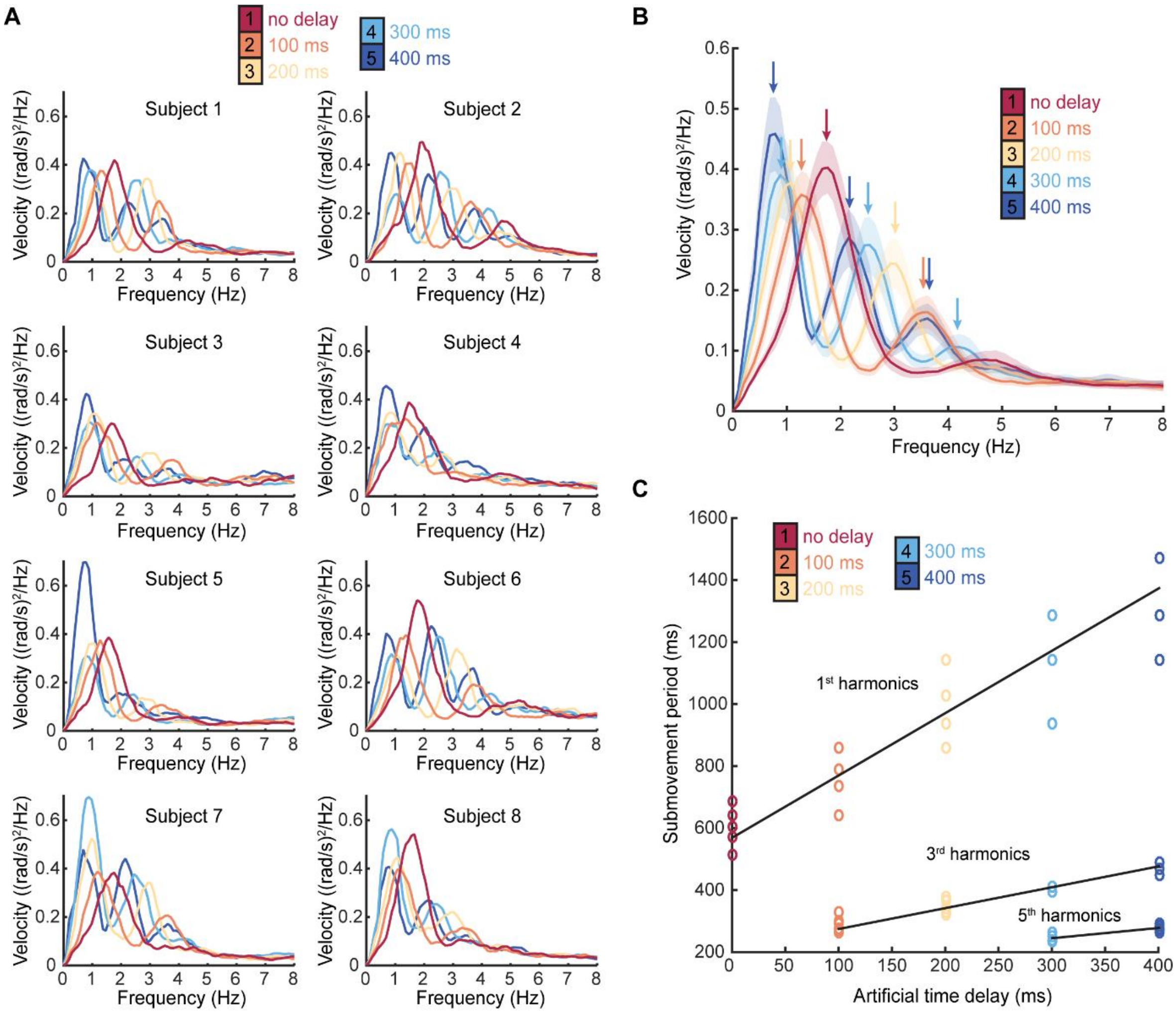

**Figure 3.2.2 Effect of visual feedback delay on submovement frequencies.**

**(A)** Smoothed power spectra of the cursor velocity of individual subjects. **(B)** Smoothed average over subjects (n=8) of power spectra of the cursor velocity with shading indicating plus/minus standard error. Power spectra of different delay conditions are overlaid. Arrows indicate submovement frequency peaks. **(C)** Submovement periods are plotted for all five time delay conditions and regression lines fitted for each harmonics group.

When no delay was added, there was a clear peak at 2 Hz. A smaller peak at 5 Hz was seen in some subjects (e.g. subject 2) and in the average. These two peaks shifted to lower frequencies as more delay was added. A third peak could be seen when a delay of 300 or 400 ms was added. At 300 ms these peaks occurred at around 1, 2.5 and 4 Hz. As the second and the third peaks occurred close to the third and fifth harmonics of the first peak, I labelled these peaks as ‘1st harmonic’, ‘3rd harmonic’, and ‘5th harmonic’. Higher harmonic peaks of submovements had smaller amplitude, but this amplitude increased as their frequency decreased with more delay.

### *3.2.4 Linear fitting of submovement harmonics*

Next, I identified peaks in the power spectra of cursor velocity (corresponding to submovement frequencies) and converted these into submovement periods by calculating their inverse. For each subject I plotted submovement periods against the corresponding artificial delay given in a particular condition (Figure 3.2.2 (C)).

There was a clear relationship between artificial time delay and submovement periods for each harmonic group. To assess this relationship I performed linear regression of the submovement period against time delay (Figure 3.2.2 (C) and Table 3.2.1), resulting in (unitless) gradients of 1.89, 0.59, and 0.33 for the 1st, 3rd, and 5th harmonic groups, respectively. The lines fitted to the data explained the data well ($F(1, 38) = 354.94$ $p<0.00001$, $F(1, 30) = 453.14$ $p<0.00001$, $F(1, 14) = 41.03$ $p<0.00001$, and $r^2 = 0.90$, $r^2 = 0.94$, $r^2 = 0.75$ for the 1st, 3rd, and 5th harmonic groups, respectively).

**Table 3.2.1 Linear fitting of submovement harmonics.**

Shown in the table are the gradients and intercepts of the regression lines fitted for each harmonic group of submovements. Shown in square brackets are 95% confidence intervals of these values.

| | **Gradient** | **Intercept** | $r^2$ | $F$ | $p$ |
|---|---|---|---|---|---|
| 1st harmonic | 1.89<br>[1.69,2.09] | 588.8 [539.08,638.52] | 0.90 | 354.94 | <0.00001 |
| 3rd harmonic | 0.59<br>[0.53,0.65] | 226.31<br>[210.79,241.84] | 0.94 | 453.14 | <0.00001 |
| 5th harmonic | 0.33<br>[0.22.0.45] | 145.75<br>[106.24,185.26] | 0.75 | 41.03 | <0.00001 |

### *3.2.5 Summary*

I developed a novel bimanual visuomotor tracking task that was able to characterise submovements clearly, as seen in the peaks of the power spectra of the cursor velocity. I tested whether submovement frequencies depended on visual feedback delay and found a systematic relationship between delay and submovement frequency. This finding supports the hypothesis that submovement frequency depends on extrinsic factors.

## 3.3 A feedback controller to model submovement frequencies

### *3.3.1 Aim*

In the preceding section, I found that when visual feedback was delayed, submovement frequencies shifted to lower frequencies. This result could perhaps be explained by a feedback controller monitoring visual feedback of position. The aim of this section was to develop a computational model of visuomotor tracking to explain the results of the preceding section.

### *3.3.2 Methods*

For simplicity, I modelled a 1D feedback controller of position (Figure 3.3.1 (A)). A 1D sinusoidal target of 0.2 Hz frequency served as the reference signal and was represented by a feedforward command ($r_t$). The motor command ($u_t$) combined this feedforward command ($r_t$) with a corrective signal arising from feedback (observed error ($z_t$).

The motor command ($u_t$) was corrupted by motor noise ($w_t$) (with a 1/f spectrum) and the sum resulted in finger-force ($ff_t$). The cursor position ($x_t$) (proportional to the finger-force ($u_t$) was delayed (visual delay ($T_v$)) and corrupted by visual noise ($v_t$) (with a white noise spectrum), and the sum resulted in visual feedback ($y_t$).

Feedback controllers with delayed sensory signals can be unstable. One solution to this is to use a Smith Predictor which uses internal feedback based on an efference copy. Thus, a Smith predictor predicts the sensory consequences of movement by using knowledge of the delay in the feedback loop. In my model, the motor command ($u_t$) was delayed by the Smith predictor, resulting in a prediction of visual feedback ($y'_t$). This was compared with the visual feedback ($y_t$) to produce the observed error ($z_t$).

The internal visual delay ($T_v$) was assumed to be 260 ms. The effect of visual feedback delay on submovement frequencies was tested by adding artificial time delays ($T_{art}$) of [0, 100, 200, 300, and 400] ms.

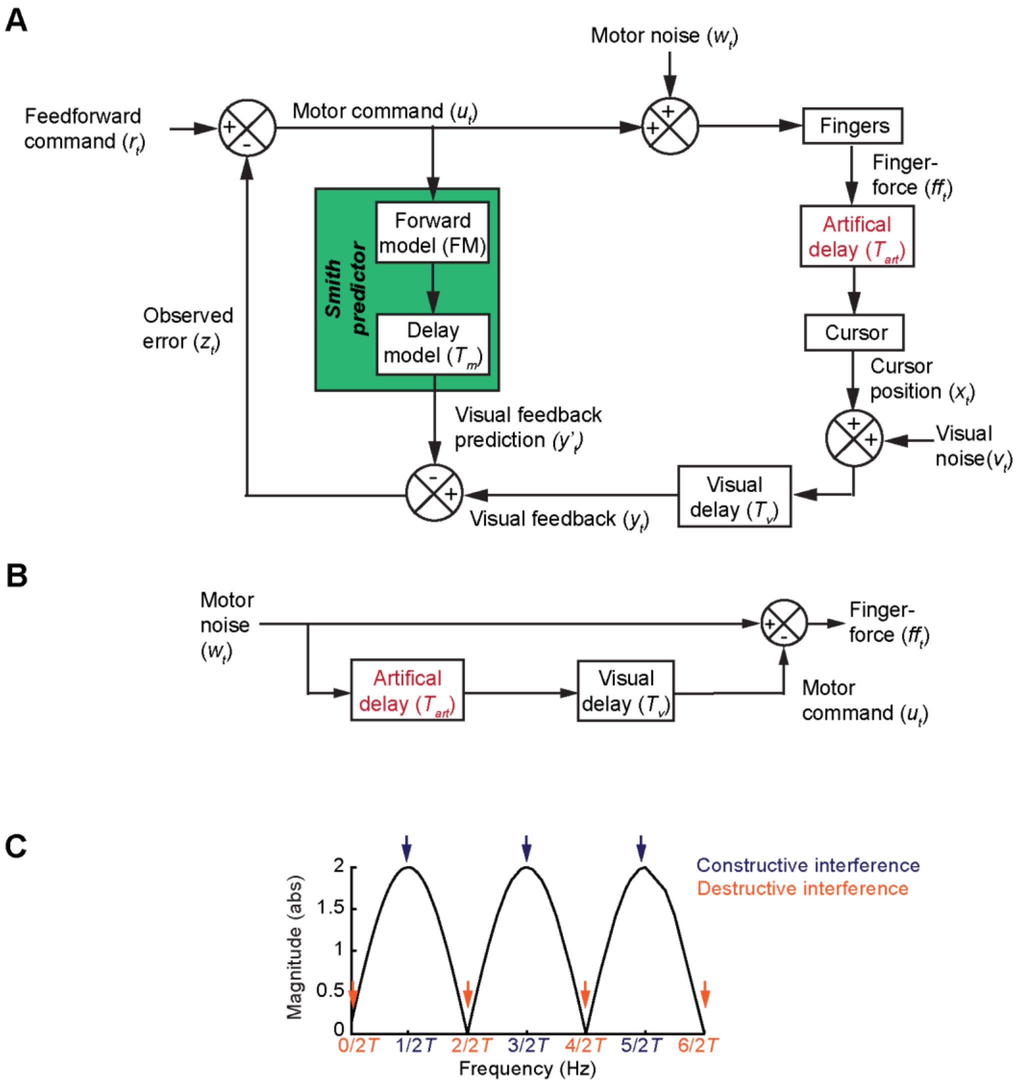

**Figure 3.3.1 Schematic of visuomotor tracking model and its comb filter amplitude response.**

**(A)** The motor command ($u_t$) is driven by delayed correction of noise in the feedback loop. **(B)** A Smith predictor allows the schematic to be redrawn into a feedforward comb filter. In this simplified schematic, the motor noise ($w_t$) is summed with the negatively delayed version of itself (as part of the motor command ($u_t$), leading to constructive and destructive interference of motor noise in the finger-force ($ff_t$). **(C)** The amplitude response of the model is a periodicity of peaks and troughs (see arrows), the frequencies of which are dependent on the total time delay ($T$) in the feedback loop. Filters with such properties in the amplitude response are commonly referred to as ‘comb filters’. See the text for further details.

### *3.3.3 Feedback controller exhibited comb filtering properties*

A schematic of my model is shown in Figure 3.3.1 (A). Visual feedback ($y_t$) comprises the delayed motor command ($u_{t-T}$) and delayed visuomotor noise ($w_{t-T} + v_{t-T}$). An accurate prediction of the sensory consequences of movement by the Smith predictor would result in the visual feedback prediction ($y'_t$) equalling the delayed motor command ($u_{t-T_m}$). In this scenario, the visuomotor noise in the feedback loop can be distinguished from the motor command by subtracting off the visual feedback prediction (${y'}_t$) from the visual feedback ($y_t$). Thus, the feedback correction (observed error ($z_t$) would comprise the delayed visuomotor noise ($w_{t-T} + v_{t-T}$). Consequently, the finger-force would consist of the sum of the delayed visuomotor noise ($w_{t-T} + v_{t-T}$) arising from feedback correction and current motor noise ($w_t$).

Whilst this visuomotor tracking model (Figure 3.3.1 (A)) appeared complex at first glance, I reasoned that the model could be simplified into a finite impulse response (FIR) filter (specifically, a feedforward comb filter, Figure 3.3.1 (B)), because the Smith predictor allows the output of the filter (finger-force, $ff_t$) to be independent from its previous output. In the resulting, simplified schematic, the motor noise ($w_t$) is summed with the negatively delayed version of itself, resulting in constructive and destructive interference of motor noise ($w_t$) in the finger-force ($ff_t$). Note that this simplified model of signal flow concentrates on the motor noise pathways. The amplitude response of this model can be shown to consist of a periodicity of peaks and troughs (hence ‘comb’ filter), the frequencies of which are dependent on the total time delay ($T$) in the feedback loop (Figure 3.3.1 (C). Peaks occur at frequencies where the corrective signal arising from feedback (delayed noise) is in-phase with the signal itself (noise), resulting in constructive interference (at odd harmonics [$^1/_2\, T, {}^3/_2\, T, {}^5/_2\, T$, etc.]). Troughs occur at frequencies where the corrective signal arising from feedback (delayed noise) is in anti-phase with the signal itself (noise), resulting in destructive interference (at even harmonics [$^0/_2\, T, {}^2/_2\, T, {}^4/_2\, T$, etc.]).

The amplitude response of this model resembled the submovement spectra seen during human visuomotor tracking (see section 3.2). The shift in submovement frequencies when artificial delays were added can be accounted for by the frequency-dependent phase shift of noise in response to a time delay, which when summed with the current noise, would change the frequencies at which constructive and destructive interference occurs.

### *3.3.4 Simulation of the effect of delay on submovement frequencies*

I performed a computer simulation of the tracking task, in which the behaviour of the 'subject' was described by the model given above. I studied the effect of introducing delays of [0, 100, 200, 300 and 400] ms to the visual feedback of cursor position (Figure 3.3.2).

I observed fluctuations in the velocity trace generated by the simulation that were very similar to the submovements I saw in my data from human subjects. The model also predicted a decline in performance of the subject with longer delays (Figure 3.3.2 (C)), consistent with the experimental performance of human subjects ($r^2 = 0.95$, $F(1, 3) = 61.00$, $p < 0.0001$). Power spectra of velocity revealed peaks and troughs (Figure 3.3.2 (D)) resembling the experimental submovement spectra (Figure 3.2.2 (B)). Without artificial delay added (see the red trace and arrows) there was a peak at 2 and 6 Hz. Without artificial delay added (Figure 3.3.2 (D), *red trace* and *arrows*) there was a peak at 2 Hz and 6 Hz. These peaks shifted to lower frequencies with longer delays. However, the peaks were of equal power at all frequencies (Figure 3.3.2 (D)) unlike the peaks in subjects, which reduced in size with increasing frequency (Figure 3.2.2 (B)).

The model predicted submovement frequencies occurring at, $f_{1st} = {}^{1}\!/_{2}T$, $f_{3rd} = {}^{3}\!/_{2}T, f_{5th} = {}^{5}\!/_{2}T$ for the 1st, 3rd, and 5th harmonics, respectively (Figure 3.3.1 (C)). Submovement periods ($t_{subm}$) were derived by calculating the inverse of the submovement frequencies: $t_{1st} = 2T,\ t_{3rd} = {}^{2}\!/_{3}T, t_{5th} = {}^{2}\!/_{5}T$ for the 1st, 3rd, and 5th harmonics, respectively. Thus, the relationship between delay and submovement period ($t_{subm}$) could be described linearly with slopes of $2$, ${}^{2}\!/_{3}$, and ${}^{2}\!/_{5}$ for the 1st, 3rd and 5th harmonics of submovement frequencies, respectively. These slopes fell within the confidence intervals of the gradients derived from human experimental data (see Table 1.5.1).

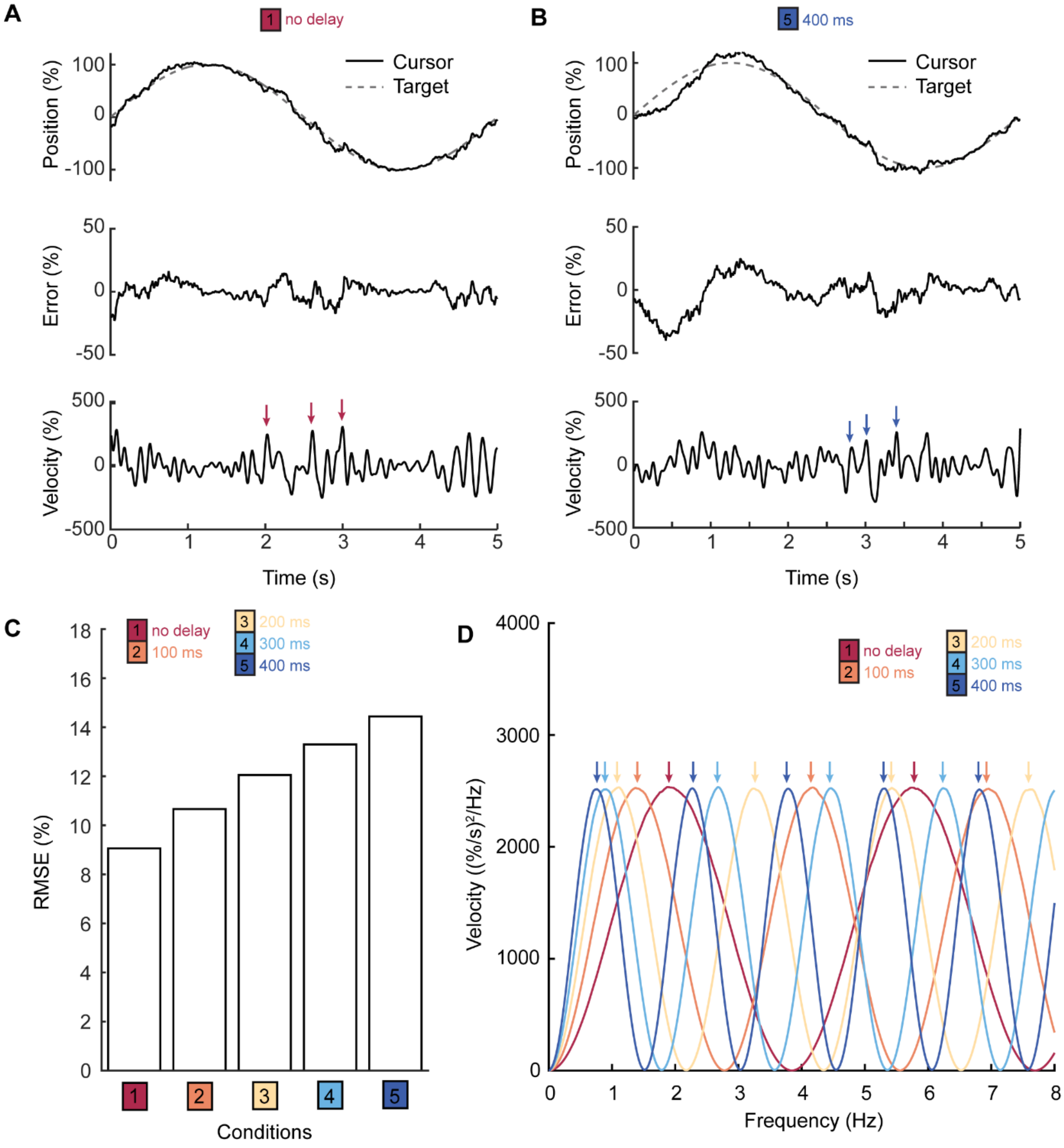

**Figure 3.3.2 Simulation of the visuomotor tracking model and the effect of delay on submovement frequencies.**

**(A)** Example traces of position and velocity in the no delay condition. To better visualise submovements, I subtracted the target position from the cursor position. Velocity was low-pass filtered and three examples of submovements are indicated by arrows. **(B)** The same as (A), but for the 400 ms delay condition. **(C)** Performance across delay conditions is shown as RMSE. **(D)** Smoothed power spectra of cursor velocity of different delay conditions, overlaid. Arrows indicate submovement frequency peaks.

### *3.3.5 Summary*

I developed a computational model of visuomotor tracking, which was able to model the frequency peaks (corresponding to submovements) in the velocity traces of human subjects. The model consisted of a feedback controller, incorporating a Smith predictor, which allowed prediction of the delayed consequences of movement. Submovement frequencies arose from constructive and destructive interference of noise which led to peaks and troughs in the power spectra. The model reproduced the systematic relationship between delay and submovement period found in my experimental data. However, the model was not able to explain the reduced power of submovement peaks at higher frequencies seen in subjects. (In the simulation, submovement peaks were of equal power at all frequencies.)

## 3.4 Human amplitude response to sinusoidal spatial perturbations during tracking

### *3.4.1 Aim*

The above modelling suggests that submovement frequencies arise from feedback correction to visuomotor noise, which leads to constructive and destructive interference of noise in finger-force. The model predicts that, at submovement frequencies, noise is exacerbated, and at other frequencies, noise is reduced. This pattern of signal amplification and reduction can be seen clearly in the amplitude response of the model in response to noise (Figure 3.3.1 (C)).

This interpretation leads to a surprising inference: that submovements seen in human tracking behaviour reflect *exacerbation* of noise at certain frequencies. Therefore, one could hypothesise that humans might be worse at correcting for noise at submovement frequencies, and better at correcting for noise at other frequencies. To test this hypothesis, I injected artificial noise (in the form of visual feedback perturbations) into the tracking task at several frequencies, and observed the human amplitude response.

### *3.4.2 Methods*

Eight participants performed an isometric 2D visuomotor tracking task (section 2.1.1). Sinusoidal perturbations of [1, 2, 3, 4, and 5] Hz were added to the visual feedback of the cursor in separate conditions. Perturbations of equal velocity were added to the cursor position in a direction tangential to the velocity vector of the target. To test the dependency of the magnitude response on delay, I added a delay of 200 ms to the visual feedback of the cursor during half of the trials. In total there were 12 conditions (Figure 3.4.1 (A)), delivered in a pseudorandom order.

According to the model introduced in section 3.3 (see Figure 3.3.1), a perturbation added to the visual feedback of the cursor would be combined with a correction arising from feedback. The sum of a perturbation and a delayed response would be predicted to result in comb filtering (amplification and reduction of the perturbation) in the cursor. I hypothesised that humans would be worse at correcting for perturbations at submovement frequencies and better at other frequencies. Moreover, I expected that the frequencies at which humans were worse at correcting for perturbations would shift in accordance with the shift in submovement frequencies when artificial delay was added.

Cursor responses to perturbation were identified as peaks in the power spectra of angular velocity at perturbation frequencies (frequency resolution = 0.098 Hz). The gain of the cursor in response to the perturbation was calculated for each perturbation frequency. Simulations were performed using the model introduced in section 3.3, by adding 1D sinusoidal perturbations of equal velocity to the cursor position ($x_t$) in the direction of the target.

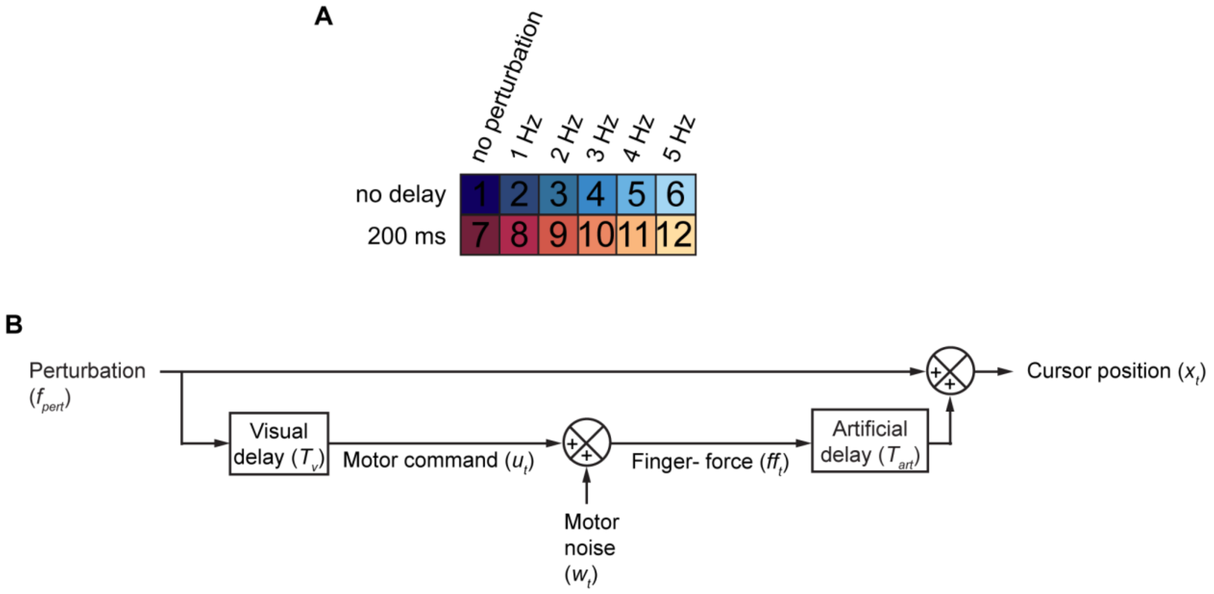

**Figure 3.4.1 Task design of spatial perturbation and delay experiment.**

**(A)** Perturbations ($f_{pert}$) of [0, 1, 2, 3, 4 and 5] Hz and artificial delays ($T_{art}$) of [0, 200] ms were added to the visual feedback of the cursor in separate conditions. **(B)** Diagram of the model's prediction when perturbations were added to the visual feedback of the cursor. Perturbations would be combined with a correction arising from feedback and result in comb filtering (frequency dependent amplification and reduction) in the cursor position. Note that this simplified model of signal flow concentrates on the perturbation and motor noise pathways.

### 3.4.3 Analysis of performance and example

All subjects were able to perform the task to a similar degree of performance after training (Figure 3.4.2 (A)). In the no-delay conditions (conditions1–6), RMSE was highest in the 1 Hz perturbation condition (condition 2), and reduced with increasing perturbation frequency. This decline in performance with increasing perturbation frequency could be attributed to the reduced amplitude of perturbations (corresponding to equal velocity) with increase in perturbation frequency. A similar observation was seen in the simulated data (Figure 3.4.2 (B)).

In both the experimental and simulated data, the highest RMSE across all conditions occurred with a 1 Hz perturbation and 200 ms delay (condition 8). Since submovements occurred at 1 Hz when a 200 ms delay was added (see yellow trace in Figure 3.2.2 (B)) the high RMSE in the 1 Hz condition could be a result of in-phase corrections to perturbation which led to further exacerbation of error.

Following this line of thought, one would also expect a higher RMSE in the 3 Hz condition (condition 10) because submovements also occurred at 3 Hz when a 200 ms delay was added (e.g. see yellow trace in Figure 3.2.2 (B)). Indeed a slightly higher RMSE was seen in condition 10 although not as high as in condition 8. The smaller RMSE in condition 10 could be attributed to the smaller amplitude of the 3 Hz perturbation compared to the amplitude of the 1 Hz perturbation.

If exacerbation of perturbation occurred at submovement frequencies and affected RMSE, I would expect RMSE to be highest when a 2 Hz perturbation was added under no delay (condition 3). However, the highest RMSE under no delay was in the 1 Hz perturbation condition. This can be explained by the RMSE being affected by both the perturbation amplitude and the feedback response. The pattern of performance across conditions found in the subjects was well predicted by the model ($r^2 = 0.89$, $F(1, 10) = 77.35$, $p < 0.0001$).

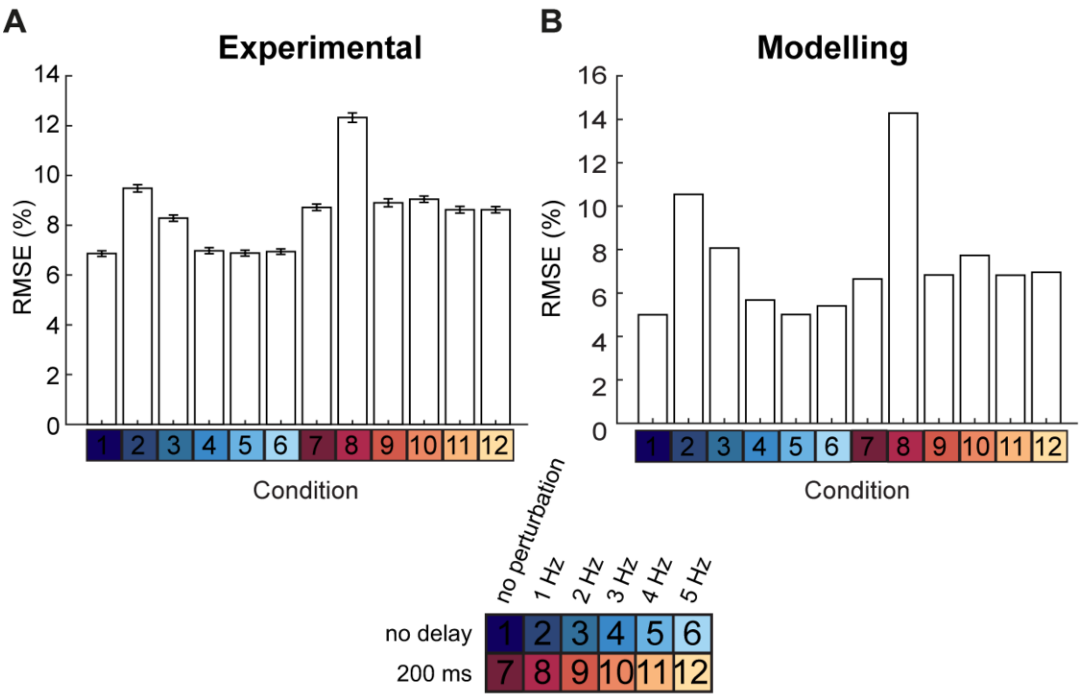

**Figure 3.4.2 Performance of participants and model in spatial perturbation and delay experiment.**

**(A)** Average performance across subjects (RMSE ± standard error; n = 8)**. (B)** Performance of the model.

When no artificial delay was added, submovements occurred at 2 Hz (see *red trace* in Figure 3.2.2 (B)) and therefore I expected perturbations to be exacerbated at this frequency. This was indeed predicted by the model (Figure 3.4.3 (C)) and seen in the example subject (Figure 3.4.3 (A)). When the 2 Hz perturbation was added, clear fluctuations were seen in the position trace of this subject, indicating that the perturbation had not been eliminated. In comparison, the position trace when 3 Hz perturbation was added did not have these fluctuations, and instead looked much smoother (Figure 3.4.3 (B, D)). This could also be due to reduced amplitude of the 3 Hz perturbation compared to the 2 Hz perturbation.

In both the experimental (e.g. Figure 3.4.3 (A)) and model-derived data (e.g. Figure 3.4.3 (C)), a clear in-phase relationship was observed between perturbation (*grey*) and finger-force (*red*) and between finger-force (*red*) and cursor (*black*) when a 2 Hz perturbation was added. This in-phase summation of perturbation and finger-force lead to constructive interference in cursor, and resulted in amplification of the perturbation. In contrast, an out-of-phase relationship was observed between perturbation (*grey*) and finger-force (*red*) and between finger-force (*red*) and cursor (black) when a 3 Hz perturbation was added (Figure 3.4.3 (B, D)). This out-of-phase summation of perturbation and finger-force lead to destructive interference in cursor, and resulted in a reduction in perturbation.

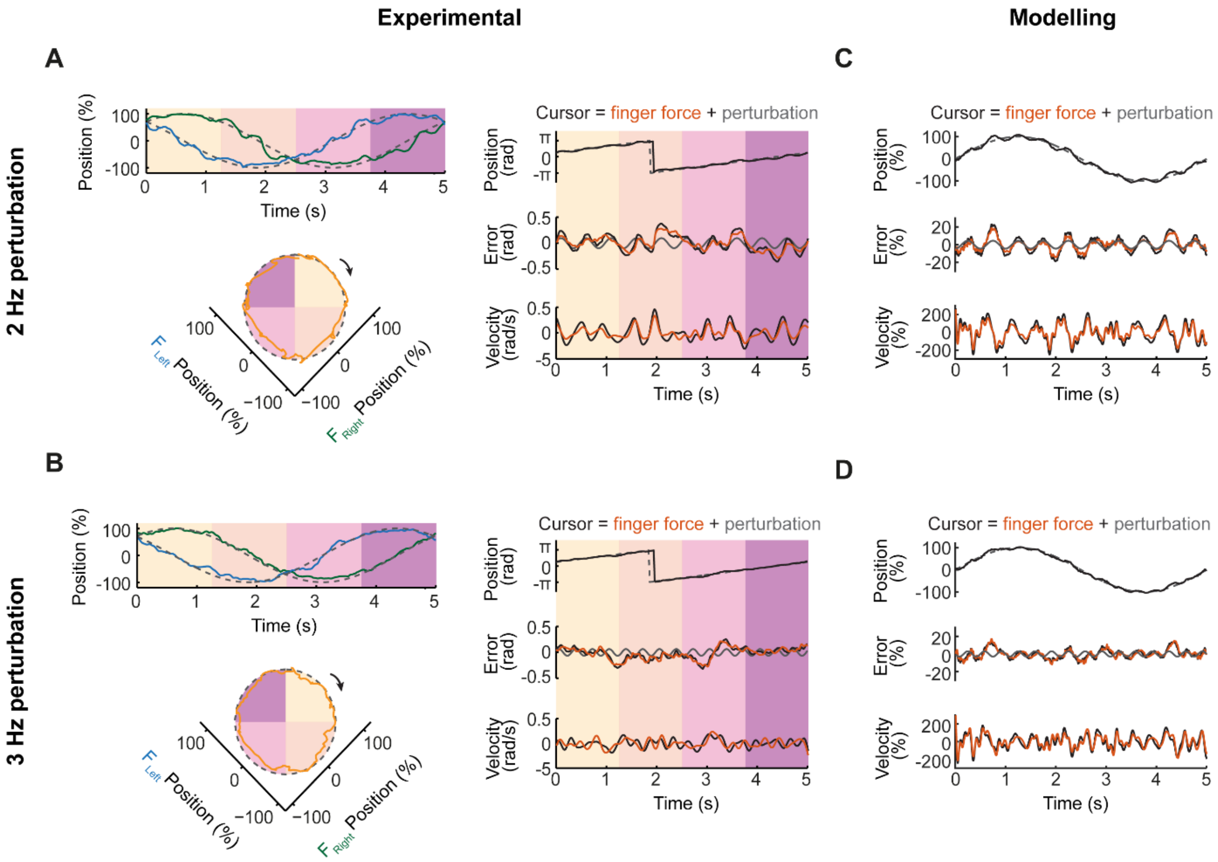

**Figure 3.4.3 Examples of tracking data, from an example subject (left) and generated by the comb filter model (right), in the perturbation and delay experiment.**

**(A)** Representative position and velocity traces for an example participant in the 2 Hz perturbation condition. Finger-force position over time (*top left*) and 2D cursor position (*bottom left*) for one target revolution. Dashed line indicates target position. Coloured shading indicates concurrent times in 1D and 2D traces. The angular position of the cursor (*top right*) was calculated and from this was subtracted the angular position of target (*middle right*). Angular error was differentiated to obtain velocity (*bottom right*). Shown is the low-pass filtered velocity. Shown as well is the perturbation angular position and finger-force angular position (*middle right*), and the finger-force velocity (*bottom right*). Angular finger-force position is the cursor angular position minus the perturbation angular position. **(B)** The same as (A), but for the 3 Hz perturbation condition. **(C)** Simulated example traces of position and velocity in the no delay condition. To better visualise submovements, I subtracted the target position from the cursor position. Velocity was low-pass filtered. Shown as well is the perturbation position and finger-force position. Finger-force position is the cursor position minus the perturbation position. **(D)** The same as (C), but for the 3 Hz perturbation condition.

### *3.4.4 Analysis of cursor power spectra and gain response*

To see more clearly how subjects responded to perturbations at different frequencies, I calculated the power spectra of cursor velocity. I observed clear peaks in individual cursor spectra in response to perturbations (Figure 3.4.4) and in the average over subjects (Figure 3.4.5 (B-C)). As in the previous experiment, the baseline submovement spectra exhibited a peak at 2 Hz when no delay was added, and a peak at 1 and 3 Hz when a 200 ms delay was added. The peaks in response to perturbations lay on top of these baseline submovement spectra.

Perturbations at 1 to 5 Hz were given of equal velocity, but the peaks in the power spectra of perturbations showed slightly different amplitudes (Figure 3.4.5 (A)). This is actually an artefact of power spectral estimation, because the Fourier frequencies at which power was calculated do not correspond exactly to integer values (the actual frequency interval being 0.098 Hz, as determined by the sampling rate and the window size).

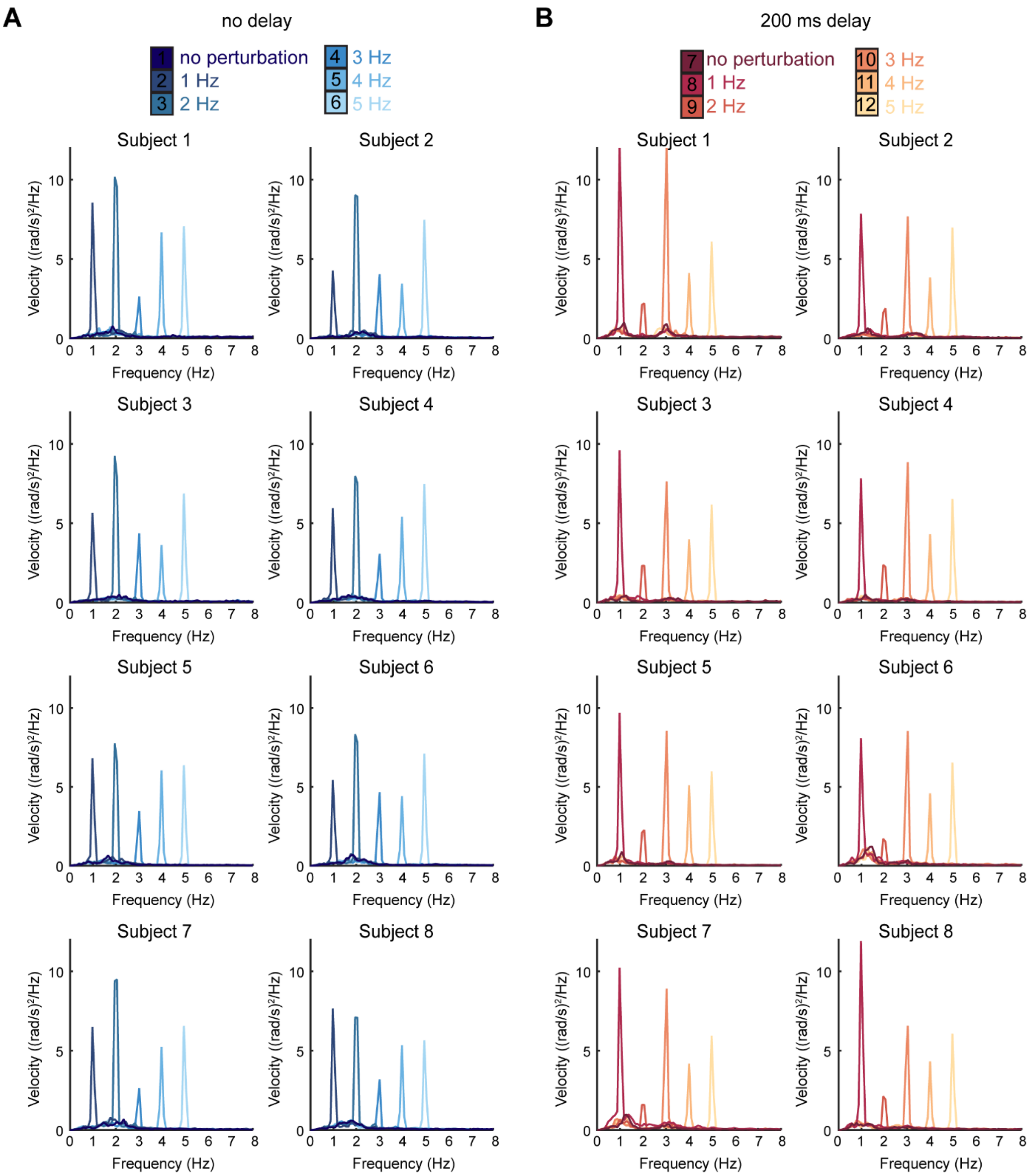

**Figure 3.4.4 Individual power spectra of cursor velocity in response to perturbations.**

**(A)** Power spectra of the cursor velocity of individual subjects in the no delay conditions. **(B)** The same as (A), but for the 200 ms delay conditions. Power spectra under different perturbation conditions are overlaid. Note that perturbation responses occurred on top of a baseline submovement spectrum.

In response to perturbations of equal velocity (Figure 3.4.5 (A)), subjects responded unequally depending on perturbation frequency and delay (Figure 3.4.5 (B, C)). The model predicted that in response to perturbations of equal velocity (Figure 3.4.5 (E)), subjects would exacerbate perturbations at submovement frequencies (Figure 3.4.5 (F, G)). Indeed I found that perturbations were exacerbated by the subjects at 2 Hz when no delay was added and at 1 and 3 Hz when a 200 ms delay was added. Conversely, perturbations were *reduced* by the subjects at 3 Hz when no delay was added and at 2 Hz when a 200 ms delay was added.

To quantify the amplitude response to perturbations, I calculated the gain of the cursor velocity relative to the perturbation (Figure 3.4.5 (D)). I found that—as predicted by the model (Figure 3.4.5 (H))—the gain to perturbations was highest at submovement frequencies and, in the delay conditions, shifted according to the shift in submovement frequencies.

I used ANOVA to compare the effect of perturbation frequency and delay on cursor gain in participants. There was no significant effect of delay $F(1, 70) = 1.239$, $p = 0.270$. There was a significant effect of frequency $F(4, 70) = 30.542$, $p < 0.0001$ and a significant interaction between frequency and delay $F(4, 70) = 110.286$, $p < 0.0001$.

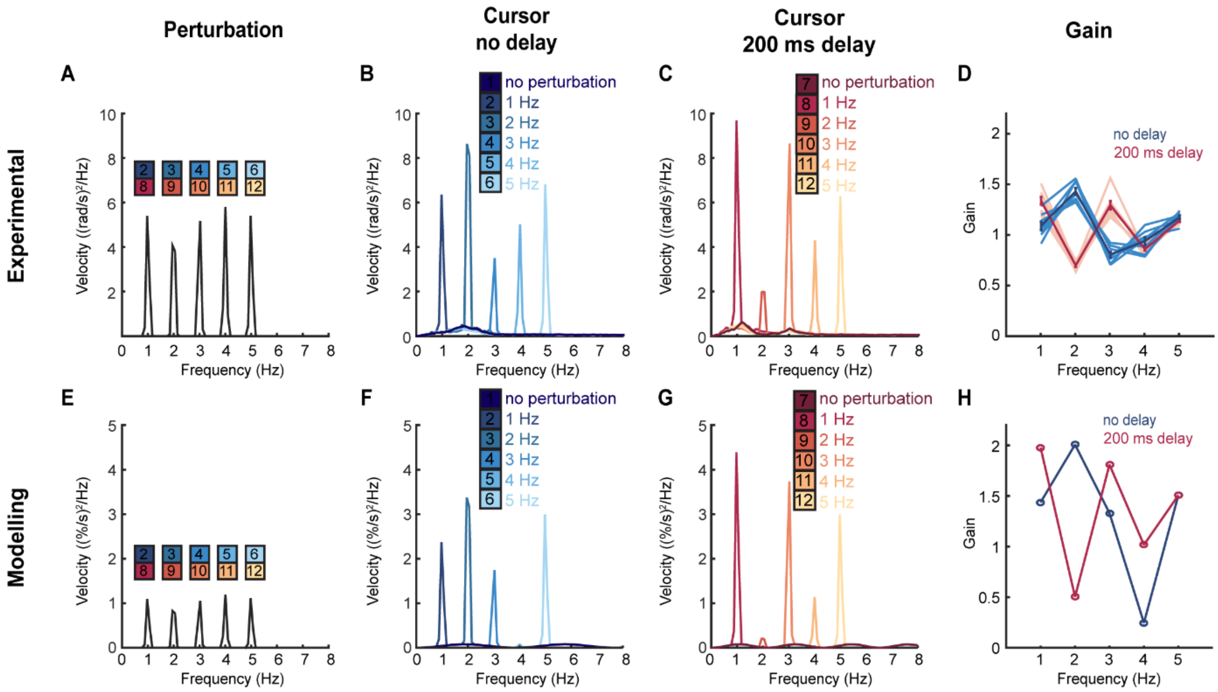

**Figure 3.4.5 Averaged cursor response to perturbations and predictions by model.**

**(A)** Perturbations of equal velocity at 1 to 5 Hz were added to the cursor. **(B)** Averaged power spectra of cursor velocity across subjects (n=8) in the no delay conditions. **(C)** The same as (B), but for the 200 ms delay conditions. **(D)** Cursor gain to perturbations at 1 to 5 Hz with no delay and 200 ms delay. Individual (lighter *blue* and *red*) and average (darker *blue* and *red*) cursor gains across subjects with standard error (n=8) were plotted. **(E-H)** As per (A-D), but for simulated data generated by the model.

### *3.4.5 Summary*

I measured the cursor gain to perturbations during visuomotor tracking, to test the hypothesis that submovements reflect frequencies at which visuomotor noise is exacerbated. If humans responded to noise in the way that the ‘comb filter’ model would predict, I would expect exacerbation of perturbation and submovement frequencies to covary with delay.

Results from human subjects showed that exacerbation of perturbation did indeed occur at submovement frequencies. Moreover, when visual feedback was delayed, the exacerbation of the perturbation shifted in accordance with the shift in submovement frequencies. This suggests that humans produce submovements as a by-product of corrections to error seen in visual feedback.

## 3.5 Discussion

In this chapter, I investigated the origin of submovements during visuomotor tracking. I re-examined whether submovements depend on extrinsic properties in tracking tasks by artificially increasing visual feedback delays. I found a linear relationship between delay and submovement periods. Simulations based on a feedback controller model reproduced submovement frequencies. I measured the human amplitude response to perturbations and found exacerbation of perturbations at submovement frequencies as predicted by the model.

### *3.5.1 Novel bimanual tracking task*

First, I developed a 2D bimanual pursuit tracking task that was able to characterise submovements. Clear peaks of submovements were observed in the power spectra of the cursor velocity. Previously, it has been shown that humans produce smooth movement without clear submovements when performing a pursuit tracking task with a predictable trajectory (Weir *et al.*, 1989). Submovements only became apparent in these experiments when human tracked an unpredictable trajectory in a compensatory manner. In contrast the results I have presented here show that subjects produced clear submovements when they tracked a predictable trajectory in a pursuit manner.

Several factors could explain the clear submovement peaks seen in our data, and the apparent discrepancy with previous findings. Firstly, subjects had to move in an isometric manner, reducing the potential filtering effects of the biomechanics of the limb. This is different to the previous pursuit tracking experiments in which a joystick was used (Weir *et al.*, 1989). Secondly, subjects tracked a completely predictable trajectory of constant speed, as the target underwent uniform circular motion. This prevented subjects from producing speed fluctuations in response to speed changes in the target, perhaps making the speed fluctuations due to submovements more evident. Thirdly, subjects had to move both hands in a 90° out-of-phase coordination pattern. This pattern of movement has been shown to be less stable than the in-phase and antiphase pattern (Zanone and Kelso, 1992). 90° out-of-phase bimanual movement is challenging to perform and require training. Even though subjects performed a predictable pursuit tracking task, the 90° out-of-phase coordination pattern might require a different mode of movement in which subjects could be forced into producing submovements instead of smooth movement.

### *3.5.2 Dependency of delay on submovement frequencies*

The aim of the first experiment in this chapter was to re-examine whether submovement frequencies change when visual feedback is delayed. I replicated previous findings that peaks of submovement frequencies shift with increasing delay (Pew, 1974; Miall *et al.*, 1986; Miall, 1996). I confirmed a systematic relationship between delay and submovement period. This dependency of submovements on delay has also been shown in a patient with peripheral deafferentation (whose condition makes him unable to use proprioceptive feedback) (Miall, 1996), suggesting the main contribution of the visual feedback loop in the generation of submovements. I concluded that submovement frequencies are extrinsically determined by the visuomotor feedback loop.

### *3.5.3 Linear feedback controller reproduced submovements*

Next, I have produced a computational feedback controller model, which successfully reproduces (in simulated data) the submovement frequencies seen in human subjects.

Previous tracking models have included elements which explicitly parse movement into submovements, by introducing non-linearities. One of these models parsed movement after a set period of time (Gawthrop *et al.*, 2011; Sakaguchi *et al.*, 2015). This idea was based on a known phenomenon: the psychological refractory period (PRP) (Vince, 1948). The PRP is a period in which subjects are not able to initiate movement in response to a second stimulus after responding to the first stimulus. Another model parsed movement based on error levels exceeding a set threshold (Gawthrop *et al.*, 2011; Sakaguchi *et al.*, 2015). This idea was based on evidence of an error ‘dead zone’ (Wolpert *et al.*, 1992). An error dead zone is a threshold of positional error that has to be reached before initiation of a new movement. Finally, a previous model parsed movement according to the reliability of an internal model (Sakaguchi *et al.*, 2015). In this model, movement was shortened when the internal model was unreliable.

The model I have developed in this chapter is entirely linear. In this model, submovements represent visuomotor noise, and submovement frequency peaks occur at frequencies at which there is exacerbation of visuomotor noise. It seems counterintuitive to think that submovements arise from the humans’ response to error, but the model was able to reproduce submovements and the shift in submovement frequencies with added delays. Whilst the idea of submovements originating from noise circulating through a delayed feedback loop has been previously proposed (Pew, 1974) this is, to our knowledge, the first time this phenomenon has been simulated via a model.

### *3.5.4 Human’s amplitude response resembled a comb filter*

I tested the prediction that submovement frequencies occur as a result of delayed corrections to errors. To do this, I injected additional noise into the visual feedback of cursor, in the form of a sinusoidal perturbation, and measured the subjects’ response. The model predicted that adding noise to the feedback would result in amplification of noise at submovement frequencies and reduction at other frequencies.

To perform the tracking task well, subjects had to cancel out the added perturbations. If subjects ignored the perturbations, their effect would not be removed from the resulting movement of the cursor, and cursor amplitude response to perturbations would therefore be unity at all frequencies. If subjects managed to correct for the perturbations completely, their effect would be completely removed, and the cursor amplitude response to perturbations would be zero at all frequencies.

My results actually showed that subjects responded unequally to perturbations at different frequencies. Perturbations were amplified at some frequencies, whereas at other frequencies they were reduced. Amplification of perturbations occurred at frequencies at which submovements occurred, and this amplification shifted with delay, as predicted by the model. These results demonstrate that humans have a comb-filter amplitude response, suggesting that submovements occur because of exacerbation of noise, caused by delayed feedback correction of noise.

My ‘comb filter’ model explains how submovement frequencies arise. However, not all features of the human data were reproduced by the model. First, the envelope of the power spectra in the experimental results exhibited a low-frequency bandpass filter, unlike the modelling results, which showed equal power at all submovement frequencies. Second, the cursor gain to perturbation was larger in the simulation than in the experimental data. I will discuss and explore these findings further in the next chapter.

### 3.6 Chapter summary

- I developed a novel 2D bimanual tracking task to characterise submovements.
- Submovement frequencies depend systematically on visual feedback delay.
- Simulations of a feedback controller reproduced submovement frequencies and their dependency on visual feedback delay.
- The model predicted that adding noise to the feedback would result in amplification or reduction of noise (corresponding to the frequency-dependent effect of a comb filter).
- I tested this prediction by measuring the human amplitude response to sinusoidal perturbations during tracking.
- I found amplification and reduction of perturbation signals corresponding to frequencies of peaks and troughs in the submovement spectra.
- When delay was added, perturbation amplification and reduction shifted in accordance with submovement frequencies.
- Taken together, the modelling and experimental results suggest that submovement frequencies are a by-product of delayed corrections to noise detected in the feedback loop.

# Chapter 4. Origin of intrinsic dynamics during visuomotor tracking

## 4.1 Chapter overview

In the preceding chapter, I showed that submovement frequencies were dependent on extrinsic properties of the visual feedback loop and that this could be reproduced by a simple feedback controller model. However, some experimental results were not explained by this model.

Simulations based on our model revealed clear submovement peaks in the power spectra of cursor velocity (Figure 4.1.1 (B)). The first lower frequency peak and the odd harmonic peaks shifted with delay and had equal power, independent of frequency. The overlaid power spectra across different conditions was fitted with an overall envelope, which was uniform, indicating equal power at all frequencies.

The average power spectra of cursor velocity in subjects also revealed clear submovement peaks (Figure 4.1.1 (A)). The first lower frequency peak and the odd harmonic peaks shifted with delay but did not have equal power independent of frequency. The odd harmonic peaks were lower in power compared to the first peak. However, the harmonics peaks increased in power when they were shifted to lower frequencies by the introduction of delay. When the overlaid power spectra across different conditions was fitted with an overall envelope, it revealed a drop-off in velocity-power with increasing frequency, with an apparent passband at 2−3 Hz. This was in contrast to the uniform power distribution seen in the simulated data.

In this chapter, I will investigate the origin of the *delay-independent* low-frequency submovement envelope – which from henceforth I will refer to as the “intrinsic dynamics”. I will go through a series of experiments and eliminative induction to find the source of this intrinsic dynamics.

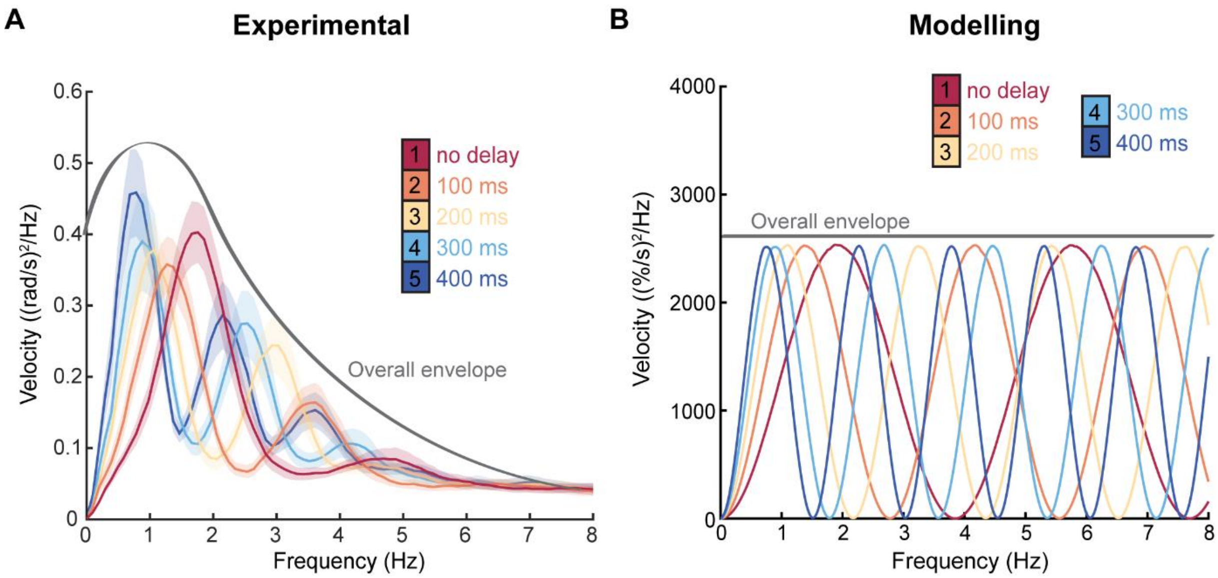

**Figure 4.1.1 Comparison of submovement spectra from experimental and simulated data.**

Average experimental (n = 8) **(A)** and simulated **(B)** power spectra of velocity under different delay conditions. Shading indicates standard error. Note the difference in the overall envelope of the overlaid spectra of different conditions between the experimental and simulated result (drawn by hand for illustration purpose) The overall envelope in the experimental spectra revealed a passband-like profile, whereas the overall envelope in the modelling spectra revealed equal power at all frequencies.

Three plausible sources of the submovement envelope are illustrated in Figure 4.1.2: visuomotor noise (circle 1), a feedforward pathway (circle 2), and a feedback pathway (circle 3).

The first origin of intrinsic dynamics could be the properties of visuomotor noise. In this case, the frequency content of visuomotor noise would determine the amplitude of submovement frequencies. If the submovement envelope reflected the frequency content of visuomotor noise, the power spectra of visuomotor noise would have the same envelope shape. However, measuring visuomotor noise directly is not possible. Instead, I added artificial noise to the visual feedback of the cursor to see whether the envelope of the feedback response was similar to the envelope of artificial noise. I will show in section 4.2 that the amplitudes of the feedback response were not similar to the amplitudes of artificial noise. Instead, the feedback response depended on frequency and revealed low-frequency filtering, resembling the submovement envelope.

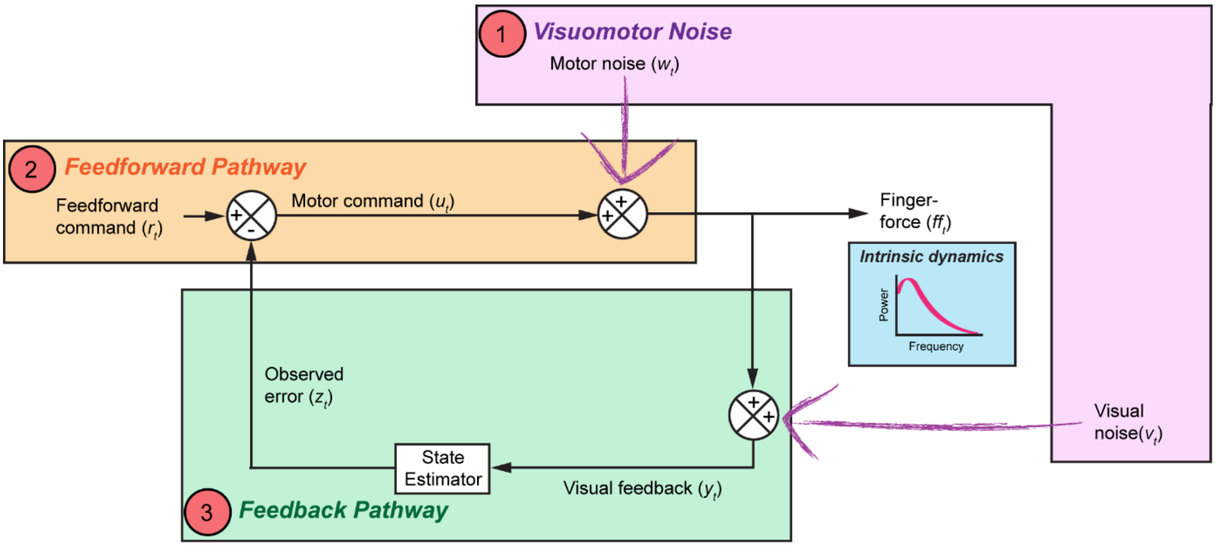

**Figure 4.1.2 Schematic of plausible sources of intrinsic dynamics.**

The low-frequency submovement envelope could reflect properties of visuomotor noise (circle 1), the feedforward pathway (circle 2), or the feedback pathway (circle 3).

The second likely origin of the submovement envelope could be in the feedforward pathway of movement. For example, the muscles could act as a low-pass filter (Partridge, 1965) filtering neural signal sent to the muscles. In this case, the submovement envelope would reflect the muscles' passband. I tested this hypothesis by assessing the feedforward gain at several frequencies in a tapping task to see whether the feedforward gain exhibited a passband at 2–3 Hz. In section 4.3, I show that the feedforward gains were much higher than the gains in response to perturbations during tracking. Moreover, the feedforward gain did not exhibit bandpass filtering. This result suggest that the feedforward processes did not limit feedback responses during tracking and did not impose intrinsic dynamics.

The third possible origin of intrinsic dynamics could be on the feedback side of the movement apparatus. It is unlikely that intrinsic dynamics were imposed by sensory limitations since humans can perceive frequencies of movement higher than 5 Hz (Hecht and Shlaer, 1936). Therefore, I speculated that intrinsic dynamics originated more downstream, in the feedback process that is in the state estimator. I show in section 4.4 that intrinsic dynamics matched features consistent with a state estimator required for optimal feedback control (OFC) in the presence of visual and motor noise.

## 4.2 Finger-force frequency response to perturbations

### *4.2.1 Aim*

The aim of this section was to investigate whether intrinsic dynamics originated from the properties of visuomotor noise. For this purpose, I added artificial noise of equal velocity to the visual feedback of the cursor and measured the finger-force amplitude response. If the low-frequency submovement envelope reflected visuomotor noise, I would expect feedback responses to artificial noise of equal velocity to be level at all frequencies.

### *4.2.2 Methods*

I analysed the same dataset reported in section 3.4. The experimental method has already been described in section 3.4.2. In section 3.4 I analysed the cursor response to perturbations, whereas in this section I analysed the finger-force response to perturbations (Figure 4.2.1 (B)).

According to the ‘comb filter’ model introduced in section 3.3, spatial perturbations added to the visual feedback of the cursor would be combined with a correction arising from feedback which can be observed in the finger-force. If intrinsic dynamics reflected properties of visuomotor noise (i.e. the visuomotor noise spectra has a pass-band like profile), then the feedback response to perturbation would reflect properties of the perturbation (i.e. the feedback response spectra will be equal to the perturbations). Hence, the amplitude response of the finger-force to perturbations would be unity (because the feedback response is dependent on the perturbation amplitude).

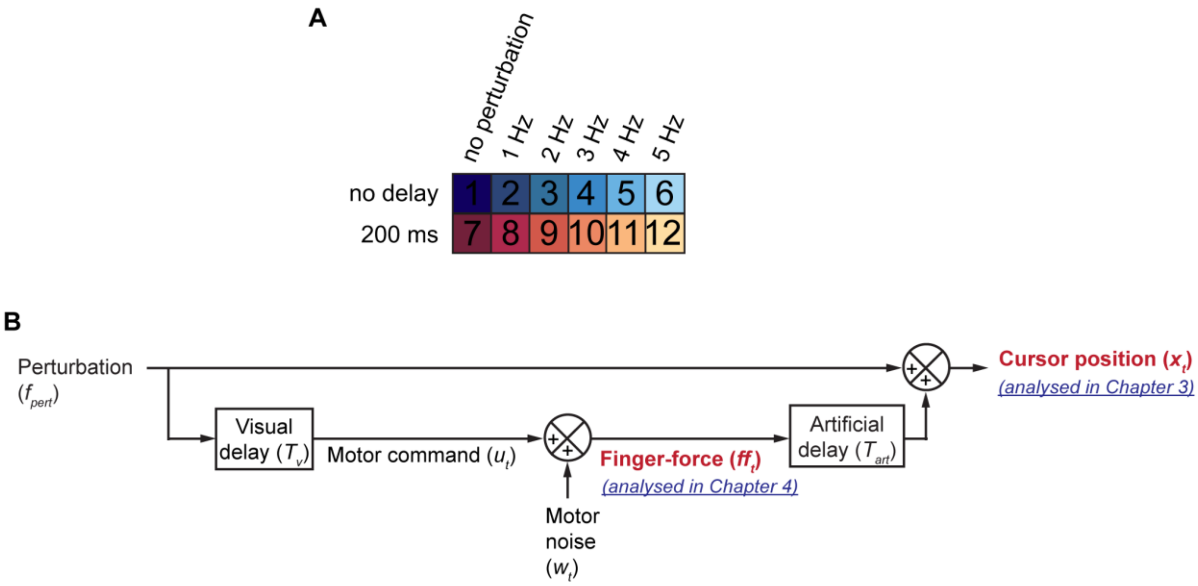

**Figure 4.2.1 Diagram of measured finger-force response to spatial perturbations.**

**(A** Perturbations ($f_{pert}$) of [0, 1, 2, 3, 4 and 5] Hz and artificial delays ($T_{art}$) of [0, 200] ms were added to the visual feedback of the cursor in separate conditions. **(B)** Diagram of the model's prediction when perturbations were added to the visual feedback of the cursor. Note that this simplified model of signal flow concentrates on the perturbation and motor noise pathways. The sum of finger-force and perturbation resulted in the cursor which was analysed in section 3.2.3. In this chapter, I analyse the finger-force response to perturbations. The model predicts that the finger-force would be a negatively delayed version of the perturbation signal (the negative is introduced to correct for perturbation; the delay is introduced by the visual delay). If intrinsic dynamics reflected properties of visuomotor noise, then the feedback response to perturbation would reflect properties of the perturbation.

The finger-force responses to perturbations were identified by peaks in the power spectra of angular velocity at perturbation frequencies. The gain and phase responses to perturbations were calculated at each perturbation frequency and the phase responses were also transformed into a time delay.

For comparison, simulations were performed, based on the 'comb filter' model introduced in section 3.3. To simulate the effect of artificial noise, 1D sinusoidal perturbations of equal velocity were added to the cursor position ($x_t$) in the direction of the target.

### *4.2.3 Analysis of finger-force power spectra and gain response*

To see how subjects responded to perturbations at different frequencies, I calculated the power spectrum of finger force velocity for each subject. I observed clear peaks in response to perturbations finger-force spectra (Figure 4.2.2) from individual subjects, and in the average over subjects (Figure 4.2.3 (B–C)). As was seen in the power spectra of cursor velocity, the peaks in response to perturbations lay on top of the baseline submovement spectrum.

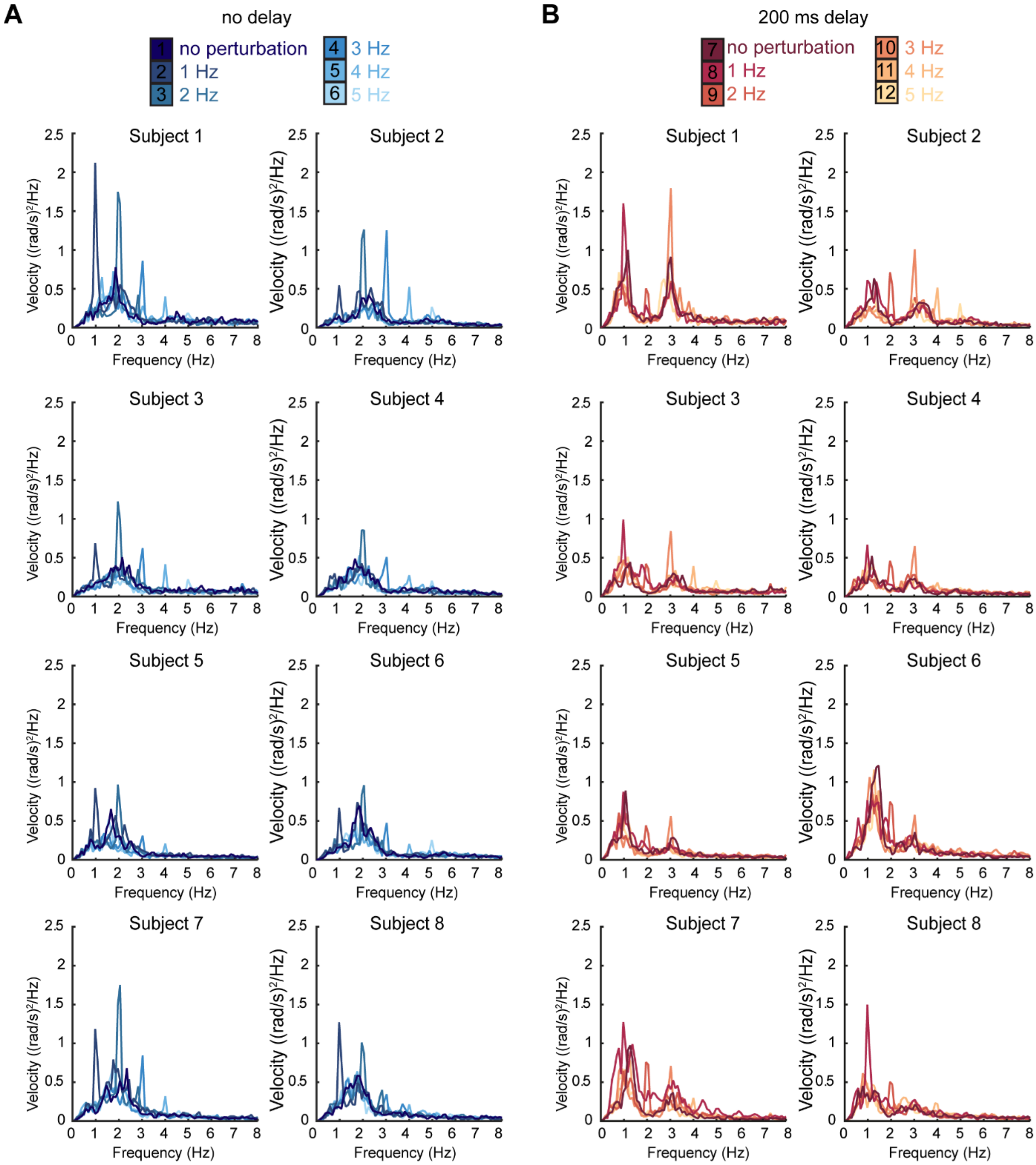

**Figure 4.2.2 Individual power spectra of finger-force velocity in response to perturbations.**

**(A)** Power spectra of the finger-force velocity of individual subjects in the no delay conditions. **(B)** The same as (A), but for the 200 ms delay conditions. Power spectra under different perturbation conditions are overlaid. Note that perturbation responses occurred on top of a baseline submovement spectrum.

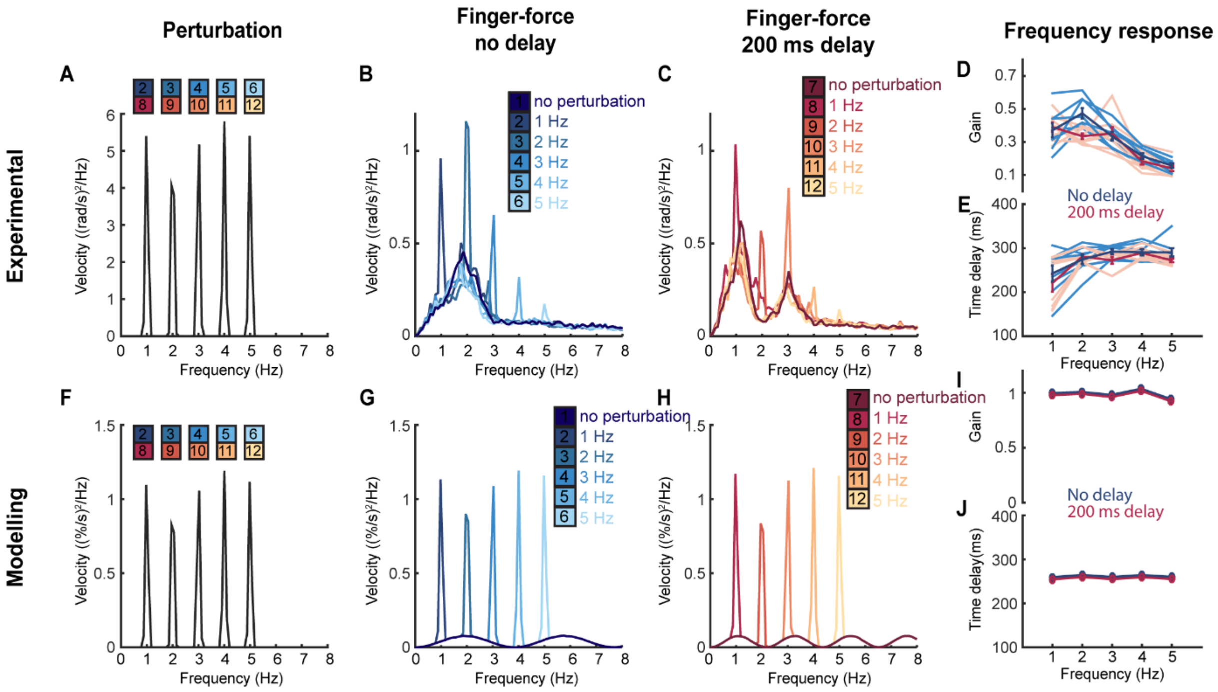

**Figure 4.2.3 Averaged finger-force response to perturbations, compared to predictions by model.**

**(A)** Perturbations of equal velocity at 1 to 5 Hz were added to the cursor. **(B)** Averaged power spectra of finger-force velocity across subjects (n=8) in the no delay conditions. **(C)** The same as (B), but for the 200 ms delay conditions. **(D)** Finger-force gain to perturbations at 1 to 5 Hz with no delay and 200 ms delay. Individual (lighter *blue* and *red*) and average (darker *blue* and *red*) finger-force gains across subjects with standard error (n=8) were plotted. **(E)** Finger-force time delay to perturbations at 1 to 5 Hz with no delay and 200 ms delay. Individual (lighter *blue* and *red*) and average (darker *blue* and *red*) finger-force time delays across subjects with standard error (n=8) were plotted. **(F-J)** As per (A-E), but for simulated data generated by the model.

The model predicted that in response to perturbations of equal velocity (Figure 4.2.3 (F)), subjects would respond equally, independent of frequency and delay (Figure 4.2.3 (G–H)). Results from human subjects actually showed that they responded unequally depending on perturbation frequency (Figure 4.2.3 (B–C)), although the response was very similar between delay conditions. Subjects' responses revealed a low-frequency envelope similar to the submovement envelope.

To quantify the amplitude response to perturbations, I calculated the gain of the finger-force velocity relative to the perturbation. The model predicted that the gain would be unity at all perturbation frequencies (Figure 4.2.3 (I)). Results from human subjects actually showed that gain (on average) was less than 0.5, and subjects responded unequally depending on perturbation frequency – with lower frequencies having higher gain than higher frequencies (Figure 4.2.3 (D)). Again, this was independent of delay.

I performed ANOVA to compare the effect of perturbation frequency and delay on finger-force gain. There was no significant effect of delay $F(1, 70) = 3.136$, $p = 0.081$. There was a significant effect of frequency $F(4, 70) = 36.338$, $p<0.0001$ and a weakly significant interaction between frequency and delay $F(4, 70) = 2.899$, $p = 0.028$.

As described in section 3.4.4, perturbations at 1–5 Hz were delivered at equal velocity, but in the power spectra, appeared to have slightly different amplitudes (e.g. Figure 4.2.3 (A, F)), because the frequency interval (0.098 Hz) at which power estimation was performed did not produce points at integer frequency values.

### 4.2.4 Analysis of finger-force time delay response

I also calculated the phase response of the finger-force velocity relative to the perturbation and converted phase into time delay (Figure 4.2.3 (E)). The model predicted that the time delay between finger-force and perturbations (Figure 4.2.3 (J)) would be equal to the visual delay ($T_v$) at all perturbation frequencies. In the human data, I actually found that the time delay increased incrementally with increases in perturbation frequency (but independent of delay condition).

I performed ANOVA to compare the effect of perturbation frequency and delay on time delay. There was no significant effect of delay $F(1, 70) = 2.625$, $p = 0.12$. There was a significant effect of frequency $F(4, 70) = 9.51$, $p<0.0001$. There was no significant interaction between frequency and delay $F(4, 70) = 0.705$, $p = 0.591$.

### 4.2.5 Summary

I measured the finger-force gain to perturbations during visuomotor tracking, to test the hypothesis that intrinsic dynamics originated from the properties of visuomotor noise. If the low-frequency submovement envelope reflected visuomotor noise, the prediction would be that the gain to perturbation of equal velocity would be level at all frequencies. Counter to this prediction, I found that the gain revealed a low-frequency response irrespective of delay resembling the submovement envelope. Furthermore, I showed an increase in time delay to perturbations with increasing perturbation frequency, irrespective of delay. These gain and time delay responses are consistent with the presence of a bandpass filter. These results suggest that intrinsic dynamics did not originate from visuomotor noise.

## 4.3 Feedforward tapping

### *4.3.1 Aim*

In the preceding section, I demonstrated that it is unlikely that intrinsic dynamics reflect properties of visuomotor noise. Moreover, I found that feedback responses to spatial perturbations exhibited low-frequency filtering resembling the submovement envelope. Such a filter could be imposed by either a feedforward pathway or a feedback pathway (see plausible sources of intrinsic dynamics in Figure 4.1.2).

The aim of the current section was therefore to investigate whether intrinsic dynamics are part of the feedforward process. For example, filtering by musculoskeletal properties (Partridge, 1965) could produce the 2–3 Hz passband seen in the submovement envelope. To investigate this experimentally, I assessed feedforward gain using a tapping task. If the low-frequency submovement envelope reflected the effects of a feedforward pathway, I would expect feedforward responses to exhibit a passband at 2–3 Hz.

### *4.3.2 Methods*

Eight participants performed an isometric unimanual tapping task (see section 2.1.2). Subjects tapped with their right index finger to an auditory cue (a beep) presented with an inter-beep frequency of [1, 2, 3, 4, and 5] Hz. Subjects received visual feedback of the cursor controlled but the target position was hidden. Instead, subjects were given an amplitude boundary of the hidden target position. Subjects were instructed to control the cursor to the full extent of the amplitude boundary. In total there were 5 conditions (Figure 4.3.1 (A)), delivered in a pseudorandom order. Finger-force responses to the target were identified as peaks in the power spectra of cursor position at target frequencies. The gain of finger-force in response to the target was calculated at each target frequency.

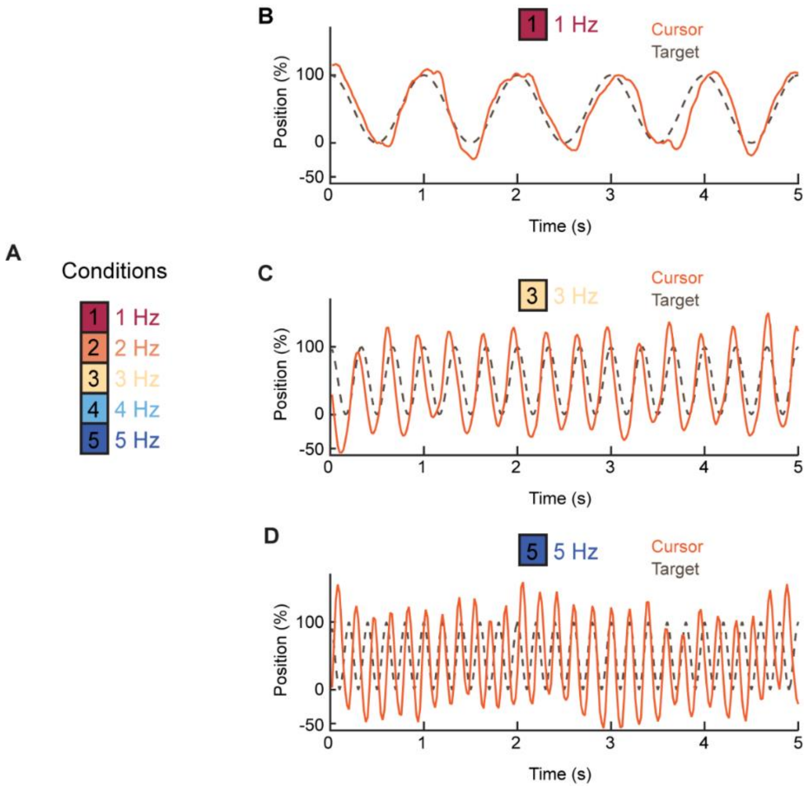

**Figure 4.3.1 Task conditions and examples data from the tapping experiment.**

**(A)** Subjects tracked a sonically-cued target, beeping at a frequency of [1, 2, 3, 4, 5] Hz given in separate conditions. Subjects received visual feedback of the cursor position, and had to tap between amplitude boundaries. **(B, C, D)** Example target and cursor position traces when a subject tapped at 1, 3 or 5 Hz, respectively.

### *4.3.3 Analysis of example, power spectra and gain response*

At higher frequencies the subject tapped with more variable amplitudes and less in-phase with the target (see representative examples in Figure 4.3.1 (B–D)).

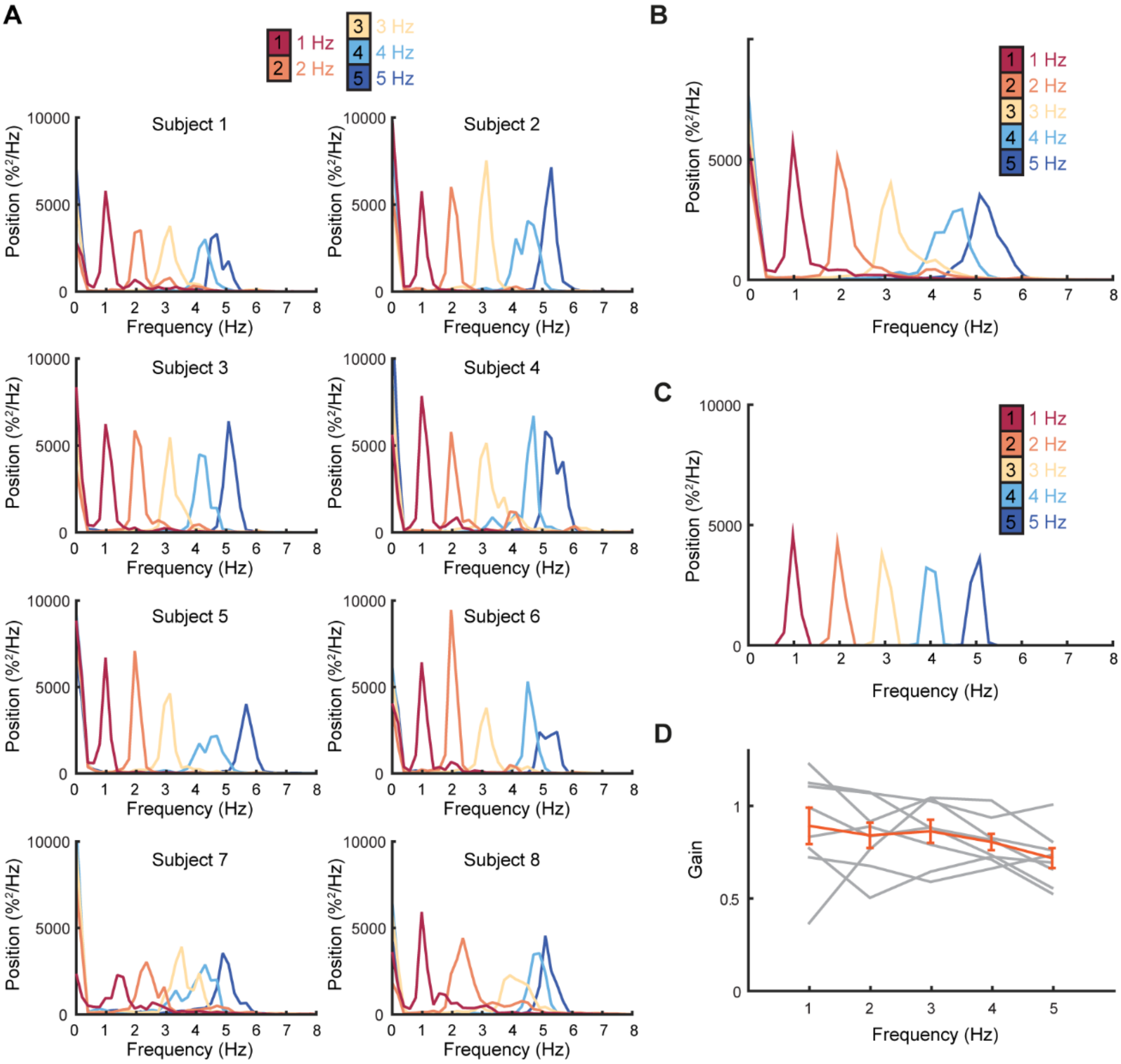

**Figure 4.3.2 Individual power spectra, averaged power spectra and gain of tapping.**

**(A)** Power spectra of finger-force position of individual subjects. Spectra of all the conditions are overlaid. **(B)** Average power spectra of finger-force position across subjects (n=8). **(C)** Power spectrum of hidden target position. **(D)** Finger-force gain to the target at 1-5 Hz; individual subjects (*grey*) and average across subjects ± standard error (*orange*).

To see more clearly how subjects tapped to targets of different frequencies, I calculated the power spectra of cursor position. If subjects tapped the full extent of the amplitude boundaries, I would expect equal power of cursor position at all frequencies, as can be seen in the true (but hidden) target position (Figure 4.3.2 (C)). As previously, the reason the peaks aren't actually of the same amplitude in this figure is an artefact of the Fourier frequencies not falling exactly at integer values (actual frequency resolution, 0.195 Hz).

Clear peaks in the cursor position power spectrum could be identified in individual spectra and in the average over subjects (Figure 4.3.2 (A–B)). In response to targets of equal position (Figure 4.3.2 (C)), subjects responded equally at all target frequencies. Most subjects could reach the target amplitude at all frequencies. Some subjects (e.g. subject 7) tapped at a slightly lower or higher frequency than the target frequency.

To quantify the amplitude response to the targets, I calculated the gain of the cursor position relative to target position (Figure 4.3.2 (D)). The average gain of all the frequencies was 0.82, 95% CI [0.69, 0.96]. I performed ANOVA to compare the effect of tapping frequency on gain. There was no significant effect of frequency $F(4, 40) = 0.174$, $p = 0.950$.

### *4.3.4 Summary*

I measured the finger-force gain of tapping to test whether intrinsic dynamics were imposed by a feedforward process. If the low-frequency submovement envelope reflected a feedforward phenomenon, I would predict that the feedforward gain profile would exhibit a passband at 2–3 Hz. Counter to this prediction, I actually found that the gain was equal at all target frequencies. Interestingly, the average feedforward gain reached 0.82, which was much higher than the finger-force gain response to perturbations during tracking (which was less than 0.5). These results suggest that intrinsic dynamics did not originate from a feedforward pathway.

## 4.4 Incorporating intrinsic dynamics in feedback controller model

### *4.4.1 Aim*

In section 4.2, I demonstrated that it is unlikely that intrinsic dynamics reflect properties of visuomotor noise. Feedback response to spatial perturbations revealed low-frequency filtering at resembling the submovement envelope. This filtering could be imposed by a feedforward or feedback processes (Figure 4.1.2). In the previous section (4.3), I provided evidence that this filtering phenomenon is not imposed by the feedforward pathway. The feedforward gain during tapping did not exhibit a low-frequency filtering; rather, it was equal at all frequencies and much higher than feedback gain to perturbations during tracking.

I therefore next speculated that intrinsic dynamics were generated as part of a *feedback* process. It is unlikely that the low-pass filtering effect we saw was a feature of sensory processing since humans can see moving object up to 60 Hz (Hecht and

Shlaer, 1936). Therefore, I speculated that filtering originated further downstream in the feedback pathway: that is in a state estimator (see Figure 4.1.2). These dynamics might be part of a state estimator which optimally estimates states by combining information from the model’s dynamics and sensory input. T he aim of this section was to improve the ‘comb filter’ model in section 3.3 by implementing intrinsic dynamics, following an optimal feedback control (OFC) theoretical framework.

### *4.4.2 Methods*

Following the optimal feedback control (OFC) theory of motor coordination (Todorov and Jordan, 2002), I incorporated intrinsic dynamics by adding a state estimator and a cost function (Figure 4.4.1(A)) to the feedback controller introduced in section 3.3.

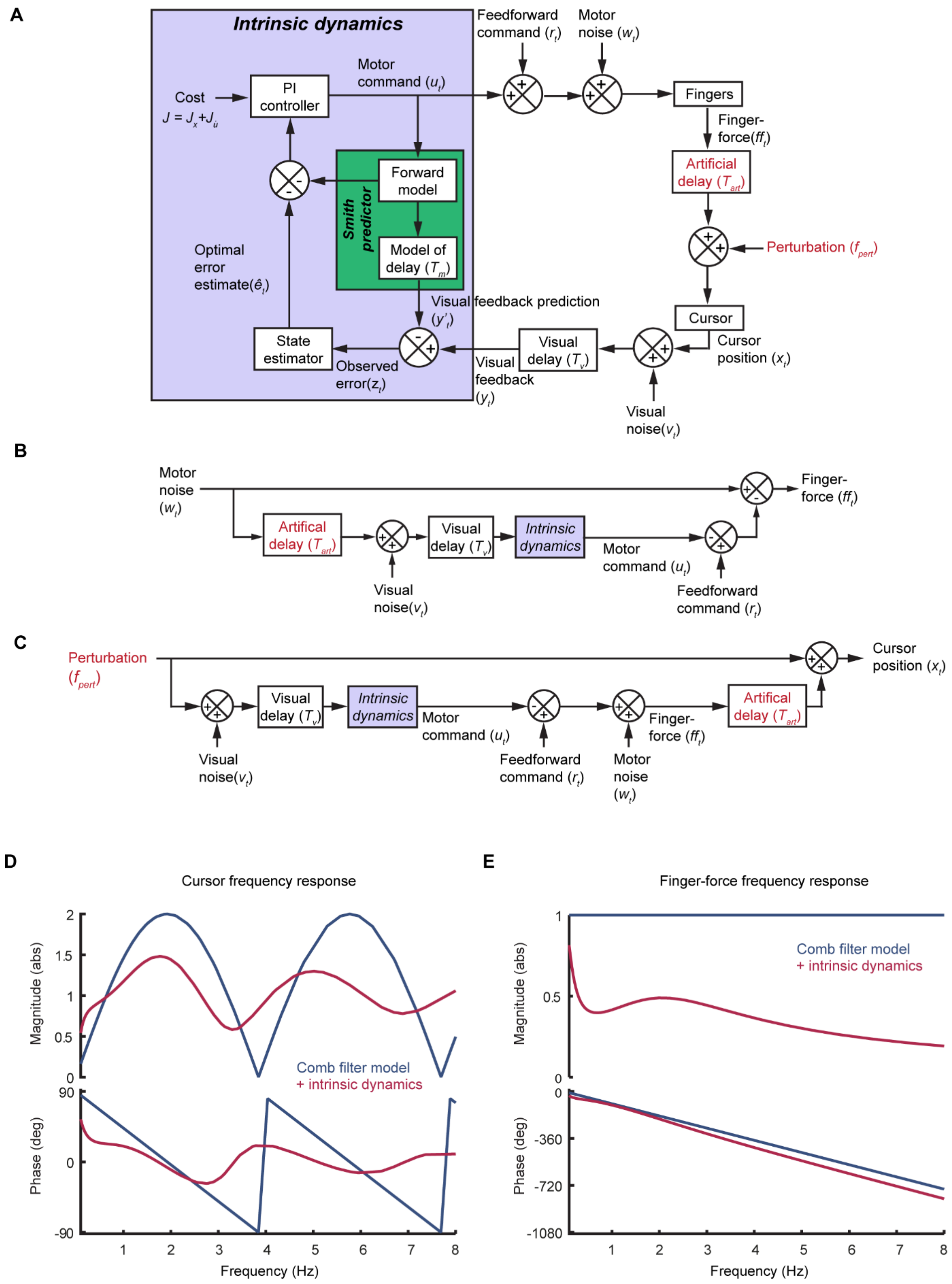

**Figure 4.4.1 Schematic and frequency response of a tracking model incorporating intrinsic dynamics.**

**(A)** Intrinsic dynamics were incorporated into the feedback controller model as part of the state estimator, PI controller, and a fast feedback loop**. (B)** Simplified schematic of feedback controller model incorporating intrinsic dynamics. **(C)** Response to perturbation of the model with intrinsic dynamics added. **(D)** The frequency response of the cursor position in response to perturbations are shown for the comb filter model (*blue*) and with intrinsic dynamics incorporated (*red*). The internal delay was set to be 260 ms. **(E)** The same as (D), but for finger-force position.

In the *comb filter* model (Figure 3.3.1 (A)), the observed error ($z_t$) was distinguished from the motor command ($u_t$) by subtracting off the visual feedback prediction ($y'_t$) from the visual feedback ($y_t$). Thus, the observed error ($z_t$) comprised the delayed motor noise ($w_{t-T}$) and visual noise ($v_{t-T}$).

According to the optimal feedback control (OFC) framework, states of interest (e.g. position, velocity) can be optimally estimated despite delayed and noisy sensory feedback. This can be done by integrating delayed noisy feedback with knowledge of dynamics of the states. Therefore, I implemented an optimal state estimator to estimate the true error ($e_t$) given a delayed and noisy observed error ($z_t$). The optimal state estimators job is to estimate the true error ($e_t$) arising from motor noise ($w_{t-T}$)*)* given the observed error ($z_t$), which is corrupted by visual noise ($v_{t-T}$*)*.

Kalman filters have been used extensively in optimal state estimation (Faragher, 2012). A Kalman filter compares uncertainty of two streams of information; specifically, it compares the uncertainty of a prediction given by an internal model to the uncertainty of sensory information. These uncertainties can be described by Gaussian distributions, and their product gives the best estimate of the state.

I implemented a Kalman filter in the *comb filter* model (Figure 4.4.1(A)). The Kalman filter was integrated with the Smith predictor in the same way as has previously been proposed (Wolpert and Miall, 1996; Schenck, 2008). The Smith predictor gives a fast prediction of the motor command, which can directly be used as a fast feedback correction (1), and a slow prediction of the motor command ($y'_t$) can be compared with visual feedback ($y_t$) (2). The fast feedback loop allowed the controller (in my model the proportional-integral controller) to have high gains (Abe and Yamanaka, 2003).

First, I will describe the state-space equations used in Kalman filters. The Kalman filter model assumes that the true state at time $t$ evolves from the prior state, at time $t-1$, according to the equation:

$$\boldsymbol{\varepsilon_t} = \boldsymbol{F}\boldsymbol{\varepsilon_{t-1}} + \boldsymbol{G}\boldsymbol{u_t} + \boldsymbol{w_t},$$

$$\boldsymbol{Cov}(\boldsymbol{w_t}) = \boldsymbol{Q_t} \qquad (4.1)$$

where $\boldsymbol{\varepsilon_t}$ is the state vector containing parameters of interest, $\boldsymbol{F}$ is the state transition matrix which applies to the prior state, $\boldsymbol{u_t}$ is the control input vector containing control inputs, $\boldsymbol{G}$ is the control input matrix which applies the effect of control parameters on to state parameters, and $\boldsymbol{w_t}$ is the vector containing process noise for each state parameter (and has covariance matrix $\boldsymbol{Q_t}$).

At time $t$ a measurement of the state $\boldsymbol{z_t}$ is made according to the equation:

$$\boldsymbol{z_t} = \boldsymbol{H\varepsilon_t} + \boldsymbol{v_t}$$

$$\boldsymbol{Cov}(\boldsymbol{v_t}) = \boldsymbol{R_t} \tag{4.2}$$

where $\boldsymbol{H}$ is the transformation matrix which maps the true state space into the measurement space, and $\boldsymbol{v_t}$ is the vector containing measurement noise for each measurement parameter (and has covariance matrix $\boldsymbol{R}_t$).

Next, I will describe how I implemented the Kalman filter in my model. Consider the 1D tracking problem to estimate the true error. The position and velocity of error are described by the state vector:

$$\boldsymbol{\varepsilon_t} = \begin{bmatrix} e_t \\ \dot{e}_t \end{bmatrix} \tag{4.3}$$

where $e_t$ is error position and $\dot{e}_t$ is error velocity.

My Kalman filter model assumes that the true state at time $t$ evolved from the prior state at time $t-1$ according to the equation:

$$\boldsymbol{\varepsilon_t} = \boldsymbol{F\varepsilon_{t-1}} + \boldsymbol{D}a_t$$

$$\boldsymbol{Cov}(\boldsymbol{Da_t}) = \boldsymbol{Q_t} \tag{4.4}$$

where $\boldsymbol{D}$ is a matrix which applies the effect of $a_t$ to the state parameters, and $a_t$ is acceleration. Since no control inputs contribute to the true error**,** there is no $\boldsymbol{Gu_t}$ term in the state equation. Moreover, I assume the process noise, $\boldsymbol{w_t}$, arises from uncontrolled forces which cause accelerations $a_t$ (and that these are normally distributed, with mean 0 and standard deviation $\sigma_a$).

The result of an acceleration during the time period $\Delta t$ (the time between $t$ and $t-1$) and the position and velocity of the error is given by the following equations:

$$e_t = e_{t-1} + (\dot{e}_t \times \Delta t) + (a_t \times \frac{1}{2}\Delta t^2) \tag{4.5}$$

$$\dot{e}_t = \dot{e}_{t-1} + (a_t \times \Delta t) \tag{4.6}$$

Which can be written in matrix form as:

$$\begin{bmatrix} e_t \\ \dot{e}_t \end{bmatrix} = \begin{bmatrix} 1 & \Delta t \\ 0 & 1 \end{bmatrix} \begin{bmatrix} e_{t-1} \\ \dot{e}_{t-1} \end{bmatrix} + \begin{bmatrix} \frac{1}{2}\Delta t^2 \\ \Delta t \end{bmatrix} a_t \tag{4.7}$$

This gives us matrices $\boldsymbol{F}$ and $\boldsymbol{D}$ in equation (4.4):

$$\boldsymbol{F} = \begin{bmatrix} 1 & \Delta t \\ 0 & 1 \end{bmatrix} \tag{4.8}$$

$$\boldsymbol{D} = \begin{bmatrix} \frac{1}{2}\Delta t^2 \\ \Delta t \end{bmatrix} \tag{4.9}$$

The covariance matrix $\boldsymbol{Q}$ is:

$$\boldsymbol{Q} = \boldsymbol{D}\boldsymbol{D}^{\boldsymbol{T}}\, {\sigma_a}^2 = \begin{bmatrix} \frac{1}{4}\Delta t^4 & \frac{1}{2}\Delta t^3 \\ \frac{1}{2}\Delta t^3 & \Delta t^2 \end{bmatrix} {\sigma_a}^2 \tag{4.10}$$

My Kalman filter model makes a measurement of the state $\boldsymbol{z_t}$ at time $t$ according to equation 4.2. The model can only observe the position of the state (error position, $e_t$), giving $\boldsymbol{H} = [1 \quad 0]$. The measurement noise $\boldsymbol{v_t}$ is assumed to be normally distributed, with mean 0 and standard deviation $\sigma_v$.

The steady-state Kalman filter was solved for using the function *kalman* in MATLAB, based on the model's state equation and measurement equation. The innovation gain ($\boldsymbol{M}$) (i.e. the discrepancy between the measured and predicted values of $\boldsymbol{z_t}$), was chosen to minimize the steady-state covariance of the estimation error given the noise covariance $\boldsymbol{Q}$ and $\boldsymbol{R}$. This gives the Kalman filter:

$$\dot{\hat{\boldsymbol{\varepsilon}}} = \boldsymbol{A}\, \hat{\boldsymbol{\varepsilon}} + \boldsymbol{B}\boldsymbol{z} \tag{4.11}$$

where $\boldsymbol{A} = (\boldsymbol{F} - \boldsymbol{MCF} - \boldsymbol{I})/\Delta t$ , $\boldsymbol{B} = \boldsymbol{FM}/\Delta t$, $\hat{\boldsymbol{\varepsilon}}$ is the optimally estimated state, and $\boldsymbol{z}$ is the observed error. Note that the only free variable in my Kalman filter model is the ratio between noise covariance $\boldsymbol{Q}$ and $\boldsymbol{R}$ which determines the resonance frequency of the filter. I chose this ratio to match the resonance frequency with the submovement envelope observed in the experimental data.

Note that state estimation was performed on the delayed error, $\boldsymbol{z}_{t-T_v}$. Therefore, the current optimally estimated error position, $\widehat{e_t}$, could be predicted using knowledge of the velocity:

$$\widehat{e_t} = \widehat{e_t} + \left(\widehat{\dot{e}_t} \times T_v\right)$$

(4.12)

where $T_v$ is the visual delay, assumed to be 0.260 s.

Thus, the current optimally estimated error position is:

$$\widehat{e_t} = \boldsymbol{C}\hat{\boldsymbol{\varepsilon}}$$

(4.13)

where $\boldsymbol{C} = [1 \quad T_v]$.

Next, I will describe the implementation of the proportional-integral (PI) controller. Gains of the controller were derived from a cost function designed to minimize position and change in control (velocity). I decided to choose to minimize the change in control rather than the control, based on the fact that the noise observed in subjects' data was proportional to change in control. In this case, position and velocity of the error is given by the following equations:

$$e_t = e_{t-1} + (\dot{e}_t \times \Delta t)$$

(4.14)

$$\dot{e}_t = \dot{e}_{t-1} + (\dot{u}_t \times \Delta t)$$

(4.15)

In state space:

$$\boldsymbol{\varepsilon_t} = \boldsymbol{F}\boldsymbol{\varepsilon_{t-1}} + \boldsymbol{G}\boldsymbol{u_t}$$

(4.16)

where $\boldsymbol{G} = \begin{bmatrix} 0 \\ 1 \end{bmatrix}$ and $\boldsymbol{u_t} = \begin{bmatrix} u_t \\ \dot{u}_t \end{bmatrix}$.

The state feedback law $\dot{\boldsymbol{u}}_{\boldsymbol{t}} = -\boldsymbol{K}\boldsymbol{\varepsilon_t}$ minimized the quadratic cost function:

$$\boldsymbol{J} = \sum_{t=0}^{\infty}\{\boldsymbol{\varepsilon_t}^{\boldsymbol{T}}\boldsymbol{Q}\boldsymbol{\varepsilon_t}+\dot{\boldsymbol{u}}_{\boldsymbol{t}}^{\boldsymbol{T}}\boldsymbol{R}\dot{\boldsymbol{u}}_{\boldsymbol{t}}\} \tag{4.17}$$

where $\boldsymbol{Q}$ and $\boldsymbol{R}$ are weighting matrices that apply to position and change in control, respectively. I weighted position and change in control equally.

The proportional-integral gains ($K_p$ and $K_i$) were solved using the linear-quadratic regulator (LQR) function, *lqr*, in MATLAB and derived from the state feedback law by integrating both sides of the equation:

The proportional-integral gains ($K_p$ and $K_i$) were solved using the function *lqr* in MATLAB and derived from the state feedback law by integrating both sides of the equation:

$$\int_{t=0}^{T} \dot{\boldsymbol{u}}_{\boldsymbol{t}}\,dt = \int_{t=0}^{T} -\boldsymbol{K}\boldsymbol{\varepsilon_t} \tag{4.18}$$

$$u_t = -\boldsymbol{K}\int_{t=0}^{T}\begin{bmatrix} e_t \\ \dot{e}_t \end{bmatrix} dt = -\boldsymbol{K}\begin{bmatrix} \int_{\boldsymbol{t=0}}^{\boldsymbol{T}} e_t dt \\ e_t \end{bmatrix} = -K_i\int_{\boldsymbol{t=0}}^{\boldsymbol{T}} e_t dt - K_p\, e_t \tag{4.19}$$

Finally, I repeated the simulation of the effect of delay and perturbation using this new model, and compared the simulated data with experimental results and with simulated data from the old feedback controller model. I labelled the old model the *comb filter* model and the new one the *+intrinsic dynamics* model.

### *4.4.3 Cursor and finger-force frequency response*

The cursor frequency response to spatial perturbations can be seen in Figure 4.4.1(D). The cursor magnitude response consisted of alternating peaks and troughs in both models, with the addition of a low-frequency bandpass filter in the *+intrinsic dynamics* model. In the *comb filter* model submovements occurred at around 2 and 6 Hz, whereas in the *+intrinsic dynamics* model the second peak shifted to a lower frequency, of around 5 Hz. In the *comb filter* model, the maximum gain response reached 2, whereas in the *+intrinsic* model the maximum gain response was reduced to around 1.4.

The finger-force frequency response to perturbation can be seen in Figure 4.4.1(E). The *comb filter* model had a gain of 1 at all frequencies. The *+intrinsic* *dynamics* model had a low-frequency bandpass filter gain with a peak at around 2 Hz. Moreover, an additional phase shift was introduced in the *+intrinsic dynamics* model.

### ***4.4.4 Simulation of the effect of delay on submovement frequencies***

I generated simulated tracking data based on the *+intrinsic dynamics* model can be seen, but with no delay and with 400 ms added delay (Figure 4.4.2 (A, B)). Performance declined with increase in delay (Figure 4.4.2 (C)) consistent with experimental performance ($r^2 = 0.96$, $F(1, 3) = 77.18$, $p < 0.0001$). The power spectra of velocity in the simulated data from this model revealed delay-dependent alternating-peaks and troughs replicating, submovement spectra. Moreover, the envelope of the power spectrum across different delay conditions exhibited a bandpass filter-like shape, matching the experimental submovement spectrum.

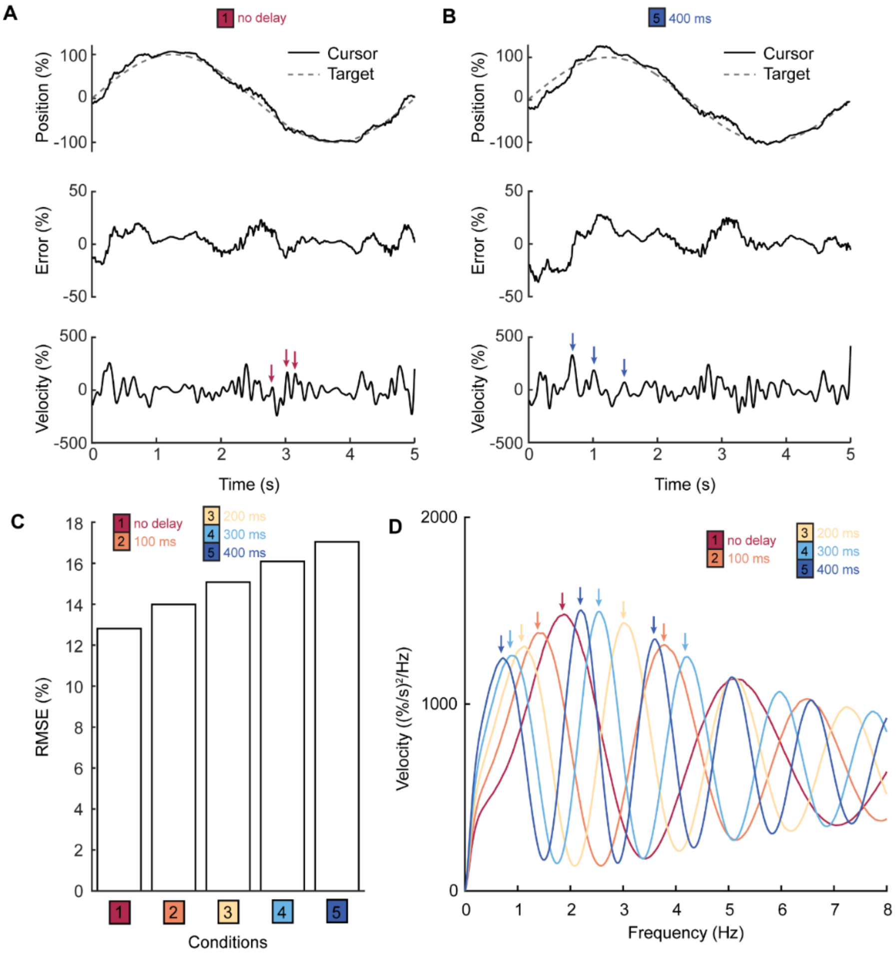

**Figure 4.4.2 Simulation of the *+intrinsic dynamics* model and the effect of delay on submovement frequencies.**

**(A)** Example traces of position and velocity in the no delay condition. To better visualise submovements, I subtracted the target position from the cursor position. Velocity was low-pass filtered and three examples of submovements are indicated by arrows. **(B)** The same as (A), but for the 400 ms delay condition. **(C)** Performance across delay conditions is shown as RMSE. **(D)** Smoothed power spectra of cursor velocity of different delay conditions, overlaid. Arrows indicate submovement frequency peaks.

Next, I investigated how well submovement frequencies were predicted by the *comb filter* model compared to the *+intrinsic dynamics* model. Submovement frequencies were better predicted by the *+intrinsic dynamics* model than by the *comb filter* model (Figure 4.4.3 (A)). The slope of the fitted line between experimental submovement frequencies and the one predicted by the *comb filter* model was 1.11 95% CI [1.04, 1.17], whereas the one predicted by the *+intrinsic dynamics* model was 1.00 95% CI [0.96, 1.05].

Finally, according to the *comb filter* model, submovement frequencies can be determined if the total time delay ($T,$ the sum of visual delay ($T_v$) and artificial delay ($T_{art}$)) in the feedback loop is known (see Figure 3.3.1). Power spectra of cursor velocity revealed submovement frequencies shifting with artificial delays. Therefore, the internal visual delay can be calculated if the frequency of submovements and the artificial delay are known (Figure 4.4.3 (B)).

The amplitude response of the feedback controller model predicted submovement frequencies to occur at $f_{1st} = {}^{1}/_{2}\, T_{v+art},\ f_{3rd} = {}^{3}/_{2}\, T_{v+art}$, and $f_{5th} = {}^{5}/_{2}\, T_{v+art}$. The internal time delay for submovements of 1st, 3th, and 5th harmonics were calculated as follows: $T_{v(1st)} = 2f_{1st} - T_{art},\ T_{v(3rd)} = {}^{2}/_{3}\, f_{3rd} - T_{art}$, and $T_{v(5th)} = {}^{2}/_{5}\, f_{5th} - T_{art}$. Next, I plotted the internal time delay against submovement frequency for each submovement peak. This revealed an increase in time delay with increase in submovement frequency, matching the increase in time delay with increase in perturbation frequency. The increase in time delay with increase in submovement frequency was predicted by the *+intrinsic dynamics* model but not by the *comb filter* model (in which the time delay was constant, at 260 ms, for all submovement frequencies).

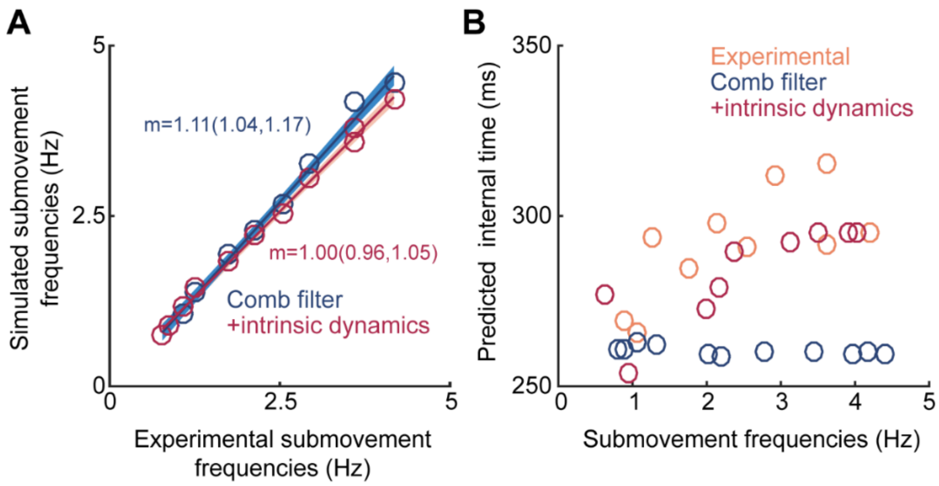

**Figure 4.4.3 Comparison between comb filter and +intrinsic dynamics model in predicting submovement frequencies and internal time delay.**

**(A)** Simulated submovement frequencies were regressed against the average of experimental submovement frequencies across subjects (n=8). **(B)** The internal time delay was predicted from the average of experimental submovement frequencies across subjects (*orange*) and from simulated submovement frequencies for both the *comb filter* model (blue) and the *+intrinsic dynamics* model (*red*).

### *4.4.5 Simulation of the effect of perturbations on cursor frequency response and finger-force amplitude response*

Next, I performed a simulation of the effect of spatial perturbations in the *+intrinsic dynamics* model. Examples of tracking with the addition of perturbations at 2 and 3 Hz can be seen in Figure 4.4.4(A-B). Similar to simulations in the *comb filter* model (Figure 3.4.3 (C-D)), the 2 Hz perturbation trace consisted of more fluctuations than the 3 Hz perturbation trace. A clear in-phase relationship was seen between cursor (*black*) and finger-force velocity (*red*) when 2 Hz perturbation was added. In comparison, a clear out-of-phase relationship was seen between cursor (*black*) and finger-force velocity (*red*) when 3 Hz perturbation was added. These examples matched the experimental examples. Performance across conditions was well predicted by the *+intrinsic dynamics* model ($r^2 = 0.95$, $F(1, 10) = 199.51$, $p < 0.0001$) (Figure 4.4.4(C)).

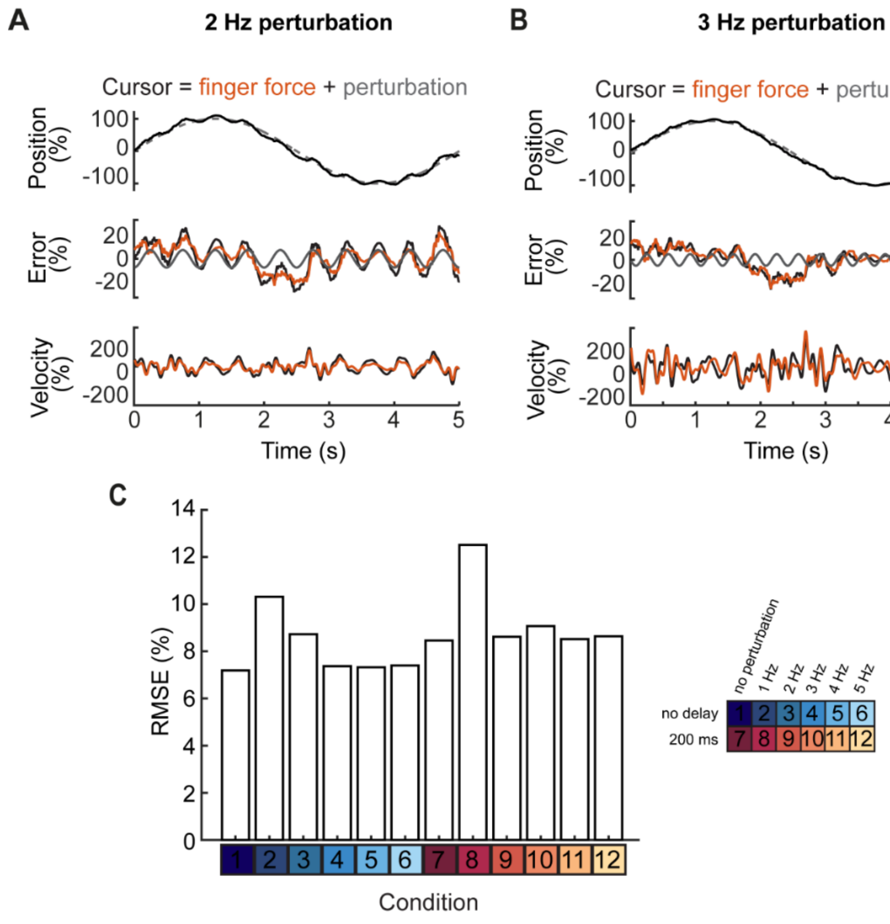

**Figure 4.4.4 Examples and performance of the +*intrinsic dynamics* model in simulation of the perturbation delay experiment.**

**(A)** Example simulated position and velocity traces under the 2 Hz perturbation condition. To better visualise submovements, I subtracted the target position from the cursor position. The low-pass filtered velocity is shown. **(B)** The same as (A), but under 3 Hz perturbation condition. **(C)** Performance is shown as RMSE.

Cursor response to perturbations of equal velocity (Figure 4.4.5 (A)) revealed a comb filter response shifting with delay, similar to the experimental cursor response (Figure 4.4.5 (B-C)). Gain was highest at submovement frequencies with gain values matching experimental cursor gain responses (Figure 4.4.5 (D)). Finger-force response to perturbations of equal velocity (Figure 4.4.5 (E)) revealed bandpass filtering (Figure 4.4.5 (F–G)). The finger-force gain revealed a band-pass filter peaking at 2 Hz and an increase in time delay with increase in perturbation frequency, matching the experimental frequency response.

Cursor response to perturbations of equal velocity (Figure 4.4.5 (A)) revealed a comb filter response shifting with delay similar to the experimental cursor response (Figure 4.4.5 (B-C)). Gain was highest at submovement frequencies with gain values matching experimental cursor gain responses (Figure 4.4.5 (D)). Finger-force

response to perturbations of equal velocity (Figure 4.4.5 (E)) revealed bandpass filtering (Figure 4.4.5 (F-G)). The finger-force gain revealed a band-pass filter peaking at 2 Hz and an increase in time delay with increase in perturbation frequency, matching the experimental frequency response.

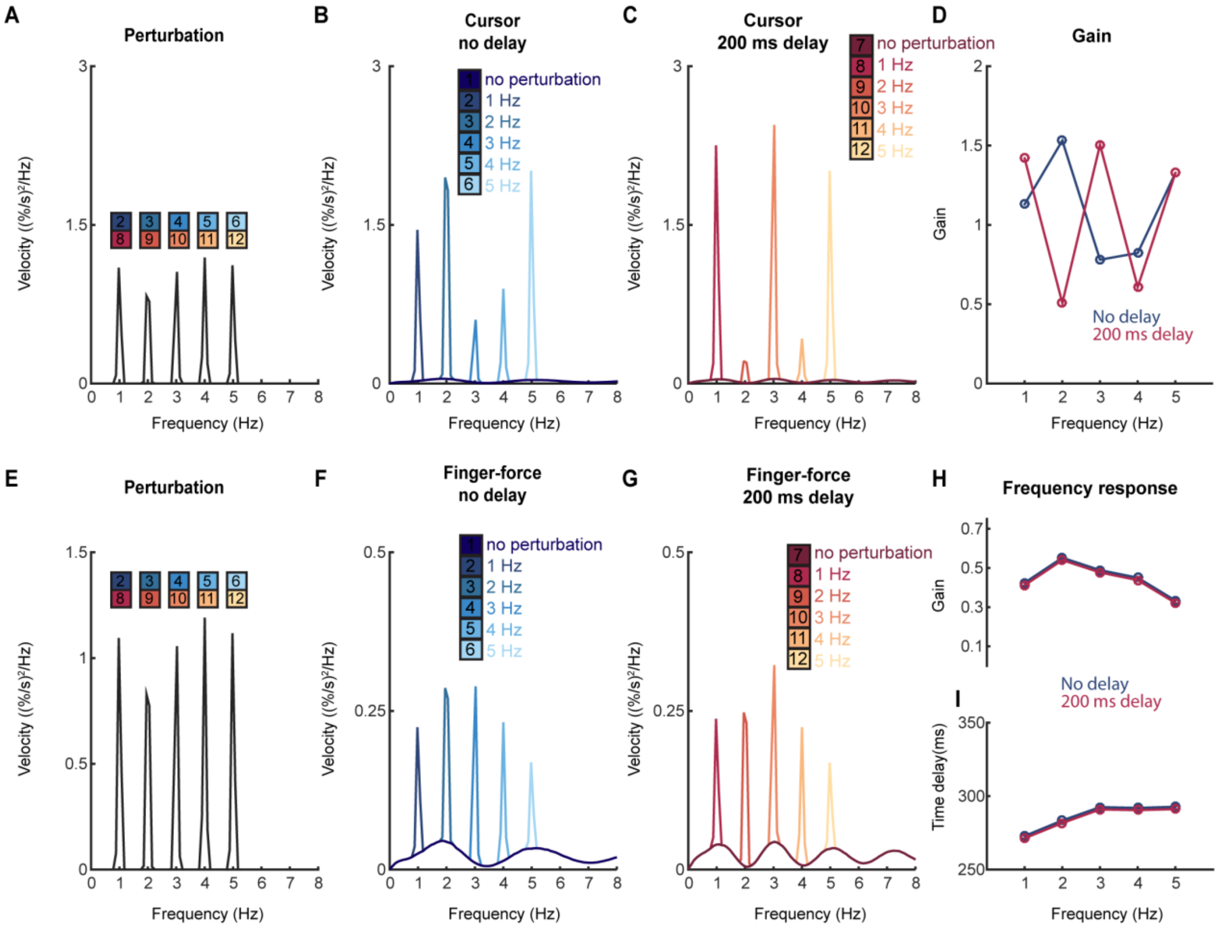

**Figure 4.4.5 Simulation of the effect of perturbations in the *+intrinsic dynamics* model.**

**(A)** Perturbations of equal velocity at 1 to 5 Hz were added to the cursor. **(B)** Simulated power spectra of cursor velocity in the no delay conditions. **(C)** The same as (B), but for the 200 ms delay condition. **(D)** Cursor gain to perturbations at 1 to 5 Hz with no delay (*blue*) and 200 ms delay (*red*). **(E)** The same as (A). **(F-H)** The same as (B-D), but for finger-force. **(I)** Finger-force time delay to perturbations at 1 to 5 Hz with no delay (*blue*) and 200 ms delay (*red*).

### *4.4.6 Summary*

I incorporated intrinsic dynamics into a feedback controller model. The *+intrinsic dynamics* model was able to explain features in the experimental data better than the *comb filter* model. The *+intrinsic dynamics* model reproduced the low frequency bandpass filter shape seen in the power spectra of submovement frequencies, and in the cursor and finger-force responses to perturbations. The finger-force gain response reproduced the intrinsic low-frequency bandpass filter shape, with a central frequency of 2 Hz, irrespective of delay. The increase in time delay with increase in perturbation frequency suggested the presence of a filter. Finally, submovement frequencies were better predicted by the *+intrinsic dynamics* model than the *comb filter* model.

## 4.5 Discussion

In this chapter, I investigated the origin of the low-frequency bandpass envelope (intrinsic dynamics) in the power spectra of submovement frequencies. I investigated whether intrinsic dynamics reflected properties of visuomotor noise, the feedforward pathway, or the feedback pathway.

### *4.5.1 Intrinsic dynamics did not reflect properties of visuomotor noise*

First, I tested the hypothesis that intrinsic dynamics reflected properties of visuomotor noise. The comb filter model predicted that the finger-force would be a negatively delayed version of the perturbation (Figure 4.4.1 (B)). However, in response to spatial perturbations of equal velocity at different frequencies, subjects responded unequally depending on the frequency. The finger-force frequency response to perturbations revealed a low-frequency band-pass filter with a central frequency of 2 Hz. Moreover, this frequency response was independent of delay, and resembled the overall submovement envelope.

I was unable to directly measure the properties of visuomotor noise from this experiment and it is possible that sinusoidal perturbations and visuomotor noise could be processed differently by visual feedback control. However, were this to be the case, it would be a surprising coincidence that the feedback response to sinusoidal perturbations resembled so closely the submovement envelope if the latter reflected properties of the visuomotor noise. A more parsimonious explanation is that the envelope of the submovement peaks and the low-pass filtering of feedback corrections reflect the same underlying phenomenon.

### *4.5.2 Feedforward process did not impose intrinsic dynamics*

Next, I tested the hypothesis that intrinsic dynamics originated from the feedforward process of movement. In response to auditory cues beeping at different frequencies, subjects responded with equal amplitude, independent of frequency. This suggest that a feedforward process did not impose intrinsic dynamics. However, this result does not show that no filtering occurred in the feedforward process. Filtering (e.g. by muscles) could occur but the feedforward processes were able to overcome it. Loram *et al.* (2006) showed that the mean of maximum frequency of joystick oscillations by humans was 6 Hz. Their finding is consistent with the idea that the feedforward process could overcome a low-frequency bandpass filter at 2–3 Hz. Indeed, I found that the feedforward gain reached 0.8 at all frequencies, which was much higher than the feedback response to perturbations, which only reached 0.5 at 2–3 Hz.

### *4.5.3 Intrinsic dynamics were modelled to originate in the feedback process: specifically the state estimator*

Having found that intrinsic dynamics originated neither from the properties of visuomotor noise, nor from a feedforward process, I concluded that intrinsic dynamics originated from feedback processes. Since humans can perceive motion higher than 5 Hz (Hecht and Shlaer, 1936), intrinsic dynamics seemed unlikely to be a limitation caused by visual processing. Therefore, I speculated that it originated from the state estimator.

Using the framework of optimal control theory, I implemented a state estimator and a cost function to the *comb filter* model. The *+intrinsic dynamics* model improved the *comb filter* model and reproduced experimental features that were not reproduced by the *comb filter* model: the low-frequency submovement envelope, the lower gain of cursor amplitude response to perturbation, and the 2–3 Hz bandpass filter of finger-force frequency response to perturbation. Moreover, the *+intrinsic dynamics* model predicted submovement frequencies better than the *comb filter* model.

How does the *+intrinsic dynamics* model explain these experimental features? The bandpass filter at 2–3 Hz, found in the feedback responses, was introduced by the optimal state estimator. The optimal state estimator had to distinguish the true state of the world in the presence of uncertain measurement by combining sensory information with an internal model of the dynamics of the external world. Forces acted in the world were assumed to obey Newtonian physics. Therefore I assumed that the motor output was corrupted by random accelerations (i.e. motor noise). On the other hand, sampling of visual feedback of position was assumed to be corrupted with instantaneous uncorrelated random noise (i.e. visual noise). The steady-state innovation gain used for optimal state estimation was only dependent on the ratio of the process noise ($\boldsymbol{Q}$) and measurement noise ($\boldsymbol{R}$), that is (in this case) the ratio between motor and visual noise. This ratio determines the resonance frequency of the Kalman filter. This bandpass like effect of the Kalman filter has previously been described (Wang, 1999).

### *4.5.4 Attenuation of feedback gains in isometric visuomotor tracking*

Another surprising result was that the feedback response gain was generally low: below 0.5 at all frequencies. This low gain to sinusoidal perturbations was also reported by Hudson and Landy (2016), in particular when perturbations were added in directions other than the direction of movement. They showed that when perturbations were added in the direction of movement, the gain was high (up to 0.8). It could be the case that perturbations added in directions other than the direction of movement are less relevant to the task than the ones added in the direction of movement. This view is consistent with the 'uncontrolled manifold' hypothesis (Latash *et al.*, 2002), in which there is selective stabilization of a task relevant dimension.

In my experimental data, the gain was low, despite sinusoidal perturbations being added in the circular direction of the movement. One aspect of my task design that may explain these low gains is that I used an isometric task. It is possible that (perturbed) visual feedback was in conflict with (unperturbed) proprioceptive information about the forces applied by the fingers. Hence corrective responses may have reflected an attenuated estimate of the perturbation as a result of cross-modal sensory integration. However preliminary experiments that I performed suggested that corrective gains were low even when perturbations were added to the target position instead of the cursor (i.e. a situation where there is no conflict between visual and proprioceptive feedback).

An alternative explanation, which we applied in the model, was to assume that subjects sought to minimize the fluctuations in control signals. In this interpretation, the low gains (e.g. < 0.5) were introduced by the proportional-integral (PI) controller, because an optimal policy attempts to offset the cost of positional errors against the cost of fast-fluctuating control signals. The PI controller gains were derived from a cost function minimizing position and change in control (velocity). I chose to minimize change in control (instead of control signals themselves) based on preliminary observations (not shown) that the trial-to-trial trajectory variability through the target cycle reflected cursor speed rather than cursor position. This suggested that minimizing speed fluctuations would be a good strategy to minimize tracking variability. Kleinman (1974) included the same cost function in his model and argued that it could account for the physiological limitations on the rate at which a human can effect control. Moreover, the frequency response of human position control is characteristic of integration (Jagacinski and Flach, 2003).

Of course, it is important to say that I have no direct experimental proof that PI control is responsible for the experimental results, and further experiments would be required to examine the role of (unperturbed) proprioceptive feedback in reducing these gains. However, many behavioral experiments suggest that the brain performs optimal state estimation and that motor commands are optimized with respect to some cost function (Todorov and Jordan, 2002; Scott, 2004; Diedrichsen et al., 2010).

## 4.6 Chapter summary

- I investigated whether intrinsic dynamics originated from properties of visuomotor noise, the feedforward pathway or the feedback pathway.
- I found that intrinsic dynamics did not reflect visuomotor noise, the feedforward pathway or visual processing limitation and speculated that they originate as part of a state estimator.
- In the framework of optimal control theory, I implemented a state estimator and a cost function to the feedback controller model.
- The addition of intrinsic dynamics to the feedback controller model explained many features seen in the experimental results that were not explained by a simpler model.

# Chapter 5. Extrinsic and intrinsic dynamics in local field potentials recorded from non-human primates

## 5.1 Chapter overview

In the preceding chapters, I have shown that submovement frequencies depend systematically on visual feedback delay. However, I have also identified a low-frequency bandpass filter phenomenon, which persists irrespective of external delay. I have demonstrated that this low-frequency bandpass filter reflects intrinsic dynamics in the feedback loop, and speculated that this may be based on a steady-state Kalman Filter state estimator. Such a steady-state Kalman filter is a 2nd order filter, which can be described as a 2nd order dynamical system.

In its most simplified form (under extremely simplified linear assumptions), such a dynamical system could be implemented in the brain by a recurrent neural network of only two neuronal populations, representing an estimate of position and velocity respectively (Figure 5.1.1). I looked for evidence of such a network in local field potential (LFP) recordings from the motor cortex of monkeys performing a visuomotor centre-out task.

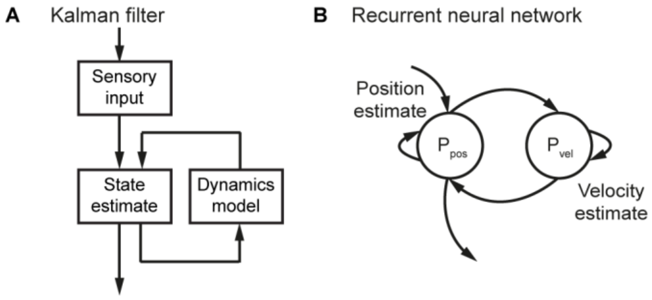

**Figure 5.1.1 Neuronal implementation of the state estimator.**

**(A)** A Kalman filter combines sensor input and knowledge about the state dynamics to estimate the state optimally. **(B)** A steady-state Kalman filter could be implemented in the brain by a recurrent neuronal network comprising two neuronal populations, representing position and velocity respectively.

In this chapter, I will investigate the effect of visual feedback delay on behaviour and LFP oscillations. I will show that, similar to humans, submovement frequencies in monkeys shift with delay. I will describe both delay-dependent and delay-independent features in the LFP. These features bear a remarkable similarity to simulations based on the model of feedback control incorporating intrinsic dynamics (+*intrinsic dynamics* model).

### 5.2 Aim

The aim of this section was to test the effect of artificially increasing visual feedback delays on behaviour and LFPs recorded in monkeys.

### 5.3 Methods

Two monkeys (*Macaca mulatta*) performed an isometric 2D centre-out task (section 2.2.1). Visual feedback of the cursor was delayed by [0, 200, 400 and 600] ms, delivered in separate condition blocks (Figure 5.4.1 (B)).

I differentiated the magnitude of the 2D torque (expressed as a percentage of the distance to the edge of the screen) to obtain radial cursor velocity (expressed as %/s). When performing frequency analysis, I removed the task-locked component by subtracting the average velocity across trials, to better visualise submovements. Submovement frequencies were identified as peaks in the smoothed power spectrum of the velocity. LFP channels were visually inspected to reject noisy LFP channels. I removed the task-locked LFP components by subtracting the average LFPs across trials. Coherence spectra were calculated between radial cursor velocity and LFP.

Submovements were defined as a peak cursor speed exceeding 100 %/s in monkey S and 150 %/s in monkey U. Dimensionality reduction was performed on LFPs using principal component analysis and its projections will be referred throughout as LFP-PCs. Submovement-triggered averages were compiled from low-pass filtered (10 Hz, four-pole, zero-phase digital Butterworth filter) cursor speed, band-pass filtered (0.5–10 Hz, four-pole, zero-phase digital Butterworth filter) surface-referenced M1 LFPs, and LFP-PCs. Imaginary cross-spectral density was calculated between unfiltered surface-referenced M1 LFPs.

Simulations were performed based on the +*intrinsic dynamics* model introduced in section 4.4. The LFPs were simulated crudely as the net synaptic inputs onto two neural populations in a simple recurrent neural network model of the state estimator based on equation (4.12):

$$\dot{\hat{\boldsymbol{\varepsilon}}} = \boldsymbol{A}\,\hat{\boldsymbol{\varepsilon}} + \boldsymbol{Bz}$$

(5.1)

where $= (\boldsymbol{F} - \boldsymbol{MCF} - \boldsymbol{I})/\Delta t$ , $\boldsymbol{B} = \boldsymbol{FM}/\Delta t$, $\hat{\boldsymbol{\varepsilon}}$ is the optimally estimated state, and $\boldsymbol{z}$ is the observed error.

Simplistically, we can imagine that position and velocity are represented by two neural populations with mean activity $P_{pos}$ and $P_{vel}$ evolving according to the following state equation:

$$\frac{d}{dt}\begin{bmatrix} P_{pos} \\ P_{vel} \end{bmatrix} = \boldsymbol{A}\begin{bmatrix} P_{pos} \\ P_{vel} \end{bmatrix} + \boldsymbol{B}z_t$$

(5.2)

where the matrix $\boldsymbol{A}$ can now be thought of as representing the synaptic connectivity matrix for the network. The net synaptic input onto each neural population is given by $\frac{dP_{pos}}{dt}$ and $\frac{dP_{vel}}{dt}$. We assume that each neural population has a different spatial localization within the cortex, and therefore model the LFPs as different super-positions of these two components reflecting the net synaptic potentials on these populations.

### 5.4 Analysis of power spectra and coherence of speed and LFP

Submovements were seen as fluctuations in the radial cursor speed (e.g. Figure 5.4.1 (D)), and peaks in individual power spectra of cursor speed for each monkey (Figure 5.4.2(A) and Figure 5.4.3(A)). With no delay added, submovements occurred at around 2 Hz. A smaller harmonic around 5 Hz was also seen in monkey U. These peaks shifted to lower frequencies as delay was added, agreeing with model predictions (Figure 5.4.4 (A)). A third harmonic appeared with a delay of 400 ms, and a fourth when a delay of 600 ms was added. Note that, as with the human data, the higher harmonic peaks had a smaller amplitude, but their amplitude increased as their frequency decreased with longer delays.

Examples of fluctuations in the LFPs locked to submovements were seen when no delay and 200 ms delay was added (Figure 5.4.1 (E)). Different phases of LFP in relation to the submovements were seen, as summarised by the LFP-PCs (Figure 5.4.1 (F)). The LFP-PC exhibited a striking correlation with submovements (Figure 5.4.1 (G)).

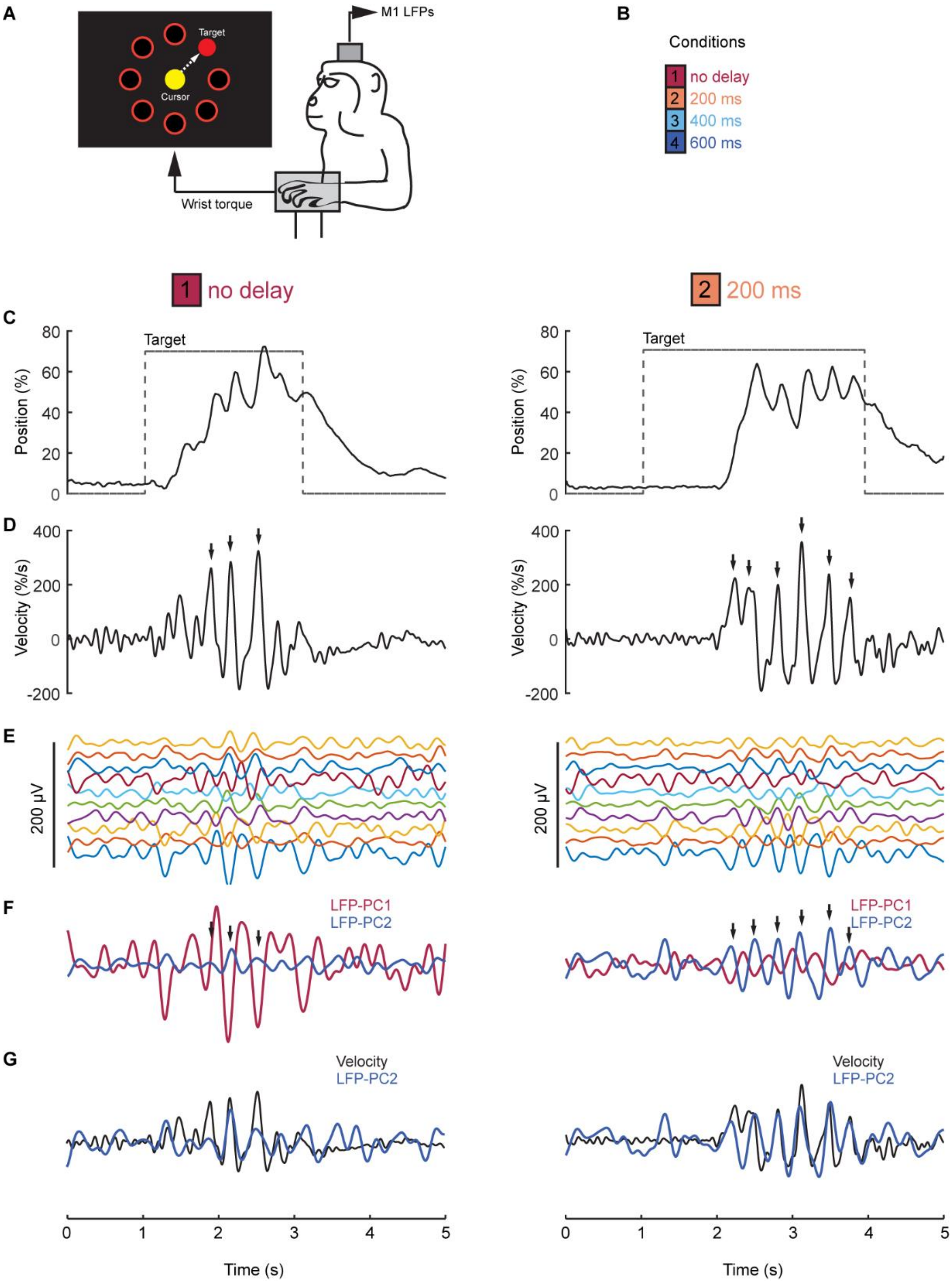

**Figure 5.4.1 Task design and examples of LFP experiment.**

**(A)** Two monkeys performed a wrist torque-controlled centre-out task. **(B)** Delays of 0, 200, 400 and 600 ms were added to the visual feedback of the cursor in separate conditions. **(C)** Examples of cursor position of a typical trial are shown with no delay (*left*) and 200 ms delay (*right*). **(D)** The same as (C), but for cursor velocity. **(E)** The same as (C), but for M1 LFPs. **(F)** The first two principal components of the LFPs. **(G)** The second LFP-PC is overlaid with the velocity trace. Data from monkey U.

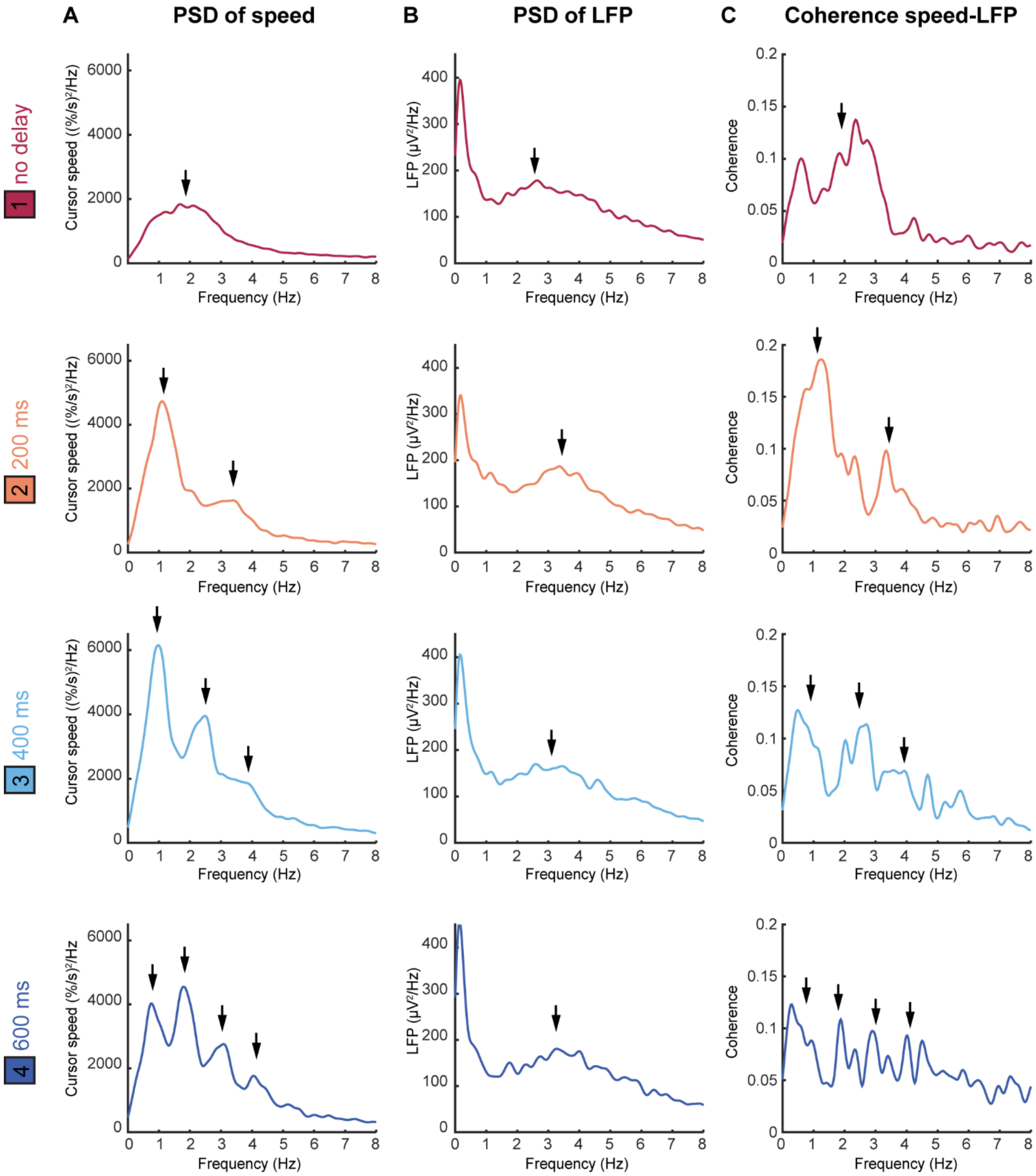

**Figure 5.4.2 Frequency analysis of speed and LFPs in monkey S.**

**(A)** Smoothed power spectrum of unfiltered cursor speed for different delay conditions. Arrows indicate delay-dependent submovement frequencies. **(B)** Smoothed power spectrum of surface-referenced unfiltered M1 LFPs for different delay conditions. Arrows indicate delay-independent peak. **(C)** Smoothed coherence spectra between unfiltered cursor speed and surface-referenced unfiltered, M1 LFPs for different delays. Arrows indicate delay-dependent coherence frequencies. Data were from monkey S averaged across all task blocks. Task-locked component was removed from both cursor speed and M1 LFPs.

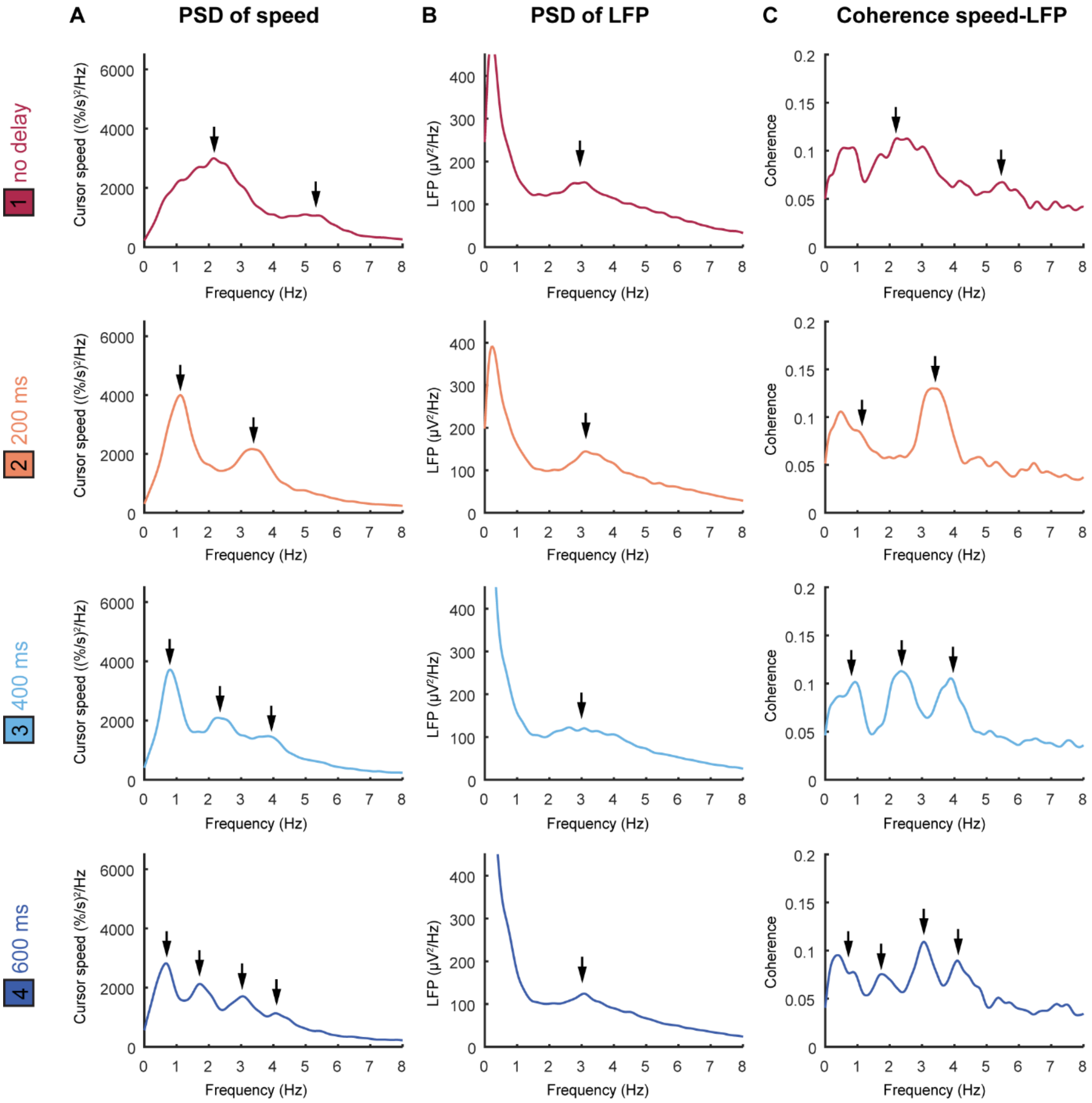

**Figure 5.4.3 Frequency analysis of speed and LFPs in monkey U.**

**(A)** Smoothed power spectrum of unfiltered cursor speed for different delay conditions. Arrows indicate delay-dependent submovement frequencies. **(B)** Smoothed power spectrum of surface-referenced unfiltered M1 LFPs for different delay conditions. Arrows indicate delay-independent peak. **(C)** Smoothed coherence spectra between unfiltered cursor speed and surface-referenced unfiltered, M1 LFPs for different delays. Arrows indicate delay-dependent coherence frequencies. Data were from monkey U averaged across all 15 sets of task blocks. Task-locked component was removed from both cursor speed and M1 LFPs.

In the no-delay condition, a peak around 3 Hz was seen in the power spectrum of the LFP (Figure 5.4.2(B) and Figure 5.4.3(B)). To see if this was correlated with the submovement peak, I analysed LFP-cursor speed coherence (a measure of correlation in the frequency domain). The coherence analysis between cursor speed and LFPs revealed a peak at the same frequency, around 2–3 Hz (Figure 5.4.2(C) and Figure 5.4.3(C)).

Based on our previous findings, I predicted that peaks in the LFPs, as well as in the LFP-speed coherence, would shift with increasing delay. Contrary to this prediction, I actually found that the peak in the LFP power spectrum remained at 3 Hz, despite the shift to lower frequencies of the peak in cursor speed spectrum. In the coherence spectra, when more delay was added, coherence peaks shifted with delay, in accordance with the shift in submovement peaks. Note that, similar to the submovement peaks, coherence peaks at higher harmonics peaks had a smaller amplitude, but this increased as their frequency decreased (with more delay). These findings were similar to the predictions made by the model (Figure 5.4.1).

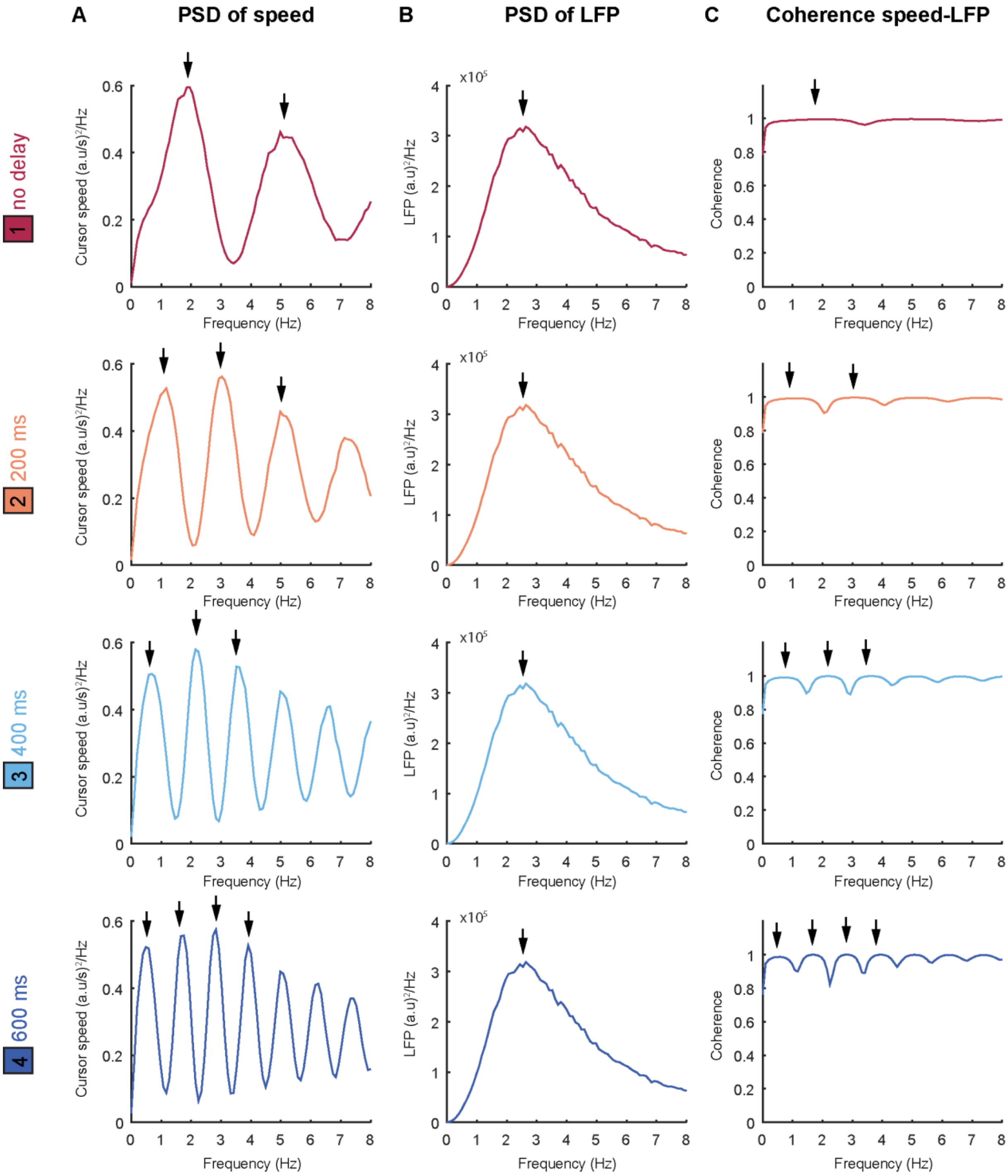

**Figure 5.4.4 Frequency analysis of speed and LFPs in the +*intrinsic dynamics* model.**

**(A)** Power spectrum of unfiltered cursor speed for different delay conditions. Arrows indicate delay-dependent submovement frequencies. **(B)** Power spectrum of unfiltered LFPs for different delay conditions. Arrows indicate delay-independent peak. **(C)** Coherence spectra between unfiltered cursor speed and unfiltered LFPs for different delays. Arrows indicate delay-dependent coherence frequencies.

## 5.5 Analysis of submovement related activity

Next, I looked at how submovement frequencies were represented in the time domain by looking at cursor speed and LFP activity related to the occurrence of a submovement. Submovements were identified from the cursor speed using a threshold, as described above.

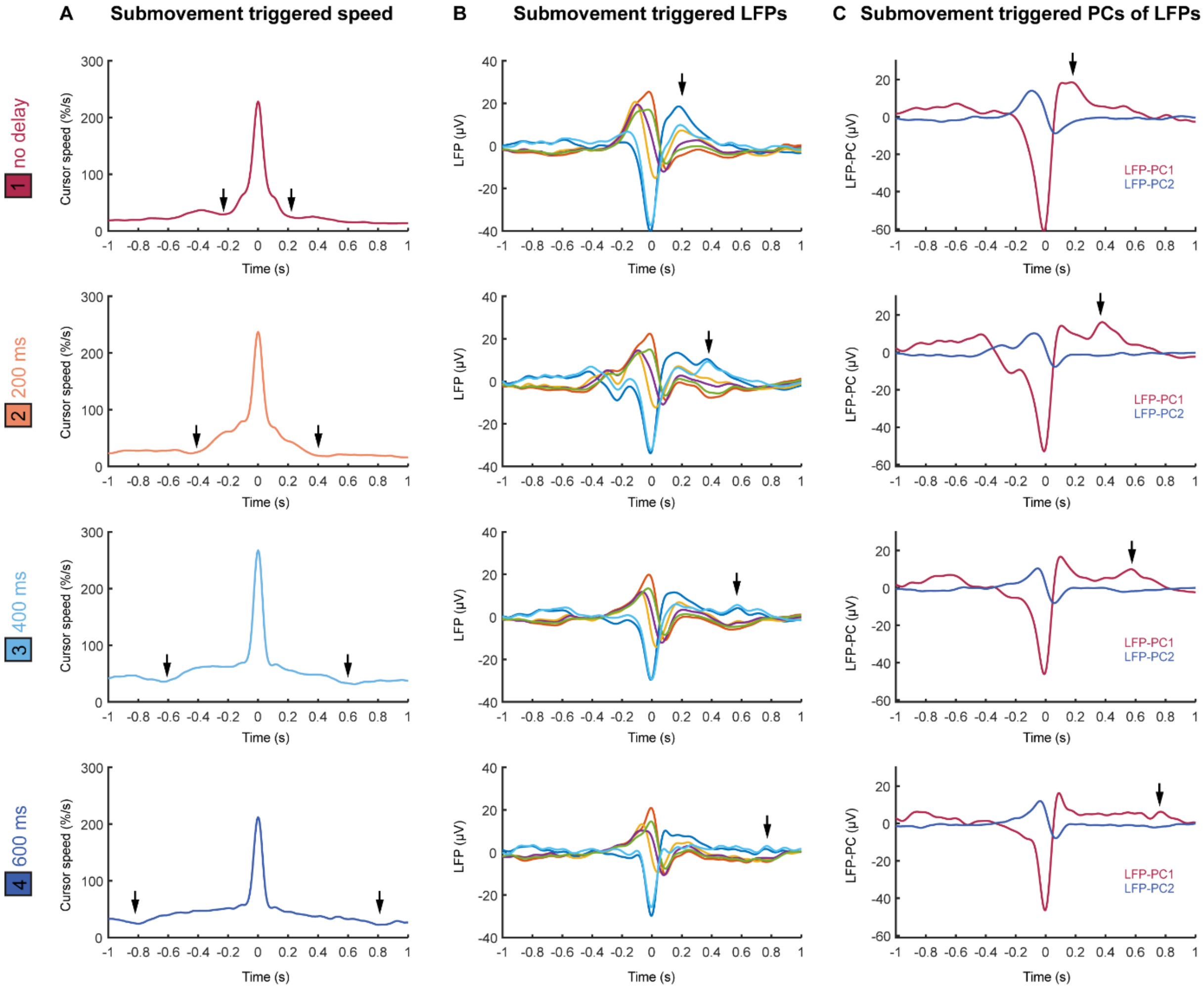

**Figure 5.5.1 Submovement related activity in monkey S.**

**(A)** Average low-pass filtered cursor speed, aligned to the peak speed of submovements for different delay conditions. Arrows indicate delay-dependent troughs. **(B)** Average surface-referenced band-pass filtered, LFP from six M1 electrodes, relative to submovements, for different delay conditions. Arrows indicate delay-dependent peaks. **(C)** Average LFP-PCs relative to submovements for different delay conditions. Arrows indicate delay-dependent peaks. Data from monkey S.

Submovement-triggered averages of speed revealed a central peak at the time of submovements and symmetric troughs either side of the central peak (Figure 5.5.1(A) and Figure 5.5.2(A)). With no delay added these troughs occurred at ±250 ms. When a delay of 200 ms was added, these troughs shifted to ±450 ms. The troughs shifted to ±650 ms and ±850 ms, respectively, when a delay of 400 ms and 600 ms was added. The shift in the troughs with experimental delay agreed with model predictions (Figure 5.5.3 (A)).

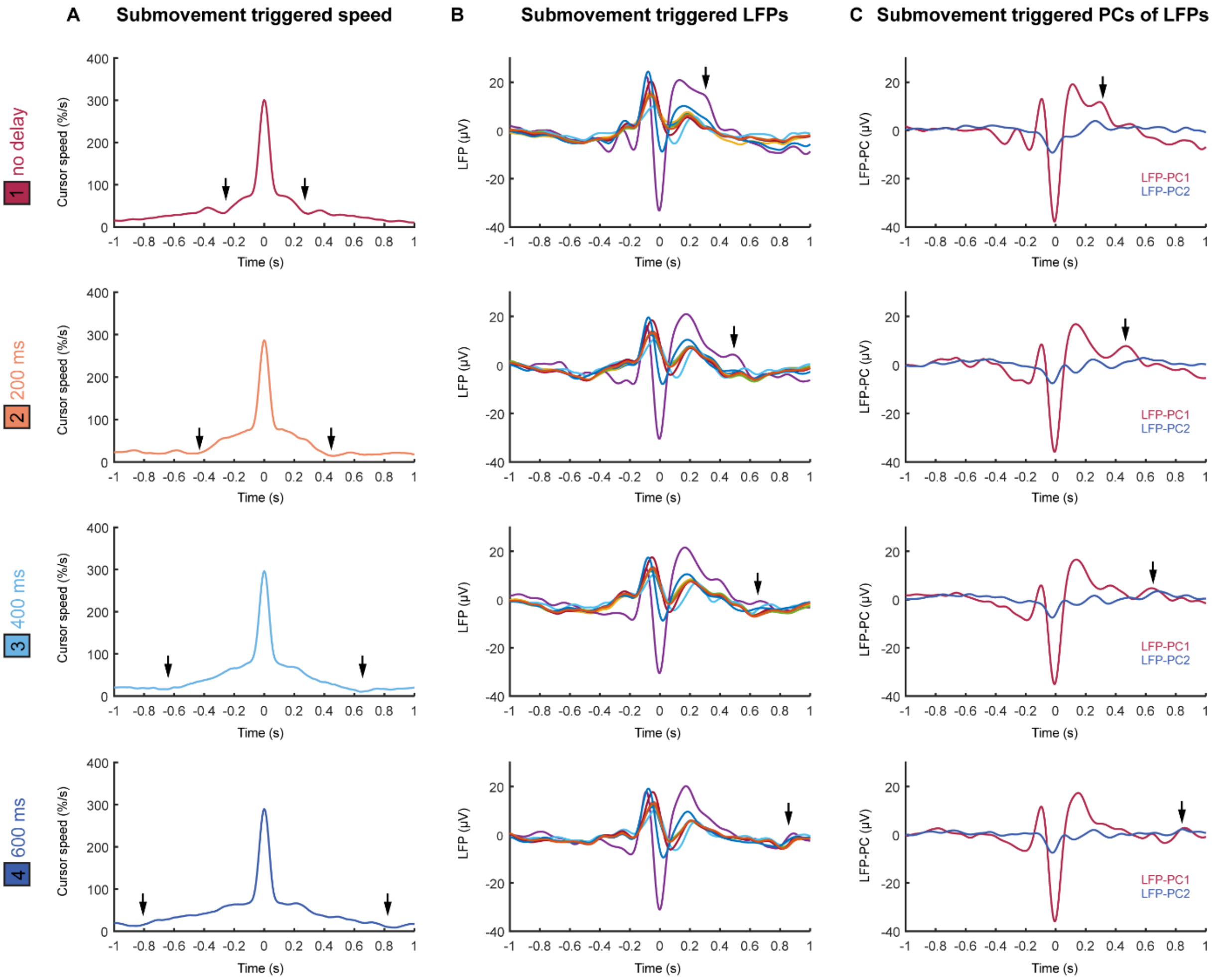

**Figure 5.5.2 Submovement related activity in monkey U.**

**(A)** Average low-pass filtered cursor speed, aligned to the peak speed of submovements for different delay conditions. Arrows indicate delay-dependent troughs. **(B)** Average surface-referenced band-pass filtered, LFP from six M1 electrodes, relative to submovements, for different delay conditions. Arrows indicate delay-dependent peaks. **(C)** Average LFP-PCs relative to submovements for different delay conditions. Arrows indicate delay-dependent peaks. Data were from monkey U comprising of one set of task block.

Submovement-triggered averages of LFPs revealed a low-frequency oscillation around the time of submovements (Figure 5.5.1(B) and Figure 5.5.2(B)). LFP channels exhibited different phases of oscillation in relation to the occurrence of submovements, and this was reflected in the first two LFP-PCs ((Figure 5.5.1(C) and Figure 5.5.2(C)).

This low-frequency submovement related oscillation occurred at the same frequency, irrespective of delays. Moreover, the phase relationship between LFPs was constant across delay conditions. Our model was able to predict this central, low-frequency, delay-independent oscillation (Figure 5.5.3 (B–C)).

As well as the delay-independent central oscillation, the submovement-triggered LFP and LFP-PCs exhibited a peak after the occurrence of submovement, coinciding with the timings of the troughs in the submovement-triggered speeds. However, unlike the symmetric troughs seen in the submovement-triggered speed, the submovement-triggered LFP exhibited an asymmetric peak, only present after submovements. When no delay was added, this peak occurred at +250 ms. When a delay of 200 ms was added the peak shifted to +450 ms. The peak shifted to +650 ms and +850 ms, respectively, when a delay of 400 ms and 600 ms was added. Our model was able to predict this delay-dependent peak, occurring after the delay-independent central oscillation (Figure 5.5.3 (B–C)).

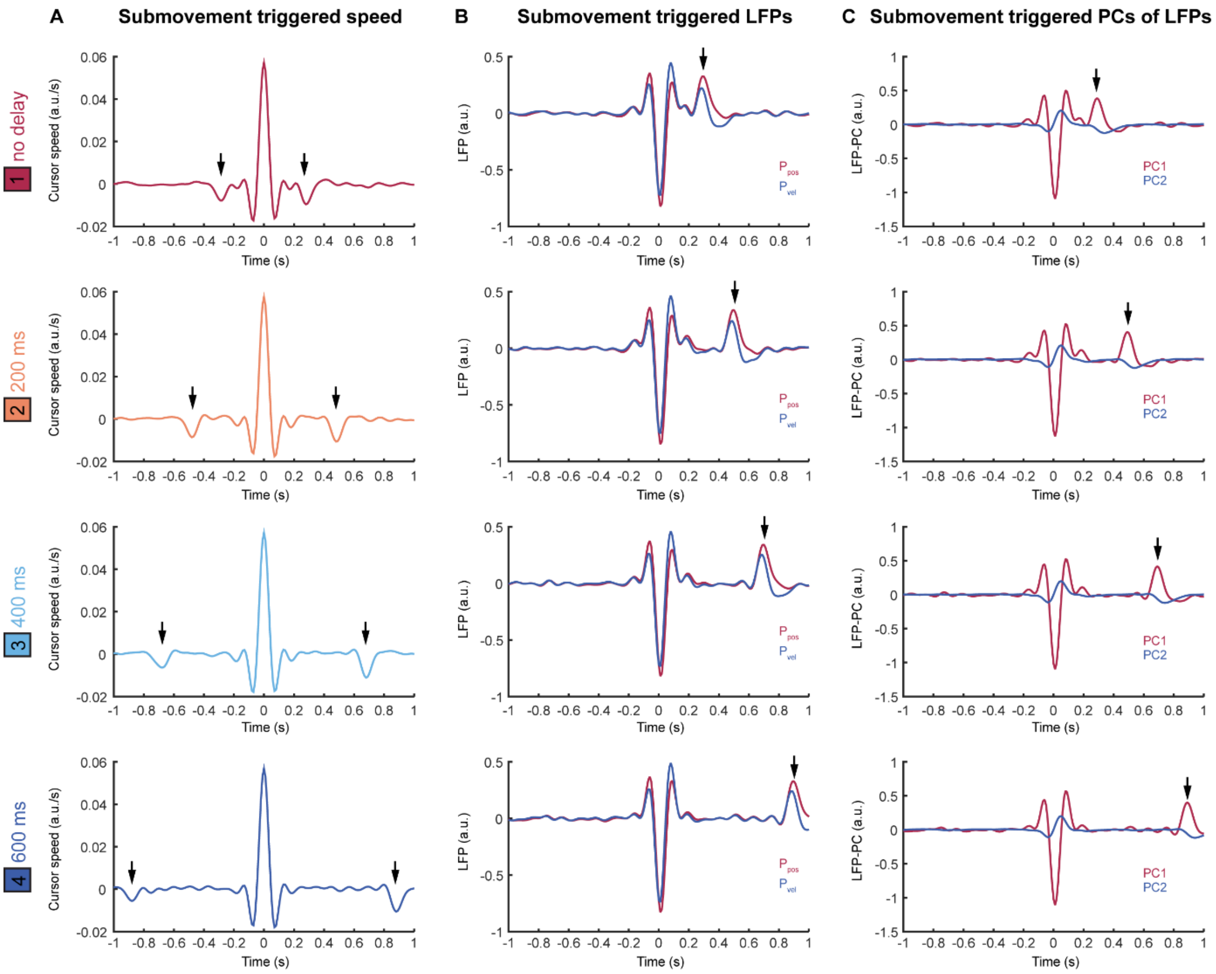

**Figure 5.5.3 Submovement related activity in the data generated by the *+intrinsic dynamics* model.**

**(A)** Average low-pass filtered cursor speed, aligned to the peak speed of submovements for different delay conditions. Arrows indicate delay-dependent troughs. **(B)** Average band-pass filtered, LFPs relative to submovements for different delay conditions. Arrows indicate delay-dependent peaks. **(C)** Average LFP-PCs relative to submovements for different delay conditions. Arrows indicate delay-dependent peaks.

## 5.6 Analysis of submovement-triggered LFP-PC trajectories and imaginary cross-spectral density of LFPs

Submovement-triggered averages of LFP-PCs revealed a central delay-independent low-frequency oscillation (Figure 5.5.1–3 (C)). Plotting the first two LFPs against each other revealed the cyclical trajectory of this oscillation in state space (Figure 5.6.1(A)). This cycling activity had a period of around 400 ms, equivalent to a frequency of 2−3 Hz. Surprisingly, despite the change in submovement frequencies with the addition of artificial delay, the cycling frequency was conserved across delay conditions. This conserved cycling frequency of submovement-triggered LFP-PC trajectories across delay conditions was predicted by the model.

Next, the phase relationships across LFP channels was measured using imaginary cross-spectral density (CSD) analysis. Imaginary CSD assesses the consistency of quadrature (90°) phase differences between two signals. Imaginary CSD across LFPs revealed a peak at 3 Hz, which was predicted by the model (Figure 5.6.1 (B)).

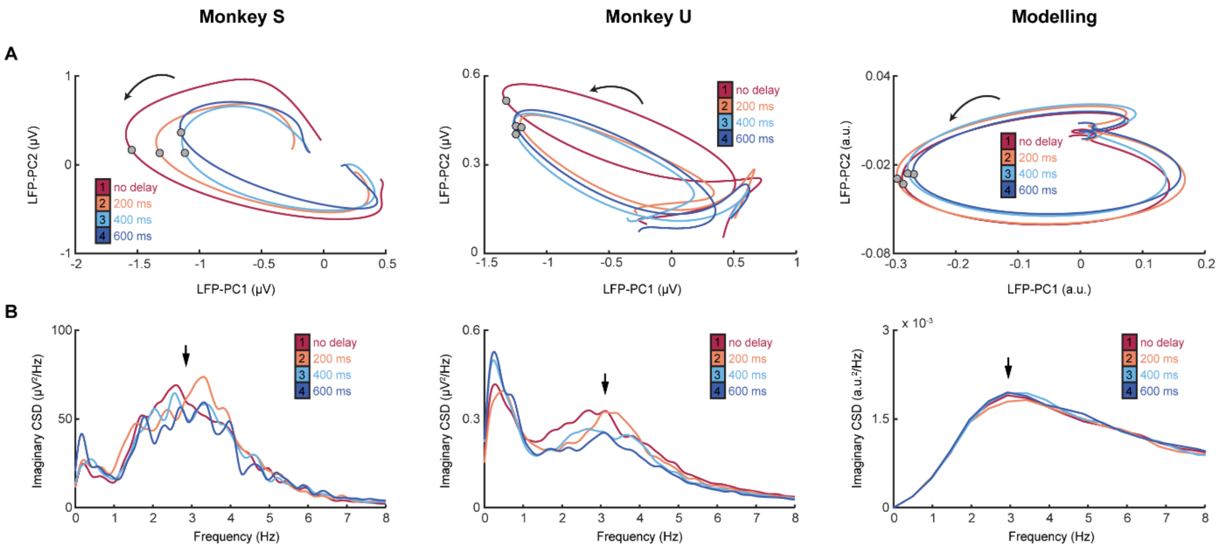

**Figure 5.6.1 Delay-independent low-frequency rotational structure in LFP**

**(A)** Average submovement-triggered LFP-PC trajectories, plotted over 200 ms on either side of peak speed (indicated by circles) for different delay conditions. Note the delay-independent rotational structure. **(B)** Imaginary cross-spectral density between unfiltered surface-referenced LFPs. Arrows indicated delay-independent low-frequency peak.

## 5.7 Prediction of LFP activity during sleep

During sleep occurrences of large potential changes have been described as K complexes. A K complex typically consists of a positive-negative-positive waveform and has been associated with slow wave sleep (Amzica and Steriade, 1997). Moreover, the period of K complex waveforms is between 200–400 ms (Colrain, 2005), that is at the same range of frequencies of submovements. Therefore, the K complex could be used as a triggering signal to see whether the relationship across LFPs during movement was preserved during sleep (Hall *et al.*, 2014).

Submovement-triggered averages of LFPs were previously reported in monkeys to exhibit a low-frequency oscillation with different phase relationships (Hall *et al.*, 2014) (Figure 5.7.1 (A-B)). Furthermore, when LFPs were averaged triggered to the occurrence of K-complexes during sleep, LFPs preserved the same phase relationships across channels (Figure 5.7.1 (D-E)). Moreover, cycling at a low-frequency was seen in the LFP-PC trajectory whether during awake behavior or sleep (Figure 5.7.1 (C, F)).

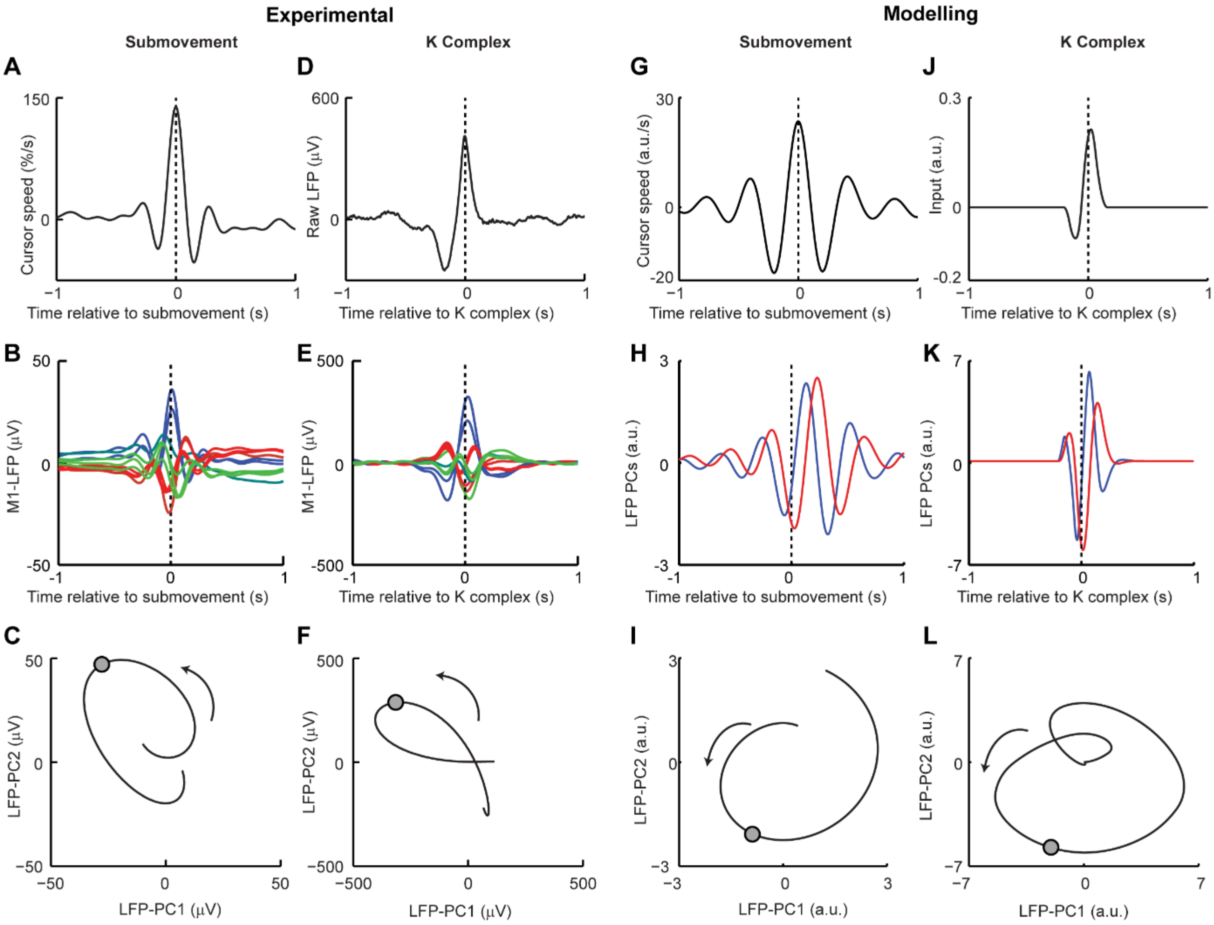

**Figure 5.7.1 The model predicted a rotational structure during sleep.**

**(A)** Average cursor speed aligned to the peak speed of submovements in monkey D. **(B)** Average low-pass filtered, mean-subtracted LFP from ten M1 electrodes relative to submovement. LFPs were colour coded into groups of similar phase relative submovements. **(C)** Average submovement-triggered (LFP-PC trajectories, plotted over 200 ms on either side of the trigger event (indicated by circles) in monkey D. **(D-F)** The same as (A-C), but for K complexes. **(G-L)** The same as (A-F) but for simulated data from the *+intrinsic dynamics* model. Panels A-F reproduced from Hall *et al.* (2014).

The model predicted many features seen in the LFPs during awake behavior. These features include a low-frequency oscillation and cycling of state-space trajectories during a submovement (Figure 5.7.1 (G-I)). To see if the model could predict similar cycling activity during sleep, I simulated LFP activity during sleep. Since during sleep no visual feedback is received and no movement is carried out, the external loop of the feedback loop was ignored (see schematic of model in Figure 5.7.2). I simulated each K-complex (effectively an down-to-up state transition) as a large spike input into the intrinsic dynamics component of the model (Figure 5.7.1 (J-

K)). Similar to the experimental results, the model predicted cycling at a low-frequency (Figure 5.7.1 (L)).

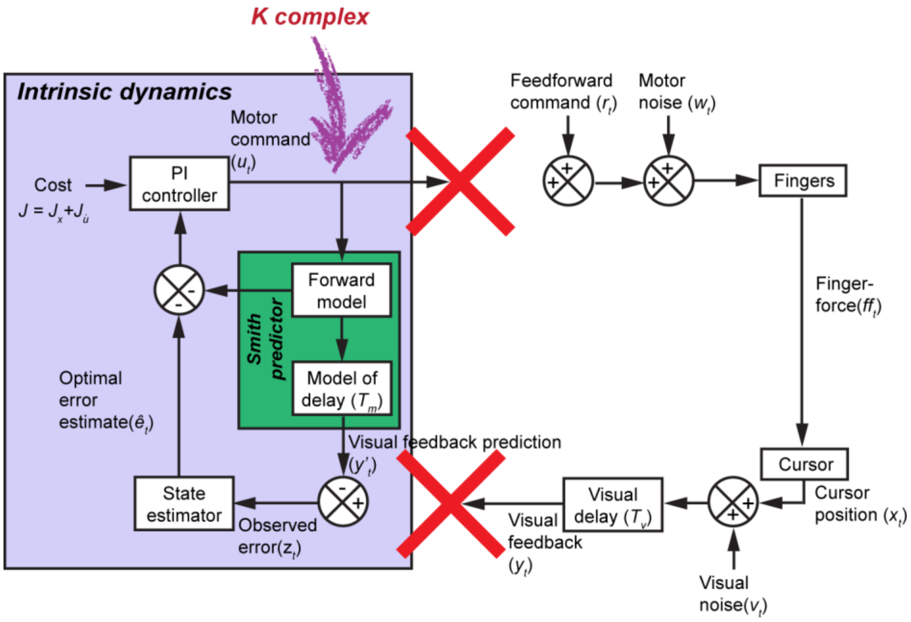

**Figure 5.7.2 Simulation of K-complexes during sleep in the +*intrinsic dynamics* model.**

Each K-complex was simulated as a large spike input into the intrinsic dynamics component of the model. During sleep, no visual feedback was received and no movement was carried out. Hence the external loop of the feedback loop was ignored.

## 5.8 Discussions

In this chapter, I have investigated extrinsic and intrinsic contributions to LFP dynamics during visuomotor tracking by experimentally delaying visual feedback, in a non-human primate (NHP) animal model. I found that submovement frequencies changed systematically with an increase in delay, in a similar fashion to the pattern seen in human tracking. I found some features of the LFP which also changed with delay. However, I also found a 3 Hz rhythmicity in the multi-channel LFP that was unchanged by delay. These features were reproduced by the model. Furthermore, the model predicted network activity during sleep, which reproduced experimental data.

### *5.8.1 Delay-dependent features in behaviour and LFPs*

I have replicated the results of previous studies which showed that peaks of submovement frequencies shift with increasing delay in humans, as well as in monkeys (Miall et al., 1986). Simulations of the feedback controller model with intrinsic dynamics reproduced submovement frequencies and their dependency on delay. This result suggests that NHPs (at least, rhesus macaques) use a similar mechanism to humans when performing a visuomotor task. This supports the surprising finding that submovements reflect frequencies at which visuomotor noise is exacerbated.

LFPs were strongly correlated with submovements, as revealed in the coherence between speed and LFPs at submovement frequencies. This is consistent with previous findings of coherence at 2–5 Hz between MEG (magneto-encephalography) and submovements in humans (Jerbi *et al.*, 2007), and between LFP and submovements in monkeys (Hall *et al.*, 2014). With the introduction of artificial delay, I have identified clear correlates of submovements, as speed-LFP coherence peaks shifted in concert with the shift in submovement frequencies.

In the time domain, submovement-triggered averages of speed revealed symmetric troughs either side of the central peak, which reflect the rhythmicity of submovements. In the absence of perturbation, this was governed by internal time delay between visual feedback and movement, but increased systematically as artificial delay was added. The timing of these troughs coincided with a late feature in the submovement-triggered LFP. However, unlike submovement-triggered speed profiles, the submovement-triggered LFP was asymmetric, since no feature preceded the time of submovements.

These somewhat counterintuitive results were replicated by the model and can be understood by examining the schematic in Figure 5.8.1. A submovement (peak in speed) can arise from two different causes: a positive peak in the motor noise (*red circle 1*) or a feedback correction following a prior negative trough in motor noise (*red circle 2*). Were it possible to compile a submovement-triggered average of the motor noise, this would therefore show a central peak (1) and a preceding trough (2). By contrast, the submovement-triggered LFP contains a superposition of the current feedback correction (2) of the negative noise, and a delayed component reflecting a future correction to the positive noise peak (1). The submovement-triggered average of speed comprises the difference in these traces (since the LFP drives a negative feedback correction that is added to the motor noise) and thus comprises three features: a central peak and two troughs (before and after the time of submovement).

In summary, I showed several delay-dependent features in behavior and LFPs. First, submovement frequencies shifted with delay. Second, LFPs were strongly correlated with submovements (as can be seen in speed-LFP coherence and submovement-triggered averages of LFPs). These results were predicted by my model, and can be explained by a framework in which submovements arise from exacerbated correction of noise.

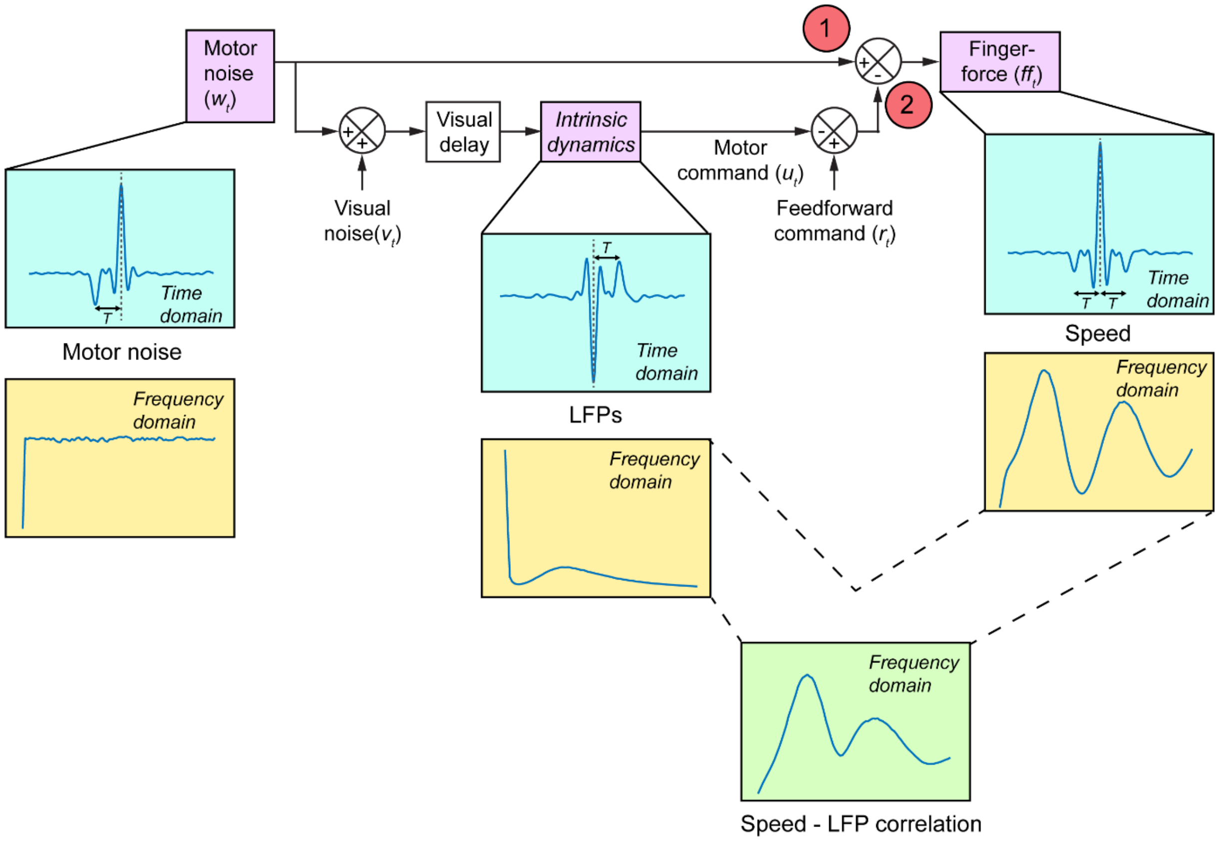

**Figure 5.8.1 Schematic of submovement-triggered averages and frequency analysis results in the model.**

Submovement-triggered average results were predicted by the model. The peaks and troughs in the submovement-triggered average of speed were related to the peaks and troughs in the motor noise and in the negative of the peaks and troughs in the LFPs. See text for explanation. Power spectrum (*yellow boxes*) in the frequency domain are equivalent to the submovement-triggered averages (*blue boxes*) in the time domain.

### *5.8.2 Delay-independent features in behaviour and LFPs*

Similar to in humans, the envelope of the power spectrum of cursor speed across different delays exhibited evidence of a low-frequency band-pass filter being present. This was manifested by higher harmonic peaks of submovements having smaller amplitude, but this amplitude increasing as their frequency decreased with increasing delay.

I have shown that there is also evidence for this band-pass filter phenomenon in the coherence between speed and LFP irrespective of delays. The envelope of this coherence across delay conditions also had a shape of a low-frequency passband. Predictions made by our feedback controller model, including modelled intrinsic dynamics, reproduced these findings.

With no delay added, the submovement peak coincided with both a peak in the power spectrum of the LFP and the speed-LFP coherence at the same frequency. Therefore, one might assume that frequencies in the power spectrum simply reflect submovements. However, I found that the peak (around 3 Hz) in the power spectrum of LFP did not shift in concert with the shift in submovement frequencies and speed-LFP coherence. This delay-independent peak at ~3 Hz most likely reflects intrinsic dynamics in the feedback pathway and can be understood by the schematic in Figure 5.8.1.

According to my model, submovement frequencies result from summation of motor noise (*red circle 1*) and feedback correction of motor noise (*red circle 2*). This summation leads to constructive and destructive interference of motor noise, reflected in peaks and troughs in the power spectrum of speed, and periodic submovements evident in behaviour. This implies that submovement frequencies should not be seen in the power spectrum of LFP alone, since no summation of motor noise has occurred at this point. However, coherence between speed and LFP would show correlations at submovement frequencies, because the speed spectrum contains the same motor noise signal, but with modulated amplitudes.

In the time domain, submovement-triggered averages of LFPs revealed a central low-frequency oscillation, with multiple LFP channels having different phases in relation to submovements. These different phases were captured in the submovement-triggered averages of the principal component projections of the LFPs. The frequency of the submovement locked low-frequency oscillation could thus be inferred from the rotational frequency of the LFP-PC state-space trajectory. When no delay was added, cycling occurred at a frequency of 3 Hz. Similar rotational state-space trajectories, at a similar frequency and locked to submovements, have previously been shown in M1 neurons (Churchland et al., 2012) and LFPs (Hall *et al.*, 2014).

Because cycling in M1 activity is locked to submovements, and occurs at a similar frequency to submovements, one would initially assume that these findings simply reflect kinematics of movement. In this case, the cycling frequency would change if the kinematics changed. Knowing that the introduction of artificial delay would change the frequency of submovements, I assessed cycling activity when different delays were added. I expected that the cycling frequency would be altered in accordance with the shift in submovement frequencies. On the contrary, I showed that the cycling trajectory and frequency were not altered when delays were added, and thus did not reflect kinematics of movement. The cycling activity in M1 was unchangeable by extrinsic perturbation of delay and could reflect intrinsic properties of motor networks.

My model predicted the same delay-independent cycling of LFP-PCs, and this can be explained by properties of the state estimator. The LFPs were modeled crudely as a recurrent neural network implementing a state estimator with a band-pass filtered transfer function. A submovement (identified in the cursor speed as a positive spike) can arise from feedback correction following a prior negative trough in motor noise (Figure 5.8.1). A negative trough going through the state estimator will result in an oscillation in the position estimate and a 90° phase shifted oscillation in the velocity estimate. A state-space trajectory of these signals will thus result in cycling at 3 Hz (unchangeable by delays), which reflects the intrinsic properties of the state estimator.

Different phase relations to submovements were showed in the submovement-triggered averages of LFPs. These phase differences were conserved across different delay conditions and were reflected in the LFP-PCs and the delay-independent cycling trajectories of LFP-PCs. To assess quadrature (90°) relationships across LFPs, I calculated imaginary cross-spectral density (CSD) between pairs of LFP channels. I showed a 3 Hz peak (unchangeable by delays), which supports the argument that these LFP dynamics results from intrinsic properties of activity in M1. The model predicts the same delay-independent cycling of LFP-PCs, and this can be explained by properties of the state estimator. Imaginary CSD between LFPs in the model reproduced the 3 Hz peak seen in real data, and this property can also be explained by the state estimator.

In summary, I have shown several delay-independent features of behavior and M1 LFPs. First, the envelope of submovement spectra and speed-LFP coherence exhibited a band-pass filter at around 3 Hz, irrespective of delays. Moreover, the power spectra of LFPs, cycling activity of LFP-PCs, and imaginary cross-spectral density of LFPs all revealed activity at 3 Hz, independent of delays. The model simulated all these findings via the implementation of a state estimator, which combines sensory feedback with an internal dynamical model, to form optimal estimates of required motor corrections. Taken together, the experimental and modelling results suggest that M1 LFPs exhibit an intrinsic rhythmicity at a frequency of around 3 Hz (in NHPs).

### *5.8.3 LFP activity during sleep*

For further evidence that this postulated intrinsic rhythmicity is an inherent property of motor networks, one can look at brain states other than task-directed movement, such as during sleep. Sleep is characterized by inhibition of sensory feedback and voluntary movement. Thus, it can be argued that there is no need to use the state estimator during sleep. Though, if the state estimator reflects intrinsic dynamics of motor network, it should be conserved during sleep.

Previous work in the laboratory has shown that LFPs retain their phase relationship in relation to submovements during sleep (Hall *et al.*, 2014). These results were observed when averages of M1 LFPs were calculated relative to K-complexes, during slow-wave sleep. K-complexes represent synchronized down-to-up state transitions of the cortex, and may reflect intrinsic cortical rhythmicity during sleep. In support of this, the LFP-PC trajectory related to K-complexes displays cycling similar to the LFP-PC trajectory related to submovements. These experimental results support the existence of an inherent rhythmicity in the motor networks, and suggest that my proposed state estimator may be involved in sleep, as well as in movement. That is to say: it is a truly intrinsic property of motor areas. To test this, I simulated the effect of using a K-complex as the input to our intrinsic dynamics model, and saw similar LFP-PC cycling to that seen during simulated movement.

Sequential activity in M1 could be a signature of replay, as has been shown in the hippocampus during sleep, where it is correlated with memory consolidation. However, recent work from our lab has indicated that sequential activity in M1 is similarly conserved, even across varied learning tasks – suggesting that sequential activity may be an imposed intrinsic network constraint (Jackson *et al.*, 2017).

### 5.9 Chapter summary

- I investigated the effect of visual feedback delay on submovements and M1 LFPs in non-human primates (rhesus macaque monkeys).
- Submovement frequencies depend systematically on visual feedback delay.
- LFP activity was strongly correlated with submovements, at frequencies determined by experimental delays, as was predicted by our feedback controller model.
- An intrinsic rhythmicity at 3 Hz was found, and was not affected by experimental delay. This matched the properties of the state estimator in our optimal feedback control model.
- Taken together, these findings suggest that both delay-dependent and delay-independent features of LFP contribute to the generation of submovements.

# Chapter 6. General discussion

## 6.1 Main findings of this thesis

In this thesis I aimed to re-examine extrinsic and intrinsic contributions to submovements in the framework of optimal feedback control (OFC) theory. Extrinsic manipulations in the form of temporal (delay) and spatial (velocity) perturbations were added to distinguish between features in behaviour and neural activity that were dependent and independent of perturbations. I found both perturbation dependent and independent features which I classify into extrinsic and intrinsic features (Table 6.1.1).

**Table 6.1.1 Summary of extrinsic and intrinsic features found in behaviour and neural activity.**

| **Extrinsic** | **Intrinsic** |
|---|---|
| Submovement frequencies shifted with artificial delay in both humans and monkeys. | Envelope of submovement spectra exhibited a delay-independent bandpass filter. |
| Exacerbation of velocity perturbation occurred at submovement frequencies and shifted with submovements when artificial delay was introduced. | Feedback response to velocity perturbations revealed delay-independent bandpass filtering at 2–3 Hz. |
| Coherence between cursor velocity and M1 LFPs shifted with submovement frequencies when artificial delay was added. | Power spectra of LFPs revealed a peak at 3 Hz irrespective of artificial delay. |
| LFP activity was locked to submovements and corrective responses shifted with delay. | Slow oscillation and phase differences across LFPs locked to submovements was conserved when delay was added and a consistent phase relationship between LFPs was revealed at 3 Hz. |

These findings were explained by a feedback controller model which incorporated a Smith predictor to predict delayed consequences of movement. Furthermore, a state estimator was implemented to optimally estimate cursor position and velocity in the presence of noisy delayed visual feedback.

Our model makes three main predictions:

1) submovements reflect exacerbation of visuomotor noise;
2) submovement kinematics reflect both extrinsic and intrinsic dynamics; and
3) M1 LFPs reflect a recurrent neural network involved in state estimation.

Next, I will discuss these three predictions in turn.

## 6.2 Submovement reflect exacerbation of visuomotor noise

Our model predicts that submovements arise from feedback corrections to visuomotor noise, and that they reflect exacerbation of noise. I tested this prediction by injecting artificial noise to the visual feedback system, and found that humans do exacerbate noise at submovement frequencies, consistent with the model's prediction. There are three key points to discuss further with regard this result.

### *6.2.1 The role of visual feedback in the generation of submovements*

First, these findings highlight the importance of visual feedback in the generation of submovements. Submovements are observed more clearly when the feedback given to subjects is an error signal (i.e. compensatory tracking) instead of separate cursor and target signals (pursuit tracking) (Miall *et al.*, 1988). This suggests that feedback of error is essential to revealing submovements.

Furthermore, submovements are suppressed when visual feedback is removed during compensatory tracking (Miall *et al.*, 1993a) but the opposite finding has been demonstrated during pursuit tracking (Miall *et al.*, 1993a; Doeringer and Hogan, 1998). It is possible that during pursuit tracking, error correction is performed based on the difference between the cursor and a memory of the target (Miall *et al.*, 1993a). Indeed, tracking accuracy has been shown to be a crucial factor that determines whether submovements are present (Reed *et al.*, 2003). This is consistent with my experiment in which subjects were instructed to minimize error.

Here I have also shown that when feedback delay is added, the exacerbation of noise shifts with the shift in submovement frequencies. This finding agrees with the consistent finding that submovements depend on visual feedback delays (Pew, 1974; Miall, 1996).The question arises, however, whether submovements are a phenomenon limited to systems involving visual feedback. Interestingly, intermittency has been reported in the kinematics of finger movement during Braille reading (Hughes *et al.*, 2014), during haptic tracking (Creighton and Hughes, 2017), and during a balancing task using vestibular and proprioceptive information (Lakie and Loram, 2006). These findings suggest that intermittency/submovements may be a general signature of sensorimotor pathways – extending to auditory, haptic, and proprioceptive feedback.

### 6.2.2 Submovements reflect filtered noise instead of movement segmentation

Second, my findings reveal that submovements reflect filtered noise, instead of segmentation of movements. I have shown that comb filtering of visuomotor noise results in submovement peaks in the power spectra. The idea of submovements arising from noise circulated through a feedback loop with delay has previously been proposed by Pew (1974). This idea can be implemented in a feedback controller model when a Smith predictor is included. The Smith predictor prevents visuomotor noise from being recirculated through the feedback loop multiple times. Thus, the feedback controller model is equivalent to a feedforward comb filter with a finite impulse response (FIR).

My model is completely linear, whereas previous models have needed to introduce non-linearities to reproduce intermittency. In these intermittent control models, explicit segmentations of movement are triggered after a given time period (refractory period), an error threshold, or reduced reliability of the internal model (Neilson *et al.*, 1988; Gawthrop *et al.*, 2011; Sakaguchi *et al.*, 2015).

Previous work, using a double-step stimulus task with a positional stimulus, has shown the refractory period to be around 500 ms (Craik, 1947). Elsewhere, it has been reported to be 250 ms, and increased by the order of the system (i.e. whether position, velocity, or acceleration was controlled) (van de Kamp *et al.*, 2013). These findings suggest that the complexity of state estimation affects the refractory period. The reaction time for the first stimulus in the double-step stimulus task ranged between 200 and 300 ms (Craik, 1947; van de Kamp *et al.*, 2013) and also increased with increase in the order of the system controlled (van de Kamp *et al.*, 2013).

Consistent with these reaction times, in my experiment I found that subjects responded to sinusoidal perturbations with a delay of 250 ms, irrespective of artificial delay. However, it seems unlikely that there was a refractory period, since subjects were able to respond to sinusoidal perturbations as high as 5 Hz, which is equivalent to a double-step stimulus with an interval of half of the period: so ~100 ms. It could be the case that the refractory period (reported to be around 250 ms (van de Kamp *et al.*, 2013)) was reduced during tracking. Indeed, in-flight corrections to a cursor step perturbation have been found to start as quickly as 100 ms (Dimitriou et al., 2013). Nevertheless, it would be interesting to measure the refractory period using a double-step stimulus given during visuomotor tracking.

To summarize, in my model, submovements did not arise from segmentation of movement—in which ballistic movements are executed periodically after a refractory period—but instead from filtering of noise, in which corrections to delayed error result in comb filtering. It can be shown, though, that this filtering can occur from error correction in a system with a refractory period or sampling period of 100 ms.

Using a compensatory tracking task, Wolpert and colleagues (1992) found an intrinsic error ‘deadzone’, in which corrections to error were not initiated. This deadzone could have been caused by limited visual processing accuracy, but actually was found to be extrinsically dependent on target speed, viewing distance, and amplitude (Wolpert et al., 1992). The presence of an intrinsic error deadzone did not explain why submovements occurred rhythmically, unless error reached the threshold periodically. Instead, error at the start of submovements was found to be normally distributed (Wolpert et al., 1992). It is interesting to ask whether the addition of a ‘deadzone’ to my model would still lead to the production of submovements, but it is important to note that, in my model, submovements did not arise from segmentation caused by a deadzone, but from comb filtering.

Lastly, intermittency has been proposed to arise from segmentation determined by the reliability of the internal model’s prediction of the target (Sakaguchi et al., 2015). In this model, segmentation of movement is triggered by a large difference between the predicted and observed target position. However, no other evidence was shown to support this hypothesis, besides the similarity in kinematics between humans and simulations.

### ***6.2.3 Submovements reflect error correction of noise***

Finally, my findings unify two interpretations of submovements: that reflect (1) noise, and (2) error corrections. Previously, these two interpretations have been seen separately, with evidence supporting submovements originating from neuromuscular noise (Celik *et al.*, 2009) or from error corrections arising from visual feedback (Miall *et al.*, 1993a). In my model, submovements arise from error corrections to noise, which lead to exacerbation of noise at submovement frequencies.

## 6.3 Submovement kinematics reflected both extrinsic and intrinsic dynamics

The model predicted that kinematics of submovements were determined by the extrinsic visual feedback loop delay and resonance frequencies of intrinsic dynamics. Submovements occurred at frequencies at which exacerbation of noise occurred dependent on the visual feedback delay. However, these frequencies were also filtered through intrinsic dynamics. I showed that during tracking the feedback response to sinusoidal perturbations were filtered through a 2-3 Hz bandpass filter. There are two questions that arise: where does intrinsic dynamics arise from and what is the function of intrinsic dynamics.

### *6.3.1 Where does intrinsic dynamics arise from?*

My results suggest that intrinsic dynamics did not reflect properties of visuomotor noise, the feedforward pathway, nor visual processing. Therefore, I speculated that intrinsic dynamics reflected state estimation. The filtering properties of intrinsic dynamics were consistent with a state estimator required for optimal feedback control (OFC) in the presence of visual and motor noise. I showed that M1 LFPs matched properties of this state estimator. The question arise whether this intrinsic rhythmicity was determined by hard wiring of the network or whether it was shaped by experience. It would be interesting to ask in what situations this intrinsic rhythmicity is changed. For example when we change the order of control or when we change the motor to sensory noise ratio by perturbing the motor or sensory pathways. Whether it is shaped by experience can be studied in a development experiment. Moreover, it is interesting to ask whether these properties can be found in other brain regions such as in the posterior parietal cortex (PPC) and the cerebellum and whether M1 LFPs reflect input from these areas. These areas are relevant because the posterior parietal cortex (PPC) has been thought to be responsible for state estimation (Mulliken *et al.*, 2008) and the cerebellum has been thought to be involved in a forward model (Miall *et al.*, 1993b; Blakemore *et al.*, 2001). It is likely that a distributed network comprising both cortical and subcortical brain circuits is involved in feedback control (Scott, 2004).

### *6.3.2 Evidence for intrinsic dynamics in rhythmical behaviours*

It is interesting to note that the frequency of intrinsic dynamics at 2 Hz has often been seen in other types of task besides visuomotor tracking. When experienced musicians were asked to tap while listening to different genres of music, the tempi distribution revealed a resonance spectra at 2 Hz (van Noorden and Moelants, 1999). In a seminal study, Kelso (1984) showed that bimanual anti-phase movement transitioned into in-phase movements at a frequency of 2 Hz. Moreover, tapping movements have been shown to transition from discrete movements into rhythmic movements at 2 Hz when the target frequency was increased (Huys *et al.*, 2008). Indeed it has been shown that moving slowly is avoided (van der Wel *et al.*, 2009). All these findings support the presence of an intrinsic dynamics with a resonance frequency of 2 Hz. Moreover, a transition seem to occur at 2 Hz with movement below 2 Hz performed using corrections of error (feedback control) and movement above 2 Hz performed in a ballistic fashion (feedforward control). It has been shown in an inverted pendulum task that entrainment between target and effector occurred when the target frequency is higher than effector Eigen frequency (Russell and Sternad, 2001). It could be the case movement at 2 Hz reflect entrainment between intrinsic dynamics in M1 LFPs and human limbs and hence is more stable. Indeed, moving intermittently at 2 Hz has been argued to be more optimal compared to moving continuously (Loram *et al.*, 2011). It could be possible that intrinsic dynamics is reflected in ballistic movements at 2 Hz when accuracy is not required, and filtered feedback responses at 2 Hz when accuracy is required. Thus, this does not necessary suggest that a different network is involved in producing feedback and feedforward movements. This is supported by the finding that similar regions in a positron emission tomography (PET) study were activated during both fast and slow handwriting in humans (Siebner *et al.*, 2001).

## 6.4 Rotational state-space trajectories of M1 LFP reflect a recurrent neural network involved in state estimation

My model predicts that M1 LFPs reflect a recurrent neural network performing state estimation. I found that M1 LFP features matched predictions made by the model. Specifically, I have shown that M1 LFP rotations in state-space (locked to submovements) do not change with external delays, despite the shift in submovement frequencies.

Rotations in state-space trajectories of M1 neural activity have been thought to reflect evolution of states from preparatory state to execution of movement (Churchland *et al.*, 2012; Shenoy *et al.*, 2013). Hall and co-authors (2014) showed that these cycles are locked to submovements. Hence, each submovement can be thought as an individual movement plan, evolving from preparation to execution state. However, the authors also showed that these cycles were present during slow-wave sleep, locked to K-complexes. Furthermore, the LFPs conserved the same phase relationship in sleep as in movement. The authors consequently interpreted these rotations as an intrinsic rhythmicity (Hall *et al.*, 2014).

In my results, I have shown that both the rotations and phase relationship across LFPs were conserved, irrespective of the change in submovement frequencies with delay. Therefore, the rotations could not reflect individual motor plans of submovements. Instead, the rotations were consistent with the idea of an intrinsic rhythmicity shaping the temporal evolution of submovements.

The conserved rotational trajectory across delay conditions matched predictions by the model. In the model, this rotational trajectory would be expected from a state-estimator estimating cursor position and velocity. Rotational trajectories of M1 LFP could therefore be thought of as reflecting a recurrent neural network estimating cursor position and velocity. Consistent with the idea of M1 acting as a state estimator is the finding that M1 activity reflect changes in afferent signals (Herter *et al.*, 2007).

In my isometric task, cursor position and velocity were equivalent to torque and differentiated torque. This does not necessarily mean that M1 encodes position and velocity or torque and differentiated torque. In fact, M1 activity has previously been found to be correlated with various parameters related to both kinetics and kinematics (Fetz, 1992; Shenoy *et al.*, 2013). In my model, bandpass filtering was dependent on the properties of process (muscle) and measurement (sensory) noise. Therefore position and velocity can be replaced with other kinematic/kinetic parameters, perhaps dependent on the dimensions being controlled. In this view, motor cortex can be seen as a flexible pattern generator, controlling task-specific dimensions in accordance with the uncontrolled manifold (UCM) hypothesis (Latash *et al.*, 2002).

In summary, I suggest that motor cortical rhythmicity reflects recurrent circuitry that combines sensory feedback with an internal dynamical model to form optimal estimates of required motor corrections.

## 6.5 Future directions

### *6.5.1 A framework to generalize findings*

In my model I focused on explaining feedback control and assumed that feedforward control of the target position was perfect even when delay was added. Further studies should explore a general framework to combine both feedforward and feedback movement while still being able to explain submovements and intrinsic dynamics. Moreover my results were found specifically during a visuomotor tracking task. Daily tasks require a combination of different type of movements, hence it would be interesting to be able to predict different types of movement using my model. Finally, in my task I ignored dynamics of the plant. This was applicable in my model since the movement made were isometric. However, this might need to be included in the model when more complicated movement are modelled.

### *6.5.2 Removing submovements*

My results showed that submovements reflect exacerbation of noise. Therefore one can ask whether these submovements can be predicted and removed from the movement. This could have applications in tele-robotic control, in which there is a long delay in the control loop. Moreover, if we can identify the source of this noise (i.e. from the movement planner, neural signal, or muscle noise) then we can find a way to overcome the introduction of this noise. For example if the noise originates from the muscles, we could use another actuator, like a robotic arm in a brain-controller interface setting. Finally, smoother control of movement could be achieved if we find a way to bypass the significant delay in the sensorimotor feedback loop.

### *6.5.3 Evidence for a smith predictor*

In this model, perfect knowledge of the feedback loop delay was required for stable tracking. Evidence for a Smith predictor has been previously debated (Miall *et al.*, 1993a; Foulkes and Miall, 2000; Miall and Jackson, 2006), but my results suggest that the Smith predictor is able to adjust its delay model on a trial-by-trial basis.

Further studies should address how the brain encodes this delay and incorporates the Smith predictor during movement.

## 6.6 Conclusions

In summary, by combining human behavioural studies, computational modelling and monkey electrophysiology, I show how movement intermittency can be explained by the interplay of both extrinsic and intrinsic dynamics within an OFC framework.

# Appendix A. Target speed tracking experiment

An experiment was performed with the aim to see the effect of target speed on submovement frequencies. I used the same tracking task as has been described in section 2.1.1. The same subjects participated in this task. There was a slight increase in submovement frequency when target speed was increased from 0.1 Hz to 0.2 Hz (Figure appendix A 1 and Figure appendix A 2), although this was only significant in the no delay condition ($t(7) = –3.38$ ,$p = 0.01$). This was not significant in the 200 ms delay condition ($t(7) = –2.05$ ,$p = 0.08$ and $t(7) = –1.59$ ,$p = 0.16$ for the first and second peak, respectively).

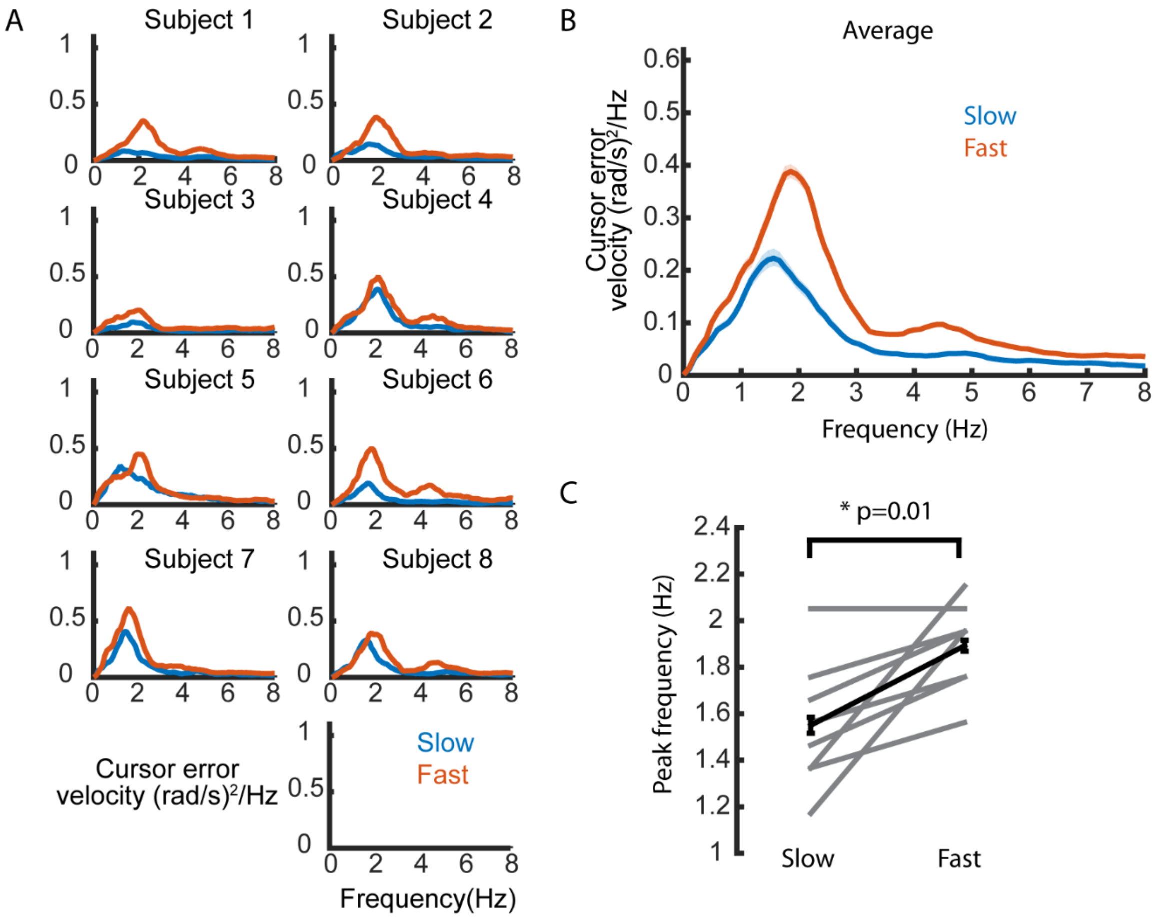

**Figure appendix A 1 Smoothed power spectra of cursor velocity at different target speeds in the no delay condition.**

**(A)** Smooth power spectra of cursor velocity in individual subjects for slow (0.1 Hz) and fast (0.2 Hz) target speed. **(B)** Average of power spectra of cursor velocity across subjects (n=8). **(C)** Comparison of submovement frequency between slow and fast target speed.

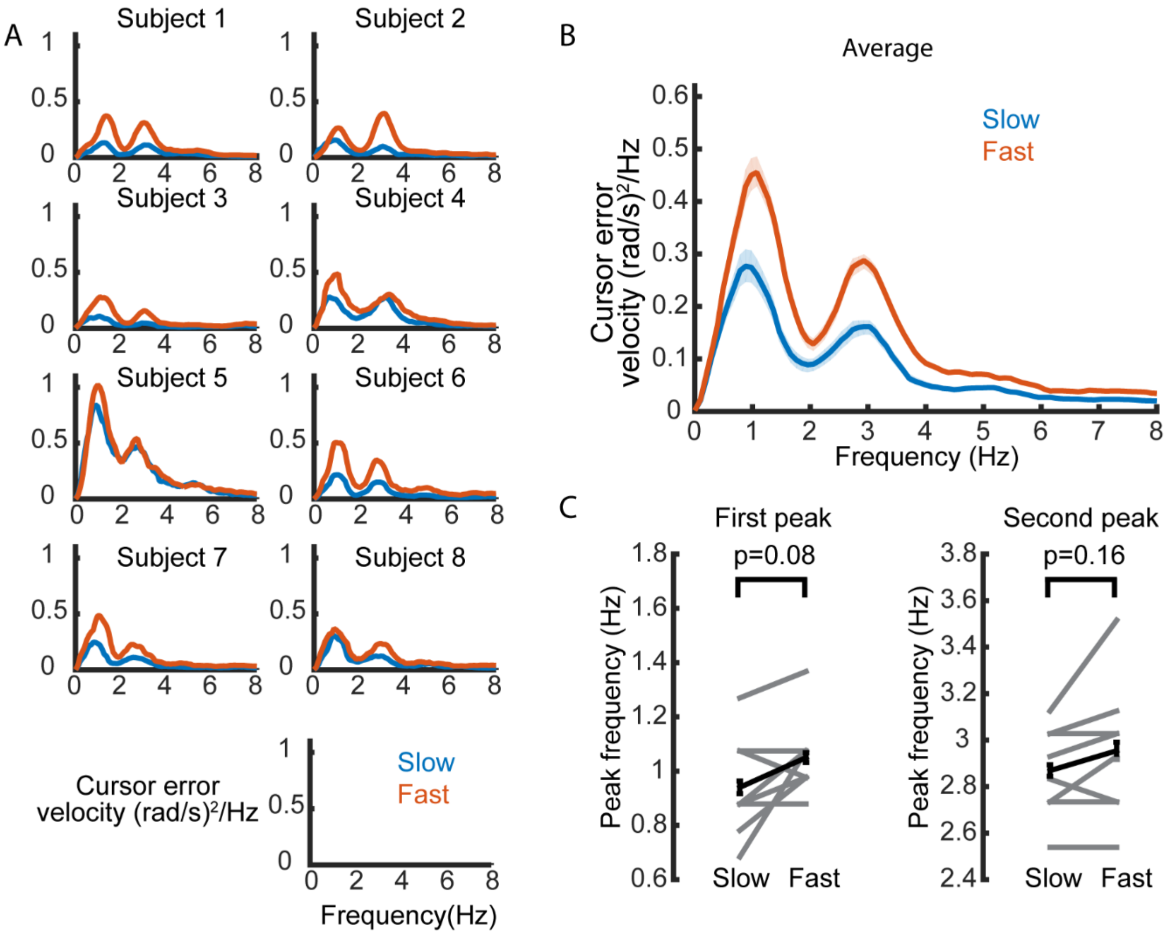

**Figure appendix A 2 Smoothed power spectra of cursor velocity at different target speeds in the 200 ms delay condition.**

**(A)** Smooth power spectra of cursor velocity in individual subjects for slow (0.1 Hz) and fast (0.2 Hz) target speed. **(B)** Average of power spectra of cursor velocity across subjects (n=8). **(C)** Comparison of submovement frequencies between slow and fast target speed.

# Appendix B. Equations

## Tracking experiment

### *Spatial perturbations*

The spatial perturbations (added to the cursor) were calculated as the difference between the actual target position, and an imaginary target that was advanced or retarded along its trajectory by a sinusoidally-varying angle:

$$Pert_{right}(f_{pert}) = 100\% \text{ x} \cos\left(2\pi f_{target}t + \frac{f_{target}}{f_{pert}}\sin\left(2\pi f_{pert}t\right)\right) - Target_{right} \tag{1}$$

$$Pert_{left}(f_{pert}) = 100\% \text{ x} \sin\left(2\pi f_{target}t + \frac{f_{target}}{f_{pert}}\sin\left(2\pi f_{pert}t\right)\right) - Target_{left} \tag{2}$$

where $Pert_{right}(f_{pert})$ and $Pert_{left}(f_{pert})$ are perturbation position added to the right and left diagonal dimension, respectively; $f_{target}$ and $f_{pert}$ are the target and perturbation frequency, respectively; $Target_{right}$ and $Target_{left}$ are target position in the right and left diagonal dimension, respectively; and $t$ refers to time points.

### *Calculation of score*

The score was calculated as follows:

$$Score = n^{-1}\sum_{t=1}^{n} e^{-\left(\sqrt{\left(\left(Cursor_{Right}(t)-Target_{Right}(t)\right)/100\right)^{2}+\left(\left(Cursor_{Left}(t)-Target_{Left}(t)\right)/100\right)^{2}}\right)/0.5} \; x \; 1000 \tag{3}$$

where $Cursor_{Right}$ and $Cursor_{Left}$ are the cursor position in the right and left diagonal dimension, respectively; and $n$ refers to number of samples.

### *Calculation of angular velocity*

In the tracking experiment, I first converted cursor and target position into an angle subtended at the centre of the screen (in radians):

$$Cursor_{Angular} = \tan^{-1}\frac{Cursor_{right}}{Cursor_{left}} \tag{4}$$

$$Target_{Angular} = \tan^{-1}\frac{Target_{right}}{Target_{left}} \tag{5}$$

where $Cursor_{Angular}$ and $Target_{Angular}$ are the cursor and target angular position; $Cursor_{Right}$ and $Target_{Right}$ are the cursor and target position, respectively, in the right diagonal dimension; and $Cursor_{Left}$ and $Target_{Left}$ are the cursor and target position, respectively, in the left diagonal dimension.

Angular position of the cursor relative to the target was differentiated to obtain the angular velocity of the cursor:

$$Cursor_{Vel} = \frac{d\left(Cursor_{Angular} - Target_{Angular}\right)}{dt} \tag{6}$$

where $Cursor_{Vel}$ is the angular velocity of the cursor.

When perturbations were added, I converted perturbation position into an angle subtended at the centre of the screen (in radians):

$$Pert_{Angular} = \tan^{-1}\frac{Pert_{right} + Target_{right}}{Pert_{left} + Target_{left}} - Target_{Angular} \tag{7}$$

$$= \frac{f_{target}}{f_{pert}}\sin\left(2\pi f_{pert} t\right)$$

where $Pert_{Angular}$ is the angular position of the perturbation.

Since perturbations were added to the cursor position, to calculate the angular position of the perturbation I used the perturbation position on top of the target position. Then I subtracted the lower frequency of the target from the angular position of the perturbation.

Angular velocity of finger-force was calculated by subtracting perturbations:

$$FingerForce_{Vel} = \frac{d\left(Cursor_{Angular} - Pert_{Angular}\right)}{dt} \tag{8}$$

where $FingerForce_{Vel}$ is the angular velocity of finger-force.

Perturbation velocity was calculated as follows:

$$Pert_{Vel} = \frac{d\left(Pert_{Angular}\right)}{dt} \tag{9}$$

$$=2\pi f_{target}\cos\left(2\pi f_{pert}t\right)$$

where $Pert_{Vel}$ is the angular velocity of perturbation.

### *Calculation of frequency response to perturbations*

To calculate the frequency response to perturbations, I first transformed perturbation velocity into a complex sine wave:

$$Pert_{Complex}(f_{Pert}) = Pert_{Vel}(f_{Pert}) + \frac{\frac{d\left(Pert_{Vel}(f_{Pert})\right)}{dt}}{2\pi f_{Pert}}i \tag{10}$$

$$= 2\pi f_{target}\, e^{-i2\pi f_{Pert}t}$$

where $Pert_{complex}$ is the complex sine wave of the perturbation.

Next, I calculated the discrete Fourier transform (DFT) of cursor velocity at perturbation frequencies using convolution:

$$DFT_{CursorVel}(f_{Pert}) = \sum_{t=1}^{n} Cursor_{vel}\, Pert_{Complex}(f_{Pert}) \tag{11}$$

where $DFT_{CursorVel}$ is discrete Fourier transform (DFT) of cursor velocity.

This value was further normalised with the amplitude of the perturbation.

Furthermore, I calculated the discrete Fourier transform (DFT) of finger-force velocity at perturbation frequencies using convolution:

$$DFT_{FingerForceVel}(f_{Pert}) = \sum_{t=1}^{n} -FingerForce_{vel}\, Pert_{Complex}(f_{Pert}) \tag{12}$$

where $DFT_{FingerForceVel}$ is discrete Fourier transform (DFT) of finger-force velocity.

This value was further normalised with the amplitude of the perturbation.

The finger force phase response was converted into time:

$$TimeDelay_{FingerForceVel}(f_{Pert}) = -\frac{Phase_{FingerForceVel}(f_{Pert})}{2\pi f_{Pert}} \tag{13}$$

where $TimeDelay_{FingerForceVel}$ is the time delay response of finger-force velocity to perturbation velocity ; and $Phase_{FingerForceVel}(f_{Pert})$ is the phase response of finger-force velocity to perturbation velocity.

### *Calculation of root-mean-squared error*

Tracking performance was reported as root-mean-squared error (RMSE), which was calculated as follows:

$$RMSE = \frac{\sqrt{n^{-1}\sum_{t=1}^{n}\left(Cursor_{Right}(t) - Target_{Right}(t)\right)^2} + \sqrt{n^{-1}\sum_{t=1}^{n}\left(Cursor_{Left}(t) - Target_{Left}(t)\right)^2}}{2} \tag{14}$$

## Tapping experiment

### *Calculation of amplitude response*

To calculate the amplitude response to targets, I first transformed target position into a complex sine wave:

$$\begin{aligned} Target_{Complex}(f_{Target}) &= Target_{Pos}(f_{Target}) + \frac{\frac{d\left(Target_{Pos}(f_{Target})\right)}{dt}}{2\pi f_{Target}} i \\ &= A_{Target}\, e^{-i2\pi f_{Target} t} \end{aligned} \tag{15}$$

where $Target_{complex}$ is the complex sine wave of the target; $Target_{Pos}(f_{Target})$ corresponds to the vertical target position; $A_{Target}$ and $f_{Target}$ are the amplitude and frequency of the target, respectively.

Next, I calculated the discrete Fourier transform (DFT) of cursor position at target frequencies using convolution:

$$DFT_{CursorPos}(f_{Target}) = \sum_{t=1}^{n} Cursor_{Pos}\, Target_{Complex}(f_{Target}) \tag{16}$$

where $DFT_{CursorPos}$ is discrete Fourier transform (DFT) of cursor position; and $Cursor_{Pos}$ corresponds to the vertical cursor position. This value was further normalised with the amplitude of the target.

## Monkey experiment

### *Calculation of cursor velocity*

I differentiated the magnitude of the absolute 2D torque (expressed as a percentage of the distance to the edge of the screen) to obtain radial cursor velocity (expressed as %/s):

$$Cursor_{Vel} = \frac{d\left(\sqrt{{Cursor_{Vertical}}^2 + {Cursor_{Horizontal}}^2}\right)}{dt} \tag{17}$$

where $Cursor_{Vel}$ is the radial cursor velocity; $Cursor_{Vertical}$ and $Cursor_{Horizontal}$ are the vertical and horizontal cursor position, respectively.

### *Calculation of magnitude squared coherence in monkey experiment*

Coherence is a measure of correlation (range 0–1) in the frequency domain between two signals, and it reflects the consistency of phase angle difference modulated by the signal magnitude. Magnitude squared coherence analysis was calculated between cursor velocity and LFP as follows:

$$Coh_{vel-lfp} = \frac{\left|S_{vel-lfp}\right|^2}{S_{vel-vel}S_{lfp-lfp}} = \frac{\left|n^{-1}\sum_{t=1}^{n}|m_{vel}|\left|m_{lfp}\right|e^{i\varphi_{vel-lfp}}\right|^2}{\left(n^{-1}\sum_{t=1}^{n}|m_{vel}|^2\right)\left(n^{-1}\sum_{t=1}^{n}\left|m_{lfp}\right|^2\right)} \tag{18}$$

where $S_{vel-lfp}$ is the cross-spectral density between cursor velocity and LFP, $S_{vel-vel}$ and $S_{lfp-lfp}$ are the auto spectral densities of cursor velocity and LFP, respectively; $m_{vel}$ and $m_{lfp}$ are the magnitude of the cursor velocity and LFP, respectively; $\varphi_{vel-lfp}$ is the phase difference between cursor velocity and LFP.

### *Calculation of imaginary cross-spectral density*

In complex vector space, cross-spectral density at a particular frequency can be represented as a vector with a real and imaginary component in which the angle of the vector represents the phase angle between two signals. A phase angle of zero or π has only a real component without an imaginary component. All other phase angles have an imaginary component. Therefore imaginary cross-spectral density reflects consistent sequential activity between two signals. To investigate whether an intrinsic correlation structure was present in the LFP, I calculated imaginary cross-spectral density between pairs of LFPs which was calculated as follows:

$$\begin{aligned} ImagCSD_{lfp1-lfp2} &= \left|imag\left(S_{lfp1-lfp2}\right)\right| \\ &= \left|imag\left(n^{-1}\sum_{t=1}^{n}\left|m_{lfp1}\right|\left|m_{lfp2}\right|e^{i\varphi_{lfp1-lfp2}}\right)\right| \end{aligned} \tag{19}$$

where $ImagCSD_{lfp1-lfp2}$ is the imaginary cross-spectral density between a pair of LFPs.

# References

Abe, N. and Yamanaka, K. (2003) SICE 2003 Annual Conference. IEEE.

Amzica, F. and Steriade, M. (1997) 'The K-complex: its slow (<1-Hz) rhythmicity and relation to delta waves', Neurology, 49(4), pp. 952-9.

Bekey, G.A. (1962) 'The human operator as a sampled-data system', IRE Transactions on human factors in electronics, (2), pp. 43-51.

Blakemore, S.-J., Frith, C.D. and Wolpert, D.M. (2001) 'The cerebellum is involved in predicting the sensory consequences of action', Neuroreport, 12(9), pp. 1879-1884.

Brewer, A.C. (2018) Color Brewer. Available at: http://www.ColorBrewer.org (Accessed: 9th of January 2018).

Celik, O., Gu, Q., Deng, Z. and O'Malley, M.K. (2009) Intelligent Robots and Systems, 2009. IROS 2009. IEEE/RSJ International Conference on. IEEE.

Churchland, M.M., Cunningham, J.P., Kaufman, M.T., Foster, J.D., Nuyujukian, P., Ryu, S.I. and Shenoy, K.V. (2012) 'Neural population dynamics during reaching', Nature, 487(7405), pp. 51-6.

Colrain, I.M. (2005) 'The K-complex: a 7-decade history', Sleep, 28(2), pp. 255-73.

Courtine, G., Bunge, M.B., Fawcett, J.W., Grossman, R.G., Kaas, J.H., Lemon, R., Maier, I., Martin, J., Nudo, R.J. and Ramon-Cueto, A. (2007) 'Can experiments in nonhuman primates expedite the translation of treatments for spinal cord injury in humans?', Nature medicine, 13(5), p. 561.

Craik, K.J.W. (1947) 'Theory of the human operator in control systems', British journal of psychology, 38(2), pp. 56-61.

Creighton, A. and Hughes, B. (2017) World Haptics Conference (WHC), 2017 IEEE. IEEE.

Debaere, F., Wenderoth, N., Sunaert, S., Van Hecke, P. and Swinnen, S.P. (2004) 'Changes in brain activation during the acquisition of a new bimanual coordination task', Neuropsychologia, 42(7), pp. 855-867.

Diedrichsen, J., Nambisan, R., Kennerley, S.W. and Ivry, R.B. (2004) 'Independent on-line control of the two hands during bimanual reaching', European Journal of Neuroscience, 19(6), pp. 1643-1652.

Diedrichsen, J., Shadmehr, R. and Ivry, R.B. (2010) 'The coordination of movement: optimal feedback control and beyond', Trends in cognitive sciences, 14(1), pp. 31-39.

Dimitriou, M., Wolpert, D.M. and Franklin, D.W. (2013) 'The temporal evolution of feedback gains rapidly update to task demands', Journal of Neuroscience, 33(26), pp. 10898-10909.

Doeringer, J.A. and Hogan, N. (1998) 'Intermittency in preplanned elbow movements persists in the absence of visual feedback', Journal of Neurophysiology, 80(4), pp. 1787-1799.

Faragher, R. (2012) 'Understanding the basis of the kalman filter via a simple and intuitive derivation [lecture notes]', IEEE Signal processing magazine, 29(5), pp. 128-132.

Fetz, E.E. (1992) 'Are movement parameters recognizably coded in the activity of single neurons?', Behavioral and brain sciences, p. 154.

Flash, T. and Sejnowski, T.J. (2001) 'Computational approaches to motor control', Current opinion in neurobiology, 11(6), pp. 655-662.

Foulkes, A.J.M. and Miall, R.C. (2000) 'Adaptation to visual feedback delays in a human manual tracking task', Experimental Brain Research, 131(1), pp. 101-110.

Gawthrop, P., Loram, I., Lakie, M. and Gollee, H. (2011) 'Intermittent control: a computational theory of human control', Biological cybernetics, 104(1), pp. 31-51.

Haken, H., Kelso, J.A.S. and Bunz, H. (1985) 'A theoretical model of phase transitions in human hand movements', Biological cybernetics, 51(5), pp. 347-356.

Hall, T.M., de Carvalho, F. and Jackson, A. (2014) 'A common structure underlies low-frequency cortical dynamics in movement, sleep, and sedation', Neuron, 83(5), pp. 1185-1199.

Hecht, S. and Shlaer, S. (1936) 'Intermittent stimulation by light', The Journal of general physiology, 19(6), pp. 965-977.

Herter, T.M., Kurtzer, I., Cabel, D.W., Haunts, K.A. and Scott, S.H. (2007) 'Characterization of torque-related activity in primary motor cortex during a multijoint postural task', J Neurophysiol, 97(4), pp. 2887-99.

Hudson, T.E. and Landy, M.S. (2016) 'Sinusoidal error perturbation reveals multiple coordinate systems for sensorymotor adaptation', Vision research, 119, pp. 82-98.

Hughes, B., McClelland, A. and Henare, D. (2014) 'On the nonsmooth, nonconstant velocity of braille reading and reversals', Scientific Studies of Reading, 18(2), pp. 94-113.

Huys, R., Studenka, B.E., Rheaume, N.L., Zelaznik, H.N. and Jirsa, V.K. (2008) 'Distinct timing mechanisms produce discrete and continuous movements', PLoS Computational Biology, 4(4), p. e1000061.

Jackson, A., de Carvalho, F., Tulip, J. and Hall, T.M. (2017) Neural Control of Movement Annual Meeting. Dublin. Society for the Neural Control of Movement.

Jagacinski, R.J. and Flach, J.M. (2003) Control theory for humans: Quantitative approaches to modeling performance. CRC Press.

Jerbi, K., Lachaux, J.P., N'Diaye, K., Pantazis, D., Leahy, R.M., Garnero, L. and Baillet, S. (2007) 'Coherent neural representation of hand speed in humans revealed by MEG imaging', Proc Natl Acad Sci U S A, 104(18), pp. 7676-81.

Kelso, J.A. (1984) 'Phase transitions and critical behavior in human bimanual coordination', American Journal of Physiology-Regulatory, Integrative and Comparative Physiology, 246(6), pp. R1000-R1004.

Kiehn, O. (2006) 'Locomotor circuits in the mammalian spinal cord', Annu. Rev. Neurosci., 29, pp. 279-306.

Kleinman, D.L. (1974) 'Towards modeling human information processing and control in economic systems: An approach based on manned vehicle systems analysis', in Annals of Economic and Social Measurement, Volume 3, number 1. NBER, pp. 117-134.

Kovacs, A.J. and Shea, C.H. (2010) 'Amplitude differences, spatial assimilation, and integrated feedback in bimanual coordination', Experimental brain research, 202(2), pp. 519-525.

Lakie, M. and Loram, I.D. (2006) 'Manually controlled human balancing using visual, vestibular and proprioceptive senses involves a common, low frequency neural process', The Journal of physiology, 577(1), pp. 403-416.

Latash, M.L., Scholz, J.P. and Schöner, G. (2002) 'Motor control strategies revealed in the structure of motor variability', Exercise and sport sciences reviews, 30(1), pp. 26-31.

Loram, I.D., Gawthrop, P.J. and Lakie, M. (2006) 'The frequency of human, manual adjustments in balancing an inverted pendulum is constrained by intrinsic physiological factors', The Journal of physiology, 577(1), pp. 417-432.

Loram, I.D., Gollee, H., Lakie, M. and Gawthrop, P.J. (2011) 'Human control of an inverted pendulum: is continuous control necessary? Is intermittent control effective? Is intermittent control physiological?', The Journal of physiology, 589(2), pp. 307-324.

McAuley, J.H., Farmer, S.F., Rothwell, J.C. and Marsden, C.D. (1999) 'Common 3 and 10 Hz oscillations modulate human eye and finger movements while they simultaneously track a visual target', The Journal of physiology, 515(3), pp. 905-917.

Miall, R.C. (1996) 'Task-dependent changes in visual feedback control: a frequency analysis of human manual tracking', Journal of motor behavior, 28(2), pp. 125-135.

Miall, R.C. and Jackson, J.K. (2006) 'Adaptation to visual feedback delays in manual tracking: evidence against the Smith Predictor model of human visually guided action', Experimental Brain Research, 172(1), pp. 77-84.

Miall, R.C., Weir, D.J. and Stein, J.F. (1986) 'Manual tracking of visual targets by trained monkeys', Behavioural brain research, 20(2), pp. 185-201.

Miall, R.C., Weir, D.J. and Stein, J.F. (1988) 'Planning of movement parameters in a visuo-motor tracking task', Behavioural brain research, 27(1), pp. 1-8.

Miall, R.C., Weir, D.J. and Stein, J.F. (1993a) 'Intermittency in human manual tracking tasks', J Mot Behav, 25(1), pp. 53-63.

Miall, R.C., Weir, D.J., Wolpert, D.M. and Stein, J.F. (1993b) 'Is the cerebellum a smith predictor?', Journal of motor behavior, 25(3), pp. 203-216.

Morasso, P. (1981) 'Spatial control of arm movements', Exp Brain Res, 42(2), pp. 223-7.

Mulliken, G.H., Musallam, S. and Andersen, R.A. (2008) 'Forward estimation of movement state in posterior parietal cortex', Proceedings of the National Academy of Sciences, 105(24), pp. 8170-8177.

Nazarpour, K., Barnard, A. and Jackson, A. (2012) 'Flexible cortical control of task-specific muscle synergies', Journal of Neuroscience, 32(36), pp. 12349-12360.

Neilson, P.D., Neilson, M.D. and O'Dwyer, N.J. (1988) 'Internal models and intermittency: A theoretical account of human tracking behavior', Biological Cybernetics, 58(2), pp. 101-112.

Partridge, L.D. (1965) 'Modifications of neural output signals by muscles: a frequency response study', Journal of applied physiology, 20(1), pp. 150-156.

Pasalar, S., Roitman, A.V. and Ebner, T.J. (2005) 'Effects of speeds and force fields on submovements during circular manual tracking in humans', Experimental Brain Research, 163(2), pp. 214-225.

Pew, R.W. (1974) 'Human perceptual-motor performance'.

Pew, R.W., Duffendack, J.C. and Fensch, L.K. (1967) 'Sine-wave tracking revisited', IEEE Transactions on Human Factors in Electronics, (2), pp. 130-134.

Qian, N. (2013) 'Movement duration, Fitts’s law, and an infinite-horizon optimal feedback control model for biological motor systems', 25(3), pp. 697-724.

Reed, D.W., Liu, X. and Miall, R.C. (2003) 'On-line feedback control of human visually guided slow ramp tracking: effects of spatial separation of visual cues', Neuroscience letters, 338(3), pp. 209-212.

Russell, D.M. and Sternad, D. (2001) 'Sinusoidal visuomotor tracking: intermittent servo-control or coupled oscillations?', Journal of Motor Behavior, 33(4), pp. 329-349.

Sakaguchi, Y., Tanaka, M. and Inoue, Y. (2015) 'Adaptive intermittent control: A computational model explaining motor intermittency observed in human behavior', Neural Networks, 67, pp. 92-109.

Schenck, W. (2008) Adaptive internal models for motor control and visual prediction. Logos Verlag Berlin GmbH.

Scott, S.H. (2004) 'Optimal feedback control and the neural basis of volitional motor control', Nature Reviews Neuroscience, 5(7), p. 532.

Scott, S.H. (2008) 'Inconvenient Truths about neural processing in primary motor cortex', J Physiol, 586(Pt 5), pp. 1217-24.

Shenoy, K.V., Sahani, M. and Churchland, M.M. (2013) 'Cortical control of arm movements: a dynamical systems perspective', Annual review of neuroscience, 36.

Siebner, H.R., Limmer, C., Peinemann, A., Bartenstein, P., Drzezga, A. and Conrad, B. (2001) 'Brain correlates of fast and slow handwriting in humans: A PET–performance correlation analysis', European Journal of Neuroscience, 14(4), pp. 726-736.

Susilaradeya, D., Galán, F., Alter, K. and Jackson, A. (2015) 'Movement intermittency: visuomotor feedback loop or intrinsic rhythmicity?', Society for Neuroscience 45th Annual Meeting. Chicago, USA.

Swinnen, S.P. and Gooijers, J. (2015) 'Bimanual Coordination', in Toga, A. (ed.) Brain Mapping: An Encyclopedic Reference. Academic Press: Elsevier, pp. 475-482.

Todorov, E. and Jordan, M.I. (2002) 'Optimal feedback control as a theory of motor coordination', Nature neuroscience, 5(11), p. 1226.

van de Kamp, C., Gawthrop, P.J., Gollee, H. and Loram, I.D. (2013) 'Refractoriness in sustained visuo-manual control: is the refractory duration intrinsic or does it depend on external system properties?', PLoS computational biology, 9(1), p. e1002843.

van der Wel, R.P.R.D., Sternad, D. and Rosenbaum, D.A. (2009) 'Moving the arm at different rates: slow movements are avoided', Journal of motor behavior, 42(1), pp. 29-36.

van Noorden, L. and Moelants, D. (1999) 'Resonance in the perception of musical pulse', Journal of New Music Research, 28(1), pp. 43-66.

Vince, M.A. (1948) 'The intermittency of control movements and the psychological refractory period', British Journal of Psychology, 38(3), pp. 149-157.

Wang, L. (1999) 'Frequency responses of phasor-based microprocessor relaying algorithms', IEEE Transactions on power delivery, 14(1), pp. 98-109.

Weir, D.J., Stein, J.F. and Mialt, R.C. (1989) 'Cues and control strategies in visually guided tracking', Journal of motor behavior, 21(3), pp. 185-204.

Wolpert, D.M. and Miall, R.C. (1996) 'Forward Models for Physiological Motor Control', Neural Netw, 9(8), pp. 1265-1279.

Wolpert, D.M., Miall, R.C., Winter, J.L. and Stein, J.F. (1992) 'Evidence for an error deadzone in compensatory tracking', Journal of motor behavior, 24(4), pp. 299-308.

Woodworth, R.S. (1899) 'Accuracy of voluntary movement', The Psychological Review: Monograph Supplements, 3(3), p. i.

Zanone, P.G. and Kelso, J.A. (1992) 'Evolution of behavioral attractors with learning: nonequilibrium phase transitions', Journal of Experimental Psychology: Human perception and performance, 18(2), p. 403.